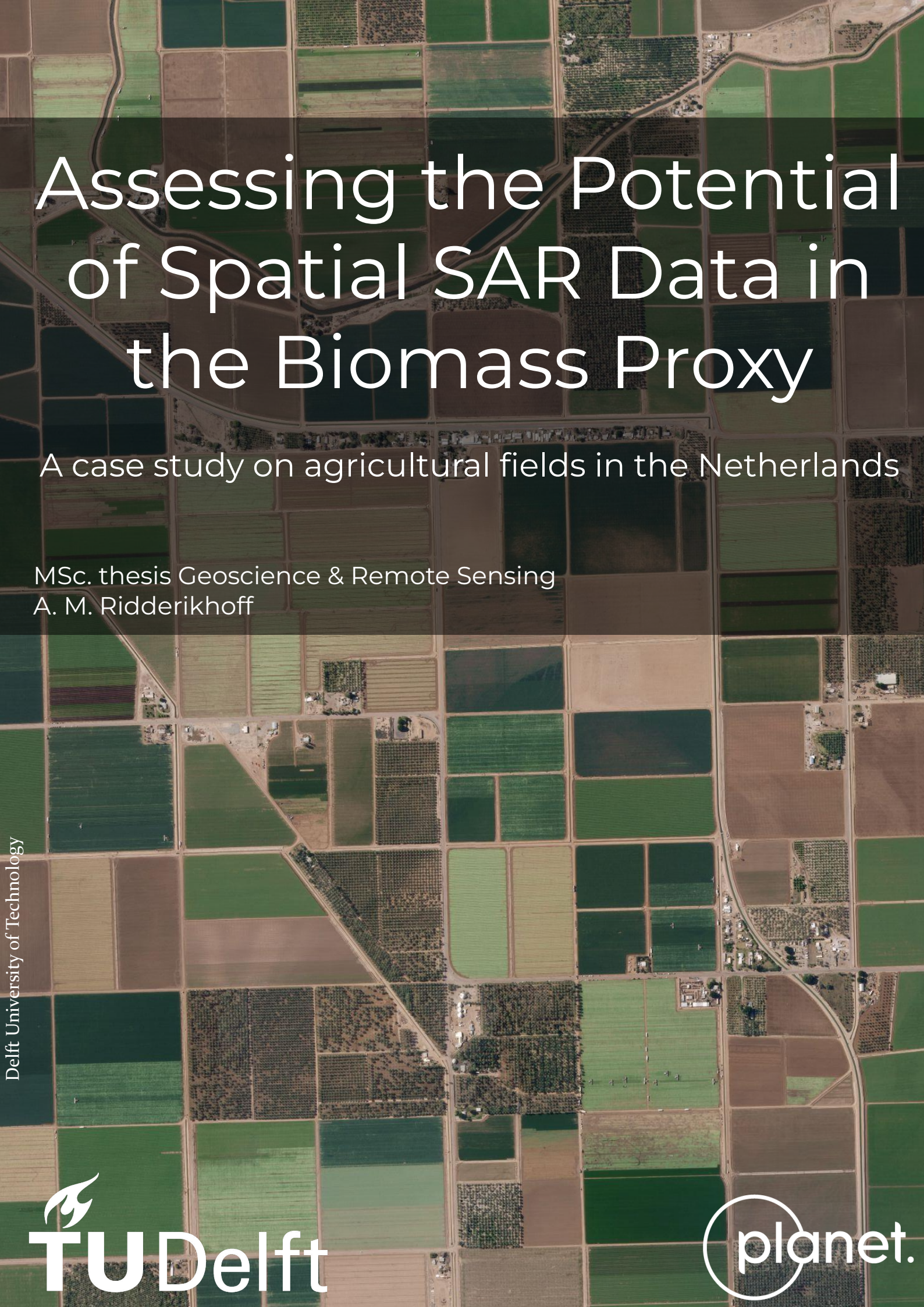

Assessing the Potential of Spatial SAR Data in the Biomass Proxy

A case study on agricultural fields in the Netherlands

MSc. thesis Geoscience & Remote Sensing
A. M. Ridderikhoff

Delft University of Technology

TU Delft

planet.

Assessing the Potential of Spatial SAR Data in the Biomass Proxy

A case study on agricultural fields in the Netherlands

by

A.M. Ridderikhoff

to obtain the degree of Master of Science
at the Delft University of Technology,
to be defended publicly on Monday Nov 21, 2022 at 09:00 AM.

Student number:	4544196	
Project duration:	Feb 1, 2022 – Nov 21, 2022	
Thesis committee:	Prof. S. Steele-Dunne,	TU Delft, chair
	Dr. F. López-Dekker,	TU Delft, supervisor
	Prof. B. Van de Wiel,	TU Delft, supervisor
	Ir. R. Burger,	Planet, supervisor

An electronic version of this thesis is available at http://repository.tudelft.nl/.

TU Delft Delft University of Technology

planet.

Abstract

Providing farmers with the tools to monitor their crops continuously and reliably can aid the scaling of global food production to meet the ever-growing demand. The optical Normalised Difference Vegetation Index (NDVI) is commonly used to monitor crop greenness as an indicator for biomass, but it is limited by clouds and signal saturation. Synthetic Aperture Radar (SAR) imagery, which is not hampered by clouds, can be used to complement the NDVI. The Biomass Proxy (BP) combines the NDVI and SAR data, but spatial biomass estimations still strongly depend on the NDVI and therefore face the same limitations. This study aims to assess the potential value of spatial SAR data to approximate the in-field biomass distribution. The SAR signal from Sentinel-1 and the NDVI signal from Sentinel-2 were analysed temporally and spatially for fields of maize, barley, oat, and spring wheat in the Dutch province of Flevoland. It was assumed that consistent SAR patterns in the spatial signal correspond to biophysical changes in the monitored crops. A framework to detect these patterns and include them in the BP was created based on combining cluster detection with spatial autocorrelation. The components of this framework demonstrate that backscatter intensity, phenological stage and crop type influence the probability of consistent patterns and that consistent patterns could not be observed from the spatial NDVI signal. Moreover, it was found that the BP's sensitivity to the input signals depends on crop type. With the knowledge of when and where consistent patterns occur, targeted research can be done to understand the spatial SAR signal better and, thereby, optimally use all available information.

Nomenclature

Acronyms

MI	Mutual Information
BBCH	Biologische Bundesanstalt, Bundessortenamt and CHemical industry
BP	Biomass Proxy
BRP	Basis Registratie Gewaspercelen
CR	Cross Ratio
CV	Coefficient of Variation
DB	Davies Bouldin
GLCM	Grey Level Co-occurrence Matrix
GRD	Ground Range Detected
IW	Interferometric Wide
LAI	Leaf Area Index
NDVI	Normalised Difference Vegetation Index
NESZ	Noise Equivalent Sigma Zero
NIR	Near Infra-Red
NRCS	Normalised Radar Cross Section
PI	Partial Information
pmf	Probability mass function
RCS	Radar Cross Section
RMS	Root Mean Square
S1	Sentinel-1
S2	Sentinel-2
SAR	Synthetic Aperture Radar
SNR	Signal to Noise Ratio
VWC	Vegetation Water Content

Greek Symbols

λ	Wave length
μ	Mean
σ	Standard deviation
σ^0	Normalised radar cross section (NRCS)

Roman Symbols

c	Contribution of signal in fused product
d	Distance
E	Wave vector of electromagnetic wave
f	frequency
H	Entropy
I	Number of classes of random variable
K	Number of distance intervals
k	Wave number
L_d	Leibovici adjencency matrix
N_g	Number of discrete interval levels in image
P	Co-occurrence matrix
qf	Quality factor
R	Number of classes of univariate or bivariate random variable
r	Distance between satellite and scattering surface
S	Complex scattering amplitude matrix
W	Bivariate random variable
w_s	Static weight
X	Random variable
Z	Univariate random variable

Other Symbols

HH	Horizontal co-polarised
VH	Vertical-Horizontal cross-polarised
VV	Vertical co-polarised

Preface

The following thesis is the result of the research I have conducted over the past eight months for my master's in Geoscience and Remote Sensing at the Delft University of Technology. The research concerns assessing the potential of spatial Synthetic Aperture Radar data to approximate the in-field biomass distributions for agricultural fields in the Netherlands. I am very happy to have been able to collaborate with Planet Labs. This company provides daily satellite data that helps businesses, governments, researchers, and journalists understand the physical world and take action. Their Biomass Proxy product, an algorithm that predicts biomass temporally and spatially, formed the basis for my research. Intending to improve the product by utilising all available information, I developed a framework to detect and implement possibly relevant spatial information. The research has made the first steps in understanding the spatial data and has demonstrated the complementary value of the spatial SAR data to the NDVI. Although limitations exist, this framework will hopefully support the next steps in utilising radar data spatially and contribute to the transition towards precision agriculture.

I am very thankful for the valuable feedback, the brainstorming sessions, and the genuine interest of everyone involved. First, I want to express a special thanks to all my supervisors. Susan Steele-Dunne always made time for our meetings and was always able to make sense of all the ideas I fired at her. Besides that, she was always kind, provided me with great insights and introduced me to the most beautiful colour map. Paco López-Dekker made sure I could zoom out and look at it through someone else's eyes, making sure this thesis is readable for outsiders and, thereby, will hopefully be used in the future. I want to thank Bas van de Wiel for making time to read and evaluate my thesis. Finally, I want to thank Rogier for his ever-lasting enthusiasm, valuable feedback and drive to improve, which has kept me truly motivated throughout the past months.

I want to end by thanking everyone at Planet, who all have made me feel welcome, showed genuine interest in my work, and were always helpful. Especially the members of my team, the Biomass Proxy POD, who were always kind, supportive, and motivating. Moreover, I want to thank my dear friends and family for proofreading and the endless moral support, especially Thomas, my mother, Emiel, Roos and Daan.

A.M. Ridderikhoff
Delft, November 2022

Contents

List of Figures

List of Tables

1 Introduction

This chapter provides an introduction to this thesis. First, in Section 1.1, some context on agricultural monitoring with remote sensing and an overview of previous work in the field is given. Then, in Section 1.2, the scope of this thesis is defined by posing the research questions. Last, the document structure is presented in Section 1.3.

1.1. Context

As the stress on food supply increases due to the growing world population and changing climate, crop monitoring can be a key component in ensuring food security (Kuester & Spengler, 2018; Mkhabela, Mkhabela, & Mashinini, 2005; Veloso et al., 2017). By closely monitoring agricultural fields, yields can be predicted, and water use can be optimised (Awad, 2019). Fields can be mapped daily and accurately with the help of satellite imagery (McNairn & Shang, 2016). One of the major challenges is the scalability of this monitoring. With a global food demand that is expected to double by 2050 (Godfray et al., 2010; Tilman, Balzer, Hill, & Befort, 2011), the agricultural sector continues to grow, and suitable technologies that can be applied at scale are indispensable (Behzad et al., 2019). Remotely sensed data can provide continuous and reliable crop information, enabling farmers and food producers to optimise the available resources and implement timely interventions to maximise yields (Khabbazan et al., 2022). In addition, crop monitoring can also help reduce the use of pesticides and fertilisers and promote more environmentally friendly land management (Vreugdenhil et al., 2018). With crop monitoring on this scale, the first steps towards the transition towards precision agriculture can be made.

1.1.1. Agricultural monitoring using remote sensing

Crop monitoring is often still done manually by inspection on the ground, which has the disadvantages that it is labour-intensive, can only be executed on a small scale, and does not give a clear insight into long-term trends (W. Li & Guo, 2010). Due to these problems, the use of remote sensing for crop monitoring has quickly gained popularity over the last few decades, providing more and more farmers with cost-effective, efficient, and reliable data for cropland management (Zhao, Qu, Chen, & Yuan, 2020). Often, remote sensing methods use vegetation indices derived from optical and Near Infra-Red (NIR) bands (Andela, Liu, M. Van Dijk, De Jeu, & McVicar, 2013), which can be used to estimate the biophysical parameters of the crops. One of the most common indices is the Normalised Vegetation Index (NDVI), which is a measure of the greenness (chlorophyll) of the backscattering surface (Tarpley, Schneider, & Money, 1984). Over the last few decades, many methods have been developed to process the optical remote sensing data, and the resolution and repetition frequency of the data have increased significantly (Zhao et al., 2020). Nevertheless, optical imagers that rely on clear-sky conditions will always have limitations. For crop monitoring, persistent cloud cover will drastically reduce the number of usable imageries, resulting in a poor temporal resolution of the data.

Radar remote sensing provides information which the optical-based vegetation indices cannot capture. Two inherent differences between the techniques cause this. Firstly, radar satellites are active satellites, meaning they transmit *and* receive signals. This enables day- and night monitoring since the signal does not depend on sunlight. Secondly, radar waves have a much longer wavelength than optical signals, allowing the

electromagnetic waves to pass through clouds and be unhindered by other atmospheric conditions (Vreugdenhil et al., 2020). Because of these characteristics, the temporal resolution only depends on the satellite revisit time and is, therefore, much higher than that of optical remote sensing. This difference in temporal resolution is visualised in Figure 1.1 for an agricultural field in the Netherlands.

Moreover, the radar waves can penetrate the surface it scatters onto a certain depth, depending on the wavelength. Thus, the backscattered signal can provide valuable insights into the structure and the material of the surface it interacts with (Ottinger & Kuenzer, 2020). Furthermore, because of its ability to penetrate the surface, the signal gets saturated at a higher vegetation density than the NDVI (Y. Y. Liu, Van Dijk, De Jeu, Mccabe, & Evans, 2012). However, due to its longer wavelength, radar has a much lower spatial resolution than optical data and compared to optical data. The use of SAR data in agricultural applications has advanced less; partly because SAR data is more complicated, diverse, and less accessible, and in part, because data interpretation is more challenging (Veloso et al., 2017).

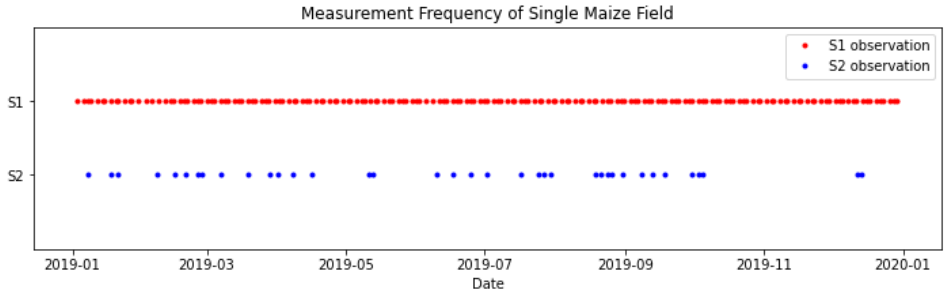

Figure 1.1: Full-coverage observation frequency of the radar Sentinel-1 (S1) and optical Sentinel-2 (S2) satellites of an arbitrary maize field in Flevoland.

1.1.2. Previous work

Agricultural remote sensing has extensively been researched for different purposes, such as crop yield estimation (Abdikan, Sekertekin, Ustunern, Balik Sanli, & Nasirzadehdizaji, 2018; J. Liu et al., 2010; Mkhabela et al., 2005), agricultural drought monitoring (X. Liu et al., 2016; Rhee, Im, & Carbone, 2010; Sánchez, González-Zamora, Martínez-Fernández, Piles, & Pablos, 2018) and estimating crop phenology (De Bernardis, Vicente-Guijalba, Martinez-Marin, & Lopez-Sanchez, 2016; Meroni et al., 2021; Schlund & Erasmi, 2020). For crop monitoring, a substantial amount of literature is available on optical and radar methods. For optical data, many studies focus on a single parameter of the monitored crops and its relation to vegetation indices such as the NDVI. Examples include leaf area index (LAI) monitoring (Asner, 1998; Kuusk, 1991), phenological stage determination (Onojeghuo et al., 2018; Ulsig et al., 2017), or biomass estimation (C. Li et al., 2019; Meng, Du, & Wu, 2013). Studies analysing the radar backscatter response have also found significant relations between crop parameters and the signal. For instance, Blaes et al. (2006) report relationships for maize crops between various polarisations and the vegetation parameters LAI, biomass, and plant height. Vreugdenhil et al. (2018) assess the potential of Sentinel-1 vertical co-polarised (VV) and cross-polarised (VH) backscatter and their ratio VH/VV, the cross ratio (CR), to monitor these same parameters and the vegetation water content (VWC). The feature importance of the different microwave indices was determined by training a random forest model on two test sites with the radar data and in-situ measurements. Paris (1983) describes the backscattering coefficients of maize and soybean for different frequencies, sensor look-angles, and polarisation combinations. They identified when row direction differences play a role, how surface-soil moisture influences the backscatter, and how depolarisation of the signal can help classify the crops. Furthermore, Mc Nairn and Brisco (2004) and Steele-Dunne et al. (2017) both comprehensively review agricultural monitoring with radar.

Besides studies on either optical or radar remote sensing, valuable studies discussing the relationship between the two were also published, e.g. Behzad et al. (2019); Veloso et al. (2017). These studies aim to improve understanding of both signals and compare their responses to growing vegetation. This relationship has been further explored and used in other studies where the signals were combined. For instance, Valero, Arnaud, Planells, and Ceschia (2021) implemented a method to use the combination of Sentinel-1 and Sentinel-2 data for cropland and crop type classification. Zhao et al. (2020) conducted a study using deep neural networks

to fill in the temporal data gaps of optical data with radar data. Chang and Shoshany (2016) showed that a 14% increase in accuracy could be reached by combining radar and optical signals for estimating biomass in shrublands. Blickensdörfer et al. (2022) proposed a workflow based on combined optical, radar, and environmental data for agricultural land cover maps that accounts for varying environmental conditions and shows a 6% to 10% increase in accuracy compared to single data sources.

Reviewing the existing literature, it becomes apparent that the studies can roughly be divided into three types:

1. identifying the relationship between biophysical parameters and remote sensing data, e.g. defining the relationship between the radar signal and LAI
2. a temporal analysis of radar or optical signals, e.g. extracting sowing and harvest dates with radar backscatter
3. agricultural land cover mapping, e.g. performing crop classification on an agricultural area

Types one and two are based on temporal analyses, while type three is based on the distribution in space. These studies form a good basis for understanding backscatter responses through time and for the differences between crops. However, research on (spatial) in-field variability of biomass is minimal. One could speculate that this is because obtaining spatial validation data at the field level is very labour-intensive and would require destructive samples or because the spatial resolution of radar is too coarse for many (small) fields. Either way, in-field vegetation parameter monitoring would provide valuable information for crop management practices.

To tackle these problems, the *Biomass Proxy* (BP) could be deployed, which is a product of Planet Labs PBC (formerly known as VanderSat) to monitor biomass in agricultural fields (Planet Labs PBC, 2022). The BP is a fusion of the Sentinel-1 (SAR) and the Sentinel-2 (NDVI) imagery, using the advantages of each to estimate relative above-ground crop biomass regardless of cloud cover accurately and at a high spatial resolution (10 m x 10 m). Before fusing the signals, the CR is extracted from the SAR signal and filtered in time and space, resulting in the *Sentinel-1 (S1) index*. From this S1 index and the NDVI, daily biomass estimations can be computed. The output is given in time and space at the field level, representing the relative amount of biomass between 0 (low biomass) and 1 (high biomass). The model owes its strength to the fusion of the radar and optical data in the spatial and temporal domains separately, making it possible to utilise the high temporal resolution of the radar data and the high spatial resolution of the optical data. Despite the valuable insights the algorithm already provides, it has not yet reached its full potential, especially in the spatial domain. The algorithm is designed to rely strongly on optical data for spatial information. And, therefore, faces the same challenges as regular optical monitoring, namely large data gaps due to cloud cover and saturation of the signal.

1.1.3. Research gap

So far, this section has highlighted the substantial amount of knowledge on the temporal SAR and NDVI signals for agricultural monitoring, as well as the lack of knowledge on spatial interpretation of the SAR data. Although the BP has already taken considerable steps towards providing crop data with high temporal and spatial resolution using the SAR and NDVI signals, it is still spatially limited due to its dependency on optical data.

The contribution of the SAR signal could be increased in the fusion of the BP to reduce this dependency. However, without the research and knowledge of the spatial characteristics of the radar data, this would lead to uninterpretable results. So far, research has yet to be conducted on which characteristics contain valuable information and how they could be fused with the NDVI. With this information, the contribution of the SAR data in the BP could deliberately be increased or decreased such that the information gain can be optimised without losing interpretability.

This study aims to bridge this gap by assessing the potential of spatial SAR data for agricultural monitoring.

1.2. Research objective

The research gap forms the basis of this study. The objective of this study is, therefore, to assess the potential of spatial SAR data to approximate the in-field biomass distribution. Consequently, this information could be used to evaluate how this could improve the BP.

The main obstacle is probably why this research has not been not carried out before: the lack of spatial validation data. This was also the case for this research, and, therefore, the answers given in response to the questions addressed in this research are also solely based on remotely sensed data. In the process, two important assumptions are made about the radar data: 1) some of the spatial patterns in the radar signal represent real and valuable information, while others are radar 'artefacts', and 2) persistent patterns occurring in the field multiple observations in a row, represent real information while quickly fluctuating patterns do not. Based on this objective and these assumptions, the research will address the following questions:

1. How do NDVI and SAR data describe biophysical changes of various crops in the temporal and spatial domains?
2. What spatial metrics can be used in which situations as indicators for clustering of the spatial S1 index data?
3. How often are clusters in the radar signal persistent, and what causes these persistent clusters?
4. How is the Biomass Proxy influenced by the static weight of the Sentinel-1 data, and how does this change throughout the growing season?

The research has been carried out for the province of Flevoland in the Netherlands, an agriculturally dense area with a low probability (20%) of acquiring optical imagery without cloud cover in the growing season (van der Wal et al., 2013). The crops investigated all have above-ground biomass and were grown on at least 50 fields in Flevoland in 2019, the year of which the data was used. These crops are maize, barley, oat, and (spring) wheat. Note that winter wheat is also often cultivated, but since this would bring more uncertainty in the analyses of the signals due to different climatological conditions, it is not researched.

1.3. Reading guide

To give a deeper understanding of the signals, vegetation, and the complexity of their interaction, an extensive theoretical background is given in Chapter 2. In addition to the signals and vegetation, Section 2.5 provides an overview of the spatial features used to describe the spatial data and Appendix C background information on a pattern detection algorithm. Next, the steps of the methodology are described in Chapter 3. This chapter starts with a description of the study area and the data sets used in Section 3.1. The following sections, Section 3.2 to Section 3.5, correspond to the research question posed in Section 1.2. Finally, the results are presented and discussed in Chapter 4, and Chapter 5 contains the conclusions and recommendations.

2

Theoretical Background

This chapter provides an overview of the main topics to understand the methods, analyses and discussions in this study. Each topic is by no means exhaustive but will help gain a necessary basic understanding. First, in Section 2.1 and Section 2.2, the input signals of the BP algorithm are discussed. Section 2.3 reviews existing literature on the use of these signals for agricultural monitoring. Section 2.4 explains the theory behind the algorithm, focused on the spatial processing of the SAR signal. Finally, in Section 2.5, multiple evaluation metrics are presented, which are used to describe the spatial signals.

Additional background on the crop development stages, entropy and *K-means* clustering is presented in Appendix A, Appendix B, and Appendix C respectively. These topics are not essential in understanding the narrative, but support the understanding of the analyses.

2.1. Normalised Difference Vegetation Index

The *Normalised Difference Vegetation Index* (NDVI) is a commonly used index in agricultural remote sensing. The index can, amongst others, be used for crop monitoring (e.g. Fang, Yan, Wei, Zhao, and Zhang (2021); C. Li et al. (2019); Seo, Lee, Lee, Hong, and Kang (2019); Veloso et al. (2017)), yield forecasting (e.g. Groten (1993); Maselli (n.d.); Mkhabela, Bullock, Raj, Wang, and Yang (2011); Mkhabela et al. (2005)) and agricultural management practices (e.g. Meivel, Maheswari, and Grade (2020); Xue et al. (2014)). The index is based on the properties of green vegetation to reflect the incident solar radiation differently in the Near Infra Red (NIR) and Red (R) spectral wave bands (Mkhabela et al., 2005). The NDVI is calculated as follows (Tarpley et al., 1984)

$$NDVI = \frac{NIR - R}{NIR + R} \tag{2.1}$$

where the NDVI is unitless and ranges from -1 to +1. The index is sensitive to chlorophyll pigment in green vegetation and leaf scattering mechanisms, which cause low spectral reflectance in the visible red band and high reflectance in the near-infrared band (De Bernardis et al., 2016). Healthy green vegetation, therefore, corresponds to high positive values. In contrast, non-vegetated surfaces such as bare soil, ice, water, snow and clouds usually correspond to NDVI values close to zero or even slightly negative (Mkhabela et al., 2005). Negative values often denote water (Laksono, Saputri, Pratiwi, Arkan, & Putri, 2020). Vegetation with a small leaf area or stressed vegetation have positive, but reduced, NDVI values (Kogan' & Ciren', 1994). An agricultural crop's typical temporal NDVI profile rises in spring as plant cover increases, peaks during summer and drops when the crop is harvested. However, when the plants change to yellow or golden colours during the senescence, the NDVI will decline before the harvest.

Advantages of the NDVI include the intuitive interpretation, comparatively high resolution (due to the short wavelengths of the signal) and strong scientific foundation. Unfortunately, the NDVI also provides limited information both spatially and temporally. The spatial signal is limited since the NDVI only senses the top of the vegetation (Y. Y. Liu, van Dijk, McCabe, Evans, & de Jeu, 2013), saturates in dense vegetation (Fang et al., 2021), is limited by atmospheric effects such as clouds, cloud shadows and aerosols (Vreugdenhil et al., 2018), and is sensitive to effects of soil brightness and colour (Y. Y. Liu et al., 2013). Besides that, the NDVI is temporally severely limited due to atmospheric influences such as clouds and aerosols (Kobayashi & Dye, n.d.) and its dependency on daylight. An overview of these advantages and disadvantages is shown in Table 2.1.

Advantages	Drawbacks
• High spatial resolution	• Limited by atmospheric effects (clouds, cloud shadow, aerosols); poor temporal resolution
• Simple and intuitive	• Saturation on dense vegetation
• Open source data	• Only senses the top layer of the canopy
	• Sensitive to effects of soil brightness and colour

Table 2.1: Advantages and disadvantages of NDVI for remote sensing C. Liu et al. (2013); Xue et al. (2014).

2.2. Synthetic Aperture Radar

This section will provide an overview of the theoretical background needed to understand and analyse the Synthetic Aperture Radar (SAR) signal. The technical side of the SAR and the interaction with the vegetation must be considered to gain a sufficient understanding of the received signal.

2.2.1. Basic SAR principles

Since SAR can provide images independent of daylight, cloud coverage and weather conditions, it is predestined to monitor the Earth's dynamic processes. SAR systems are active microwave sensors transmitting electromagnetic waves at microwave frequency and receiving the backscattered signal. The waves are transmitted from a pulsed radar installed on a platform with forward movement. The system's echo is received sequentially (Moreira et al., 2013). The transmitted pulse's frequency typically ranges between 450 MHz and 35 GHz, but the most common frequencies are 1.3-1.4 GHz (L-band), 5.3-5.4 GHz (C-band) or 9.56 GHz (X-band) (López-Dekker & De Zeeuw Van Dalsen, 2021). When the signal interacts with the Earth's surface, the amplitude, phase and polarisation change depending on the physical (e.g. geometry, roughness) and electrical properties (e.g. permittivity) of the imaged object. The transformation of the emitted wave (E^t) to the received wave (E^r) is defined as (Lee & Pottier, 2009)

$$\begin{aligned} \vec{E}^r &= \frac{\exp(-\mathrm{i}kr)}{r}[S]\vec{E}^{t^*} \\ \begin{bmatrix} E_H^r \\ E_V^r \end{bmatrix} &= \frac{\exp(-\mathrm{i}kr)}{r} \cdot \begin{bmatrix} S_{HH} & S_{HV} \\ S_{VH} & S_{VV} \end{bmatrix} \begin{bmatrix} E_H^t \\ E_V^t \end{bmatrix}^* \end{aligned} \tag{2.2}$$

The elements of $[S]$ denote the four complex scattering amplitudes $S_{IJ} = \left|S_{IJ}\right| \exp\left(\mathrm{i}\varphi_{IJ}\right)$, where the H and V subscripts indicate the horizontal and vertical polarisations respectively. The phase shift and attenuation for a spherical wave are expressed by the factor $exp(-ikr)/r$, with $k = 2\pi/\lambda$ the wave number. These vertical and horizontal linear polarisations refer to the orientation of the electric field vector of the transmitted and received electromagnetic wave and should be interpreted in the context of the structure of the target (McNairn & Shang, 2016). The polarisation possibilities are visualised in Figure 2.1b. The transmitted and received configuration of the polarisations is instrument dependent: dual-polarised instruments transmit H or V and receive H and V simultaneously, and quad-polarised instruments transmit H and V on alternate pulses and also receive them simultaneously (Podest, Pinto, & Fielding, 2017).

Since SAR operates in the microwave part of the electromagnetic spectrum, it does not capture images the same way as optical satellites do. Instead, they provide reflectivity maps of the region of interest (ROI), where targets appear bright if the signal is directly reflected and dark when the target's backscatter is low. The flight direction is denoted as the azimuth and the line-of-sight as slant range direction (Moreira et al., 2013). A Single Look Complex (SLC) product is the 'image' the radar takes of a scene in the slant range by azimuth imaging plane. Each image pixel is represented by a complex magnitude value and therefore contains amplitude and phase information (ESA, n.d.). Figure 2.1a illustrates the typical SAR geometry, where the platform moves in the azimuth or along-track direction, whereas the slant range is the direction perpendicular to the radar's flight path. Because of this geometry, SAR is side-looking (unlike optical sensors, which are usually nadir-looking). The swath width gives the ground-range extent of the radar scene, while its length depends on the 'duration' of the image, i.e., how long the radar is turned on (Moreira et al., 2013).

Targets scanned by the radar all have a radar cross section (RCS or σ), which measures how detectable an object is by radar. Objects with a larger RCS are, therefore, easier to detect. The reflected signal can be represented by the backscatter coefficient, which is the RCS (or backscattering area) per unit ground area,

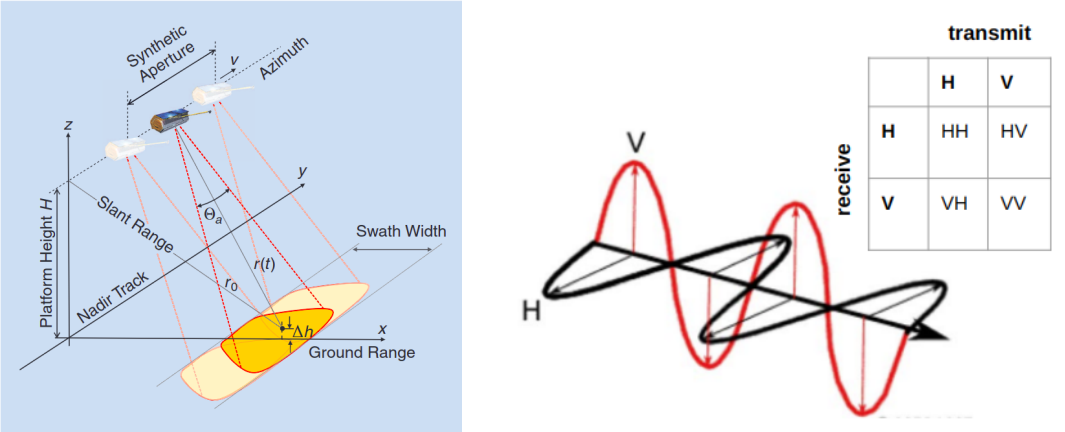

(a) Illustration of the SAR imaging geometry. r_0 stands for the shortest approach distance, Θ_a for the azimuth beam width and v for the sensor velocity (Moreira et al., 2013).

(b) Linear polarisations of the electromagnetic waves, adjusted figure from (Skrunes, Brekke, & Eltoft, 2014).

Figure 2.1: Basic principles of SAR satellite geometry and polarimetry.

also referred to as the normalised radar cross section (NRCS or σ^0). Because σ^0 depends on many factors of the target (e.g. size, structure, geometry and electromagnetic characteristics), it can vary by several orders of magnitude. Therefore, it is often converted to dB as $10log_{10}\sigma^0$. It can be seen as a measure to determine whether the radiated terrain scatters the incident microwave radiation preferentially towards the SAR sensor (dB > 0) or away from the sensor (dB < 0) (ESA, 2012). Besides the properties of the reflective surface, σ^0 generally has a significant variation with incidence angle, wavelength, and polarisation (MacDonald, 2011). This incidence angle results from the target's topography and the satellite's geometry, i.e. the relative orbit. Earth's topography distorts the radar signal when there is relief displacement. Effects include foreshortening, layover and variations in the ground resolution along the range direction (McNairn & Shang, 2016). Therefore, satellite radar images must be orthorectified using the orbital models and the Digital Elevation Model (DEM) (Marsetič, Oštir, & Fras, 2015). The orbit model provides information on the satellite's geometry: each relative orbit has a a certain satellite direction (ascending or descending) and a range of incidence angles. Since SAR is side-looking, different areas are illuminated in the ascending or descending direction. The flight direction impacts the illuminated pixel area and, depending on the local incidence angle, can lead to differences in backscatter intensity. If the ROI is completely flat, this effect is minimised. However, the sensor is still theoretically interacting with other parts of the surface (Dumitru & Datcu, 2013).

The azimuth resolution δ_a is determined by the smallest separation between two point targets detected by the radar. For a simple radar, this is inversely proportional to the length of the antenna, i.e. a long antenna will have a good azimuth resolution. In order to improve the resolution without drastically having to increase the antenna size, many pulses are transmitted from short antennas which have an overlap in the scene they capture. By combining these lower resolution images, a longer antenna is simulated, hence the name *Synthetic Aperture Radar* (López-Dekker & De Zeeuw Van Dalsen, 2021). The slant-range resolution δ_r is inversely proportional to the system bandwidth according to $\delta_r = c_0/2B_r$ with c_0 the speed of light (Moreira et al., 2013). Note that the spatial resolution is not the same as pixel spacing: the former describes the system's ability to distinguish between adjacent targets, while the latter corresponds to the distance between adjacent pixels in an image, expressed in meters. For Sentinel-1, this means that the spatial resolution of 20x22 m corresponds to a pixel spacing of a grid of 10x10 m (European Space Agency, 2012).

2.2.2. SAR image properties

As mentioned in Section 2.2.1, optical and SAR images do not capture the same information. Because the nature of the signal is different, both come with their own challenges and complications. Roughly, two types of effects that significantly degrade the spatial resolution of the output image can be defined: system noise and speckle (ESA, 2012).

The Noise Equivalent Sigma Zero (NESZ) measures the sensor's sensitivity to low backscatter areas, encompassing all system noise sources, including thermal noise and quantisation noise sources (ESA, 2012). It is defined as the NRCS of a distributed target within the product coverage for which the signal power level in the final image is equal to the noise power level (thermal noise only), i.e. an image with a Signal to Noise Ratio (SNR) of 0 dB. The values of the NESZ depend on the incidence angle, polarisation and sensor characteristics (Lopez-Sanchez, Vicente-Guijalba, Erten, Campos-Taberner, & Garcia-Haro, 2017). However, since this difference between co- and cross-polarisation is less than 0.1 dB, these differences often are neglected (MacDonald, 2011). The thermal noise included in the NESZ is an additive noise caused by the sensor and only becomes relevant when the signal mean is low. In the multi-swath acquisition modes, this noise typically has a different intensity in each sub-swath, and the data (including noise contributions) are multiplied during the raw SAR focusing (Piantanida, Miranda, & Hajduch, 2017). During the post-processing of the data (in the Level 1 GRD data), the additive noise in the sub-swaths is removed to help reduce discontinuities between sub-swaths for scenes in multi-swath acquisition modes (ESA, 2012).

Speckle, on the other hand, is a multiplicative 'noise' that inherently exists in SAR and severely limits spatial resolution. It is also known as radar noise and is caused by the presence of many scatterers within a resolution cell, all with a different random distribution. The coherent sum of their phases and amplitudes results in strong fluctuations of the backscattered signal between the resolution cells. Consequently, the intensity and phase in the final image are no longer deterministic but follow an exponential and uniform distribution, respectively (Oliver & Quegan, 2004). This effect is illustrated in Figure 2.2.

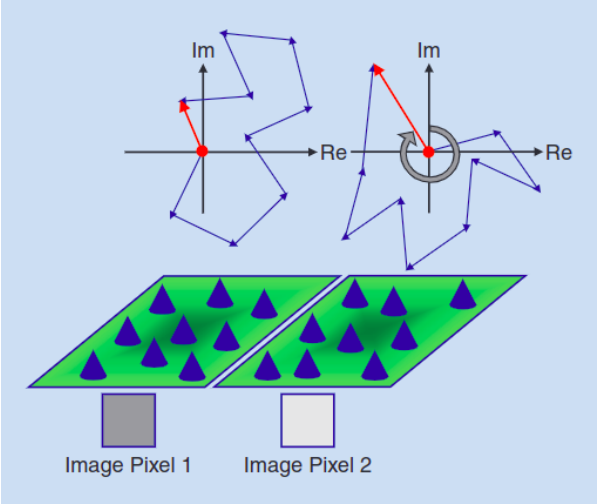

Figure 2.2: Speckle occurs in SAR images due to the coherent sum of many elemental scatterers within a resolution cell. The two parallelograms show the distribution of the scatterers in each resolution cell and the resulting amplitude and phase values (Moreira et al., 2013).

With these image properties, the Signal to Noise Ratio (SNR) can be defined as follows (Park, Won, Korosov, Babiker, & Miranda, 2019):

$$SNR_{pp} = \frac{\sigma^0_{pp} - NESZ_{pp}}{NESZ_{pp}} \tag{2.3}$$

where the subscript pp defines the polarisation. The NESZ varies with incidence angle but has a maximum of -22.2 dB for Sentinel-1 (MacDonald, 2011). As the formula shows, the SNR decreases as the backscatter (σ^0) becomes lower, i.e. images of low reflective surfaces are noisier.

The radar images (in Level 1) can be processed either from a Single Look Complex (SLC) image or Ground Range Detected (GRD) image. Level-1 SLC products consist of focused SAR data, geo-referenced using orbit and altitude data from the satellite, and provided in slant-range geometry. The products include a single look in each dimension using the full available signal bandwidth and complex samples (real and imaginary), preserving the phase information (Miranda & Meadows, 2015).

In order to reduce the amount of speckle and compress the data, neighbourhoods of pixels can be averaged. This is also known as multi-look processing (Canty, 2014). It is, however, at the cost of spatial resolution. The result is the Level-1 GRD product, which consists of focused SAR data and has been multi-looked and

projected to ground range using the Earth ellipsoid model WGS84. Each pixel value represents the detected amplitude, but due to the multi-looking, phase information is lost (Miranda & Meadows, 2015).

To summarise, the advantages and disadvantages of SAR remote sensing are shown in Table 2.2. Comparing this with the advantages and disadvantages of NDVI (Table 2.1), one can see that the two signals are complementary on some levels, but also how they come with their own challenges.

Advantages	**Drawbacks**
• SAR can produce data day and night since it is an active sensor that does not depend on sunlight.	• Extended target areas that one would expect to have a constant backscattering behaviour (e.g., large homogeneous agricultural fields) show speckle.
• SAR backscattering depends on different physical properties of the target than the properties that cause optical reflectance. These properties relate to (electromagnetic) material properties and structural geometry of the target.	• SAR backscattering depends on the angle of incidence of the radar waves, i.e. the same target will appear different depending on whether it is the near or far range of the swath. Moreover, how the backscattering varies with the incidence angle is target-dependent.
• SAR is insensitive to atmospheric conditions in C-band (except for very dense rain cells).	• SAR backscattering is strongly influenced by terrain relief because it modulates the illuminated area by the side-looking SAR radiation.
• SAR data can be calibrated, without the need for atmospheric correction, leading to consistent time series.	• To use SAR data efficiently, one needs to be aware of what part of the signal relates to the intrinsic sensor properties and what part to the physical properties of the target.

Table 2.2: Advantages and disadvantages of SAR for remote sensing (Google Developers, 2022).

2.2.3. Microwave backscatter from vegetated surfaces

With a general understanding of the observation configuration and signal properties, the backscattered signal can be evaluated and interpreted. SAR signals can be difficult to interpret due to their sensitivity to several parameters. Ulaby et al. (2019) divides these parameters into two sets: sensor (or wave) and terrain parameters. After a brief introduction to the types of backscatter, this subsection will go into the different wave and terrain parameters influencing the backscatter.

The total SAR backscatter is conventionally expressed in received dB and can broadly be split into three categories (Ottinger & Kuenzer, 2020):

1. Direct or surface backscatter Figure 2.3(a)
2. Volume backscatter Figure 2.3(b)
3. Double-bounce backscatter Figure 2.3(c)

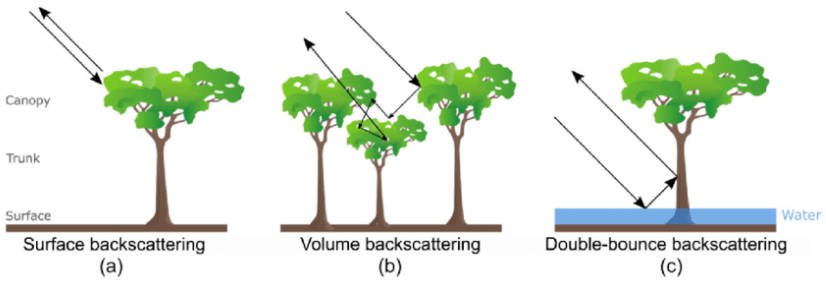

Figure 2.3: Radar backscattering mechanisms (Ottinger & Kuenzer, 2020).

One source of scattering typically dominates, but depending on the complexity of the target, secondary and tertiary sources of scattering can also be present (Mc Nairn & Brisco, 2004). The received backscatter type depends on different factors of both the signal and the vegetation.

Wave parameters

One must understand how different signal parameters influence the target interaction to monitor crops. The satellite and signal properties of SAR have been discussed in Section 2.2.1. Three of these properties play an important role in how electromagnetic waves interact with the vegetation: the incidence angle, frequency and polarisation.

The incidence angle is defined as the angle between the incoming radar wave and the normal of the surface. For large (shallow) incidence angle, the reflectivity generally decreases (Cable, Kovacs, Jiao, & Shang, 2011). The incidence angle also affects the path the radar wave travels through the vegetation. A small (steep) incidence angle implies a more or less vertical path through the vegetation, predominantly scanning the top part of the crops (assuming a C-band frequency). Conversely, a large angle results in a more horizontal path, measuring different characteristics, e.g. the stems. However, the angle difference should be minimised to meaningfully compare images taken from various angles (Wiseman, McNairn, Homayouni, & Shang, 2014). Figure 2.4 illustrates the relation between incidence angle and backscatter for the different polarisations. Vreugdenhil et al. (2020) has described the relationship between backscatter and incidence angle for different polarisations and surface types. For bare soil, the backscatter decreases as a function of incidence angle, as shown in Figure 2.5(a). In the case of perfectly rough soil, the incident wave will be scattered uniformly in all directions. This phenomenon is also known as Lambert scattering. Lambert scattering is common for thick vegetation canopies and is independent of incidence angle. This kind of dense vegetation mainly causes volume scattering, which is illustrated in Figure 2.5(c) for VV backscatter. Since backscatter from volume scattering is independent of incidence angle, the slope of the backscatter-incidence angle relation is almost flat (Figure 2.5(d)).

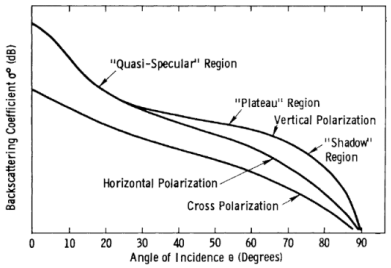

Figure 2.4: General characteristics of backscattering-coefficient variation with angle of incidence (Ulaby et al., 2019).

The wave frequency is inversely proportional to the wavelength and is defined as $f = c/\lambda$, where f is the frequency [Hz], c is the speed of light, and λ is the wavelength [m]. The dependency can already be seen in Equation 2.2, where the frequency is in the negative exponential term, i.e. the backscatter increases with an increase in frequency. The wavelength of the transmitted signal determines the penetration depth and thus the amount of interaction with the soil or the lower parts of the crops (Vreugdenhil et al., 2020). Therefore, backscattering behaviour differs between wavelengths, but since this research only considers C-band radar, this does not have to be taken into account. As mentioned previously, Sentinel-1 operates at C-band frequency, corresponding to $f = 5.4$ GHz and $\lambda = 56$ mm. This frequency does not penetrate a canopy fully (unlike L-band) and is therefore generally not sensitive to soil moisture changes or soil roughness during the growing season (Steele-Dunne, Friesen, & Van De Giesen, 2012). However, before the closure date of the crops, i.e. when soil is not completely covered, soil properties do influence the signal.

Finally, the polarisation of the radar wave influences the interaction with the vegetation (see Section 2.2.1 for the definition). This effect of vegetation on polarisation is visible when comparing Figure 2.3(b) and (c): there is no H return for bare soil, but due to the diffuse scattering in the canopy, there is a V and H return. Horizontal structures and V-polarized waves strongly reflect the incident wave with H polarisation by vertical structures. The HV and VH are sensitive to both orientations and are, therefore, indicators of random scatterers. The roughness of the soil or thickness of the vegetation also affects the degree of depolarisation d, which measures how much the polarisation of the backscattered wave varies from point to point within that target. A smooth, bare surface will have strongly polarised returns (d close to 1), while diffuse scatterers will have almost completely unpolarised returns (d close to 0) (Mc Nairn & Brisco, 2004). Thus, d increases with increasing multiple and volume scattering, depending on crop type and condition. Hinds, Sofko, Wacker, and Koehler (1993) showed that the degree of (de-)polarisation depends on crop type, growth stage and polarisa-

tion. The degree of polarisation varied throughout the growing season for the same crop type, decreasing as the vegetation developed and increasing as the crops matured and dried out.

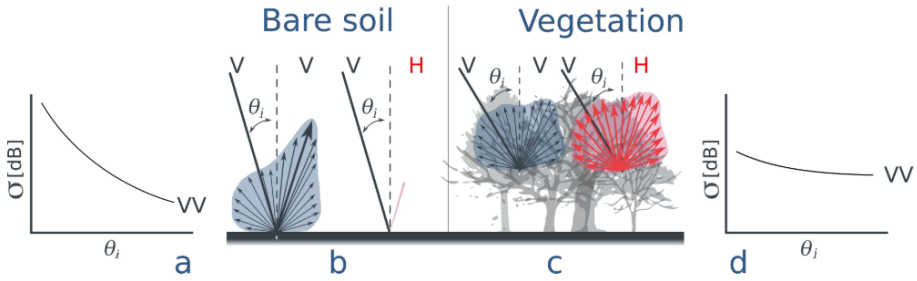

Figure 2.5: Scattering mechanisms of VV and VH polarised backscatter, where (a,b) show the relation between backscatter and incidence angle and scattering mechanisms for bare soils, and (c,d) the relation between backscatter and incidence angle and scattering mechanisms for vegetation (Vreugdenhil et al., 2020).

Figure 2.5 also demonstrates that the (de-)polarisation and scattering-type are interlinked. Vreugdenhil et al. (2020) describes how volume scattering can lead to depolarisation effects, where double- (or multiple-) bounce scattering can lead to a change in polarisation. Figure 2.5(c) shows that the return of the H-polarized backscatter is stronger in vegetation than for bare soils (Figure 2.5(b)). Hence, antennas that receive cross-polarised signals (e.g. VH) detect an increase in received energy with increasing vegetation density. This is consistent with Moreira et al. (2013), where it is described that a VH (or HV) response is strong when multiple-scattering dominates. A smooth to medium rough surface does not lead to depolarisation of the signal but does increase the received energy of the co-polarised receiving antenna (e.g. VV). However, this increase is not as strong as for the cross-polarised signal.

Terrain parameters

Once the signal has reached the surface, multiple factors can influence how the wave is scattered. Influencing factors include surface roughness, dielectric constant, geometry and agricultural practices.

The surface roughness influences the backscatter when the soil is not (yet) covered by vegetation or when the penetration depth is large enough to reach the soil. Smooth surfaces act as mirror-like reflectors, scattering the incident wave away from the radar. Rough surfaces scatter the waves in random directions, resulting in diffuse waves. Ulaby et al. (2019) has shown that σ^0 is higher for smooth soils for angles close to nadir but decreases faster with incidence angle than rougher surfaces. The authors define a surface as smooth based on the roughness (expressed in root mean square average), the wavelength and correlation length.

The dielectric constant of the surface is dependent on water content which is present in the soil and the vegetation (VWC). Ulaby (1980) describes how scattering occurs when the radar waves encounter dielectric discontinuities. The presence of water typically causes these discontinuities due to its high dielectric constant (80.4) compared to air (1) (Ulaby & El-Rayes, 1987). Interaction between the plants and radar waves is, therefore, (amongst others) driven by the volume of water in the plant. Ferrazzoli et al. (1992) reported that plant moisture (i.e. the ratio between water content and the dry biomass of plants) of cereals was rather stable during their research. Therefore, the increase or decrease in VWC is directly related to the plant's biomass.

Crop geometry is an important factor in the backscattered signal. It is an important driver for the type of backscatter and the re- or depolarisation. Plant geometry is heavily interlinked with the phenological stages, causing a crop-specific temporal profile. For instance, during the stem elongation phase of wheat, the plant structure becomes more vertically pronounced, causing an increase in σ^0_{VV} (Chakhar, Hernández-López, Ballesteros, & Moreno, 2021; Veloso et al., 2017; Vreugdenhil et al., 2018).

Besides the crops' characteristics, agricultural practices can also influence the signal. McNairn and Shang (2016) describes how physical orientation with respect to the polarisation of the incident wave can influence the amount of microwave interaction. In addition, the authors describe how planting density and row direction (relative to the range direction) could influence the SAR response. Paris (1983) also reported that the backscatter intensity is generally higher when the row direction is perpendicular to the range direction.

However, Mc Nairn and Brisco (2004) showed that the cross-polarised signal is insensitive to planting row direction, which makes VH (or HV) an important polarisation for crop monitoring. Susan Moran et al. (2012) verified this by demonstrating that cross-polarised backscatter can be used to track growth stages for grain (jointing and heading) and maize (leaf development and reproduction). Wiseman et al. (2014) observed differences in SAR response among soybean fields due to varying planting densities, even though all fields were at the same phenological stage. Patel et al. (2007) obtained similar results, reporting positive linear relationships between all polarisation types and the planting density of the *Prosopis juliflora*, a thorny plant.

A summary of all effects is visualised in Figure 2.6. When relevant, polarisation is included. For (e), the dielectric constant, the upper figure visualises the situation for a low dielectric constant, i.e. dry biomass, and the lower figure a high dielectric constant, i.e. high VWC. In the column illustrating agricultural practices (g), the upper figure illustrates the effect of high planting density, and the lower figure represents the planting direction perpendicular to the range direction. Both of these practices result in strong volumetric backscatter.

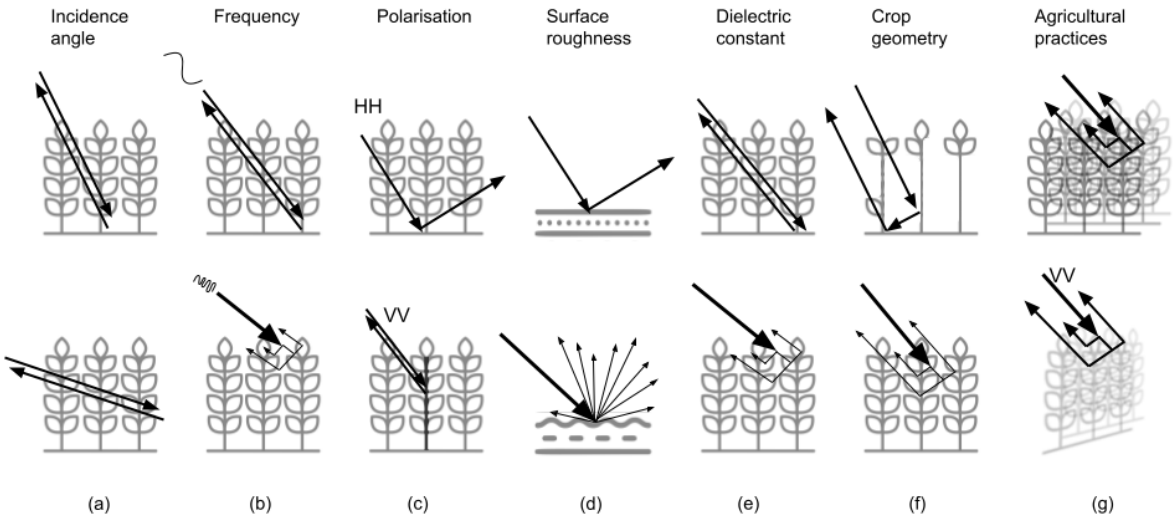

Figure 2.6: Effect of different signal and vegetation or terrain parameters. It should be noted that the differences between the upper and lower figures are illustrative and that all of the factors together make up the precise backscatter processes. Arrows indicate radar waves, and the line widths indicate backscatter intensity.

2.3. Related work

As mentioned in Section 1.1.2, there is a vast amount of literature available on both optical as well as radar remote sensing for agricultural monitoring. There, related work on agricultural remote sensing was discussed, while this section will focus on the use of NDVI for agricultural monitoring, the Cross Ratio (CR) and the temporal analysis of remote sensing signals for the crops of interest.

2.3.1. NDVI for agricultural monitoring

The NDVI is one of the earliest analytical product in remote sensing used to interpret multi-spectral imagery, and is now the most popular index for vegetation monitoring (Huang, Tang, Hupy, Wang, & Shao, 2021). The NDVI is appealing due to its ability to quickly distinguish vegetation and vegetative stress, which is useful in commercial agriculture and land-use studies. Huang et al. (2021) has reviewed different applications of NDVI data and demonstrated the increasing interest since its first use in Rouse, Haas, Schell, and Deering (1974).

The overall objective of using NDVI is to improve the analysis of vegetation information using remotely sensed data. Some examples of possible applications for the NDVI are its use for landcover classification (e.g. Pettorelli et al. (2005)), and to estimate various vegetation characteristics, such as biomass (e.g. Zhu et al. (2019)), chlorophyll content (e.g. Pastor-Guzman, Atkinson, Dash, and Rioja-Nieto (2015)), the LAI (e.g. Tian et al. (2017)), plant stress (e.g. Ji and Peters (2003)), and plant productivity (e.g. Vicente-Serrano et al. (2016)). These estimates are frequently obtained by comparing remotely sensed NDVI values to ground-measured values of these variables. Butt (2018) therefore justly pointed out that the reliability of the NDVI directly de-

termines the robustness of the NDVI-based models.

Huang et al. (2021) describes the three main limitations of NDVI as atmospheric effect, saturation phenomenon, and sensor factors. These atmospheric effects such as clouds is the cause of the low temporal resolution of NDVI in the Netherlands, and thus degrades the value of the product. Other atmospheric effects, e.g. aerosoles, are corrected for in the Sentinel-2 data (Frantz, 2019). Another limitation is the NDVI's insensitivity to changes in biomass when biomass density reaches a certain level. For maize, the NDVI already reaches saturation for a LAI of 1.5 (Thomason, Phillips, & Raymond, 2007). Lastly, Rossi et al. (2019) points out the existing inconsistencies between NDVI values obtained with different sensors. These inconsistencies were caused by sensor-specific spatial and spectral resolutions and acquisition geometries, as well as agricultural practices and crop development during the growing season.

2.3.2. Cross Ratio

Many studies (e.g. Meroni et al. (2021); Veloso et al. (2017); Vreugdenhil et al. (2020)) demonstrate the advantage of combining the polarisations into the CR. This CR is more sensitive to vegetation changes as it is less influenced by changes in soil moisture and soil-vegetation interactions. Vreugdenhil et al. (2018) demonstrated this by computing the feature importance of the VV, VH and CR for a model estimating the total VWC, where the importance of the CR was more than twice as high as that of the VV and VH (0.35 vs 0.16 and 0.17 respectively). This observation agrees with the findings of Veloso et al. (2017), who showed that the cross-polarized backscatter is more sensitive to volume scattering than co-polarised, such that the CR increases with vegetation. However, Vreugdenhil et al. (2018) discusses the challenge of isolating the influence of soil roughness and vegetation structure when using cross-polarised backscatter or the CR. Soil roughness can result in depolarisation and can have the same backscatter or CR values as a vegetated surface.

2.3.3. Temporal analysis SAR

Since C-band radar does not penetrate the ground, most studies using this frequency focus on crops with above-ground biomass, such as cereals, maize, rice, soybeans and sunflowers. As Section 2.2.3 has highlighted, backscatter depends on crop structure and vegetation water content. Since the development of the plants differ per crop type, backscatter responses differ per crop type and phenological stage of that crop during the image acquisition. Various scales to indicate these phenological stages have been developed, of which the BBCH scale is one of the most commonly used (BBA et al., 2001). A description of the crops' phenological stages and their corresponding BBCH stages can be found in Appendix A, and the same stage numbering will be used in this section and in the analysis of the temporal signal in the results. Many efforts have been made to describe this temporal signal. Mattia et al. (2003) and Wiseman et al. (2014) both found high correlations between C-band SAR responses and dry biomass for wheat, maize, canola and soybeans. Responses increased rapidly early in the growing season as biomass accumulation accelerated, leading to strong correlations with non-linear models. Wiseman et al. (2014) found the strongest correlations with dry biomass for entropy (r = 0.81 for maize), suggesting that at the start of the season, accumulation of biomass increases the randomness of the scattered signal. During seed and fruit development in the mid to late season, the rate of increase of the SAR response was reported. During these stages, the signal became more responsive to changes in growth stages rather than biomass accumulation. The study suggests that this increased sensitivity to phenological stages could partially explain the reduced sensitivity of SAR to biomass changes during this part of the growing season. Vreugdenhil et al. (2020) also offers that an increase in CR can be observed right before leaf out due to the depolarisation occurring in the multi-scattered signal. The soil-vegetation interactions via branches and stems cause this depolarisation, leading to an increase in CR. After leaf out, the leaves attenuate this soil-vegetation interaction, and volume scattering dominates.
Due to the difference in anatomy and phenological stages of the plants, the temporal behaviour can differ. For each crop, the literature on the temporal behaviour of the specific crop will be discussed. An overview of the used literature is presented in Table 2.3.

Maize

The temporal profile of the SAR signal can be discussed in terms of different stages in the growing season. Before the emergence between January and mid-May, Veloso et al. (2017) describes a decrease in VH, VV and the CR caused by the gradual smoothing of the soil with time. The temporal variations in the signal are mainly attributable to variations in soil moisture (Khabbazan et al., 2019). Both studies show that, from mid-May onwards, the slope of the S1 index becomes positive, indicating an increase in water. This period

corresponds to the expected emergence from the plants (Sibma, 1987) and is, therefore, probably caused by the increasing Vegetation Water Content (VWC). This first stage is the leaf development stage, denoted on the BBCH scale as 12 (BBA et al., 2001). C. Liu et al. (2013); Wiseman et al. (2014) report an increase in VH backscatter after emergence due to an increase in volume scattering caused by the vegetation. In 2017, Khabbazan et al. (2019) reported a crop growth of 160 cm between the 8th of June and the 10th of July. Due to this significant buildup of above-ground biomass, an increase in both the VH and CR backscatter was observed. During this period, the stem elongation stages (BBCH 31 to 39) took place, which changed the geometry of the maize plant to have a more prominent vertical structure. This change in (vertical) geometry increases the VV backscatter and the double bounce backscatter between the stalks and the soil. Veloso et al. (2017) showed that during this period, the influence of the soil becomes marginal, and the soil moisture variations do not influence the backscatter. Multiple studies (e.g. Ferrazzoli et al. (1992); Jiao et al. (2011); Vreugdenhil et al. (2018)) have shown saturation of the radar backscatter signal around this period as the LAI reaches values of 2-3. Khabbazan et al. (2019) also reported a plateau of the VH backscatter around the end of July, which corresponded to the grain development phase (BBCH 71) and the maximum height of the plants. During the final stages of late fruit development (BBCH 75) and the ripening stages (BBCH 89), Vreugdenhil et al. (2018) saw a slight decrease in CR due to the drying of the plants and thus a reduced VWC.
At parcel level, Khabbazan et al. (2019) noted abrupt decreases in backscatter between mid-September and mid-October as the maize was harvested. With the soil left bare again, the soil moisture starts to influence the backscattered signal again. Making it more difficult to detect harvest in wet autumn months.

Cereals

Cable et al. (2011) and Vreugdenhil et al. (2018) found closely related backscatter signals of wheat, barley and oat since the early growing stages and the main phenological stages are very similar. Therefore, no distinction between the cereals was made for these first stages.

As with maize, the backscatter is essentially determined by the soil before emergence (Veloso et al., 2017). At the beginning of spring (around April), the vegetation starts to emerge, causing less direct (VV) and more volume (VH) scattering. This emergence causes an increase in the CR as well. Chakhar et al. (2021) reported that, after reaching a maximum in the CR a month later, there was a decrease in CR, which can be attributed to the stem elongation stage (BBCH 30-39). The predominantly vertical structure of the cereal stems attenuates the signal (Veloso et al., 2017; Vreugdenhil et al., 2018). After the stem elongation stage, Skriver, Svendsen, and Thomsen (1999) and Larranaga, Alvarez-Mozos, Albizua, and Peters (2013) observed an increase in VH, VV and CR again, indicating the heading stage (BBCH 51-59). They attribute the increase in this period to the increase in fresh biomass. The flag leaves become less dominant within the canopy during the heading, creating a more open vertical structure. C. Liu et al. (2013) reports a decrease in CR again near the end of the growing season, indicating the end of the phenological cycle. The plants dry out, causing the radar waves to penetrate deeper, thus reducing the amount of backscatter. After harvest, all cereal crops returned to that of a rough surface as observed by McNairn, Duguay, Brisco, and Pultz (2002).

Once mature, the seed-bearing structures are very different for the three cereals, as was shown in Figure A.2b. In the late growing stages of barley (after senescence BBCH 87), Cable et al. (2011) observed an increase in VV response while VH decreased as expected due to the drying of the plant. The VV, however, was likely caused by the heads of the barley that became too heavy and leaned over. The authors found a similar backscatter behaviour for oat, except for the increase in VV. They expect this is due to the oat heads that stayed erect. Vicente-Guijalba, Martinez-Marin, and Lopez-Sanchez (2015) developed a dynamic approach for monitoring crops, among which wheat, barley and oat. They demonstrated the effectiveness for wheat and barley, but the model's sensitivity was only sufficient in the first and last stages for oats. Lopez-Sanchez, Vicente-Guijalba, David Ballester-Berman, and Cloude (2013) also reported a lower sensitivity from the radar response to oats. They attribute this to the vegetation volume, which is less dense and tall than the other cereals. Therefore the radar response does not exhibit clear variations after the end of the vegetative phase, and the contributions from the soil are more present than for the other cereals.

Table 2.3: Literature overview of sources for the time series analysis.

Crop(s)	Signal	Study area	Description	Source
Wheat, barley, rapeseed, maize, soybean, sunflower	Sentinel-1, Sentinel-2	Southwest France	Analysis of the temporal trajectory of remote sensing data for a variety of winter and summer crops that are widely cultivated.	Veloso et al. (2017)
Sugar beet, potato, maize, wheat, English rye grass	Sentinel-1	Flevopolder, the Netherlands	Time series analysis compared to ground measurements of phenological stage and height, estimation of emergence and closure dates and harvest detection using inSAR coherence.	Khabbazan et al. (2019)
Maize, wheat, soybean	Radarsat-2	Eastern Ontario, Canada	Multiyear trend analysis for crop monitoring using polarimetric synthetic aperture radar analysis based on the Pauli decomposition.	C. Liu et al. (2013)
Canola, corn, soybean, spring wheat	Radarsat-2	Western Canada	Polarimetric SAR responses of 21 parameters are compared with dry biomass over a period of 6 weeks.	Wiseman et al. (2014)
Maize, sunflower, alfalfa, wheat, barley,	DUTSCAT, ERASME, MSP	Tuscany, Italy	A comparative evaluation of the potential of active and passive microwave sensors in estimating vegetation biomass.	Ferrazzoli et al. (1992)
Maize, soybean	Radarsat-2	Ottowa, Canada	Deriving the relationship between SAR parameters at two incident angles with LAI from optical imagery.	Jiao et al. (2011)
Oilseed-rape, maize, winter cereals	Sentinel-1	Austria	Quantifying the sensitivity of backscatter and microwave indices to vegetation dynamics by applying linear and exponential models and machine learning methods to the S1 data and in-situ measurements.	Vreugdenhil et al. (2018)
Cereal, horticultural/ industrial crops, perennials, deciduous trees, legumes	Sentinel-1, Sentinel-2	Castilla La Mancha, Spain	Assessing the potential of S1 polarizations and S2 NDVI to perform crop classification and examining the temporal dynamics of the crops.	Chakhar et al. (2021)
Wheat, barley, oats, sunflower, rapeseed, peas, vetch, pastures, fallow	Radarsat-2	Pamplona, Spain	Perform a multitemporal analysis of the variations in backscatter coefficients and ratios at different polarizations due to the growth stage of each crop and establishing the optimal dates for accurate crop separation and classification.	Larranaga et al. (2013)
Barley, wheat, rape, potatoes, peas, beets	EMISAR	Central Jutland, Denmark	Analysis of polarimetric signatures with respect to incidence angle variations, between-field differences and multitemporal variations.	Skriver et al. (1999)
Barley, wheat, oat	Radarsat-2	Saskatchewan, Canada	Novel approach for real time vegetation parameter modelling.	Vicente-Guijalba et al. (2015)

2.4. Biomass Proxy

The Biomass Proxy (BP) is a fusion of the Sentinel-1 (S1) radar signal and the Sentinel-2 (S2) optical signal, providing daily and near real-time data of biomass estimations of agricultural fields. By fusing the signals, it utilises the advantages of both the NDVI (see Table 2.1) and the SAR signal (see Table 2.2). This fusion allows it to estimate the relative above-ground biomass, regardless of cloud cover and at a high spatial resolution of 10x10 meters. The input of the BP is a vector file of the agricultural field of interest. The output is two-fold, providing both a spatial (relative) distribution of biomass and an absolute value in time. Figure 2.7a shows the spatial output which is a two-dimensional representation of the field, where each pixel represents a relative measure of biomass between 0 (low biomass) and 1 (high biomass) (Planet Labs PBC, 2022). The temporal output is a time series of the expected biomass and is shown in Figure 2.7b.

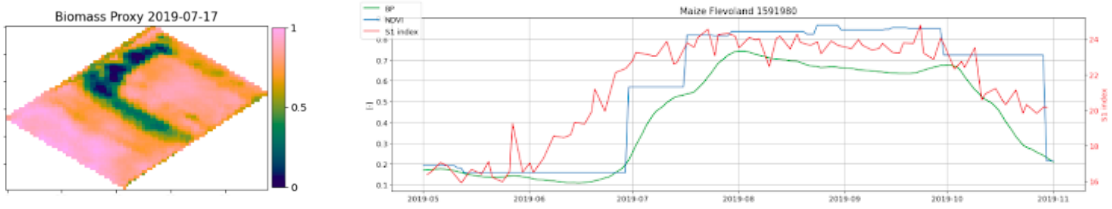

(a) The spatial output of the BP.

(b) The temporal output of the BP, where the NDVI and BP are plotted on the left y-axis and the S1 index on the right.

Figure 2.7: Examples of the Biomass Proxy output signals.

Since this study focuses on the spatial information the S1 data contains, this section will only provide in-depth information on the processing of the radar data and the fusion of the signals in the spatial domain while giving a brief description of the NDVI processing. The (radar) processing chain can roughly be segregated into three steps, which will be discussed separately in the following subsections.

Step 1) Signal preprocessing

The first step of the processing is the preprocessing of the S1 signal. This step aims to attain an image of the CR with the lowest possible amount of speckle. As discussed in Section 2.2.3, the CR can be used to minimise the influence of soil moisture on the radar signal and can be acquired by subtracting the VV polarisation band from the VH band in the logarithmic domain. The input VH and VV images are level-1 GRD images. Next, the CR image is filtered in time and space by the Lee-Sigma filter and again in space by a median filter. Lee (1983) designed the Lee-sigma filter to reduce speckle while being computationally efficient. In principle, speckle reduction for distributed scatterers requires averaging pixels within a homogeneous area. The Lee-sigma filter was introduced as a way of selecting these homogeneous areas. The filter is based on the concept that 95.5% of the pixels are distributed within the two-sigma range from its mean. Since the mean is not known *a priori*, the filter assumes the centre pixel value as the mean. The speckle can be reduced by replacing the centre pixels of a scanning window with the window's average of the pixels within the defined two-sigma range. Pixels outside this range are considered outliers, thus separating homogeneous areas and reducing speckle (Lee, Wen, Ainsworth, Chen, & Chen, 2009). Note that this is a spatial operation. The 'multi-temporal' term indicates that the filter is applied to a series of images, of which the weighted average will be taken.

Next, the median filter is applied to smooth the signal even more. The median is one of the simplest despeckling filters, in which the central pixel of a moving window is replaced by its median (Qiu, Berglund, Jensen, Thakkar, & Ren, 2004). Smith and Smitht (1996) reported that the median filter is successful at pulse- and spike noise-removal while retaining step and ramp functions, thus preserving edges between different features. However, it does not preserve single pixel-wide features, which are altered when there is speckle noise present. Lee et al. (1994) found that a 3x3 median filter is useful for preserving texture information but does not retain the mean value.

In the final step of the preprocessing, an orbit correction is applied at field level. This correction removes the bias between different orbits caused by the difference in orbit geometries. Instead of only using one orbit as is often done (except for Lievens et al. (2019); Vreugdenhil et al. (2018)), it enables the algorithm to use all available observations. The bias removal is done by identifying the different orbits iteratively and subsequently scaling the orbits to the rolling mean of all available orbits of the specified field. This step also includes filtering outliers by slope difference and a standard deviation threshold. The output of this step is a collection of rasters of the filtered CR, which are all given an offset of 30 dB. This filtered CR is the *S1 index* and will be referred to throughout this thesis as input for the BP.

The preprocessing of the optical data consists of computing the NDVI from the NIR and red band, applying a cloud mask, detecting the last full coverage or extrapolating partial coverage images and front filling for days without NDVI observations.

Step 2) Scaling

One of the key features of the BP is its global consistency. This consistency is made possible due to the consistent relationship found between the S1 index and NDVI. A global scaling parameter set was derived using this relation. The S1 index is scaled with these parameters to the same scale as the NDVI values, which is necessary for the fusion of the signals in the next step.

Step 3) Fusing S1 and S2

In the third and final step, the S1 index and the NDVI signal are fused. It is important to note that this fusion is different in the temporal and spatial domains to optimise both the high temporal resolution of the S1 index and the spatial resolution of the NDVI signal. Since this research aims to understand better the *spatial* information of S1, only the fusion process will be elaborated.

First, the weights of the fusion process are determined. These weights consider both temporal and spatial factors by defining two different weight categories: static and dynamic weights.

The static weights for the spatial domain are $w_{S1} = 0.075$ for the S1 index and $w_{S2} = 1 - w_{S1} = 0.925$ for the NDVI (S2). These values are chosen such that the contribution of the S1 signal can never exceed 40%. This limit was set in place such that users do not suddenly receive a completely different signal which they cannot interpret.

The dynamic weights of the S1 index and the NDVI are a product of the coverage of the image between no coverage (0) and full coverage (1) and a quality factor function. This function ranges between 1 and 0.1 as a function of the number of days since the last full coverage image, decreasing in an s-curve. Additionally, the quality factor of the S1 index is multiplied by the square root of the number of images within the last 24 days with a maximum of 6 days, divided by 6.

If there is no NDVI observation within the last 24 days, the most recent image is used with the lowest possible static weight ($w_{S2} = 0.1$). Since the contribution limit of S1 has a limit of 40%, the output image would still mostly consist of the outdated NDVI image. The final contribution of the S1 index (c_{s1}) is then defined as

$$c_{S1} = \frac{w_{S1} \cdot qf_{S1}}{w_{S1} \cdot qf_{S1} + w_{S2} \cdot qf_{S2,full}} \tag{2.4}$$

where w denotes the static weights and qf is the quality factor of the S1 index (S1) and NDVI (S2). The term $qf_{s2,full}$ denotes the quality factor of the last full coverage NDVI observation. An example of how this contribution would look as a function of days since the last NDVI observation is shown in Figure 2.8a. For this example, a full coverage value of 1 is assumed for the NDVI.

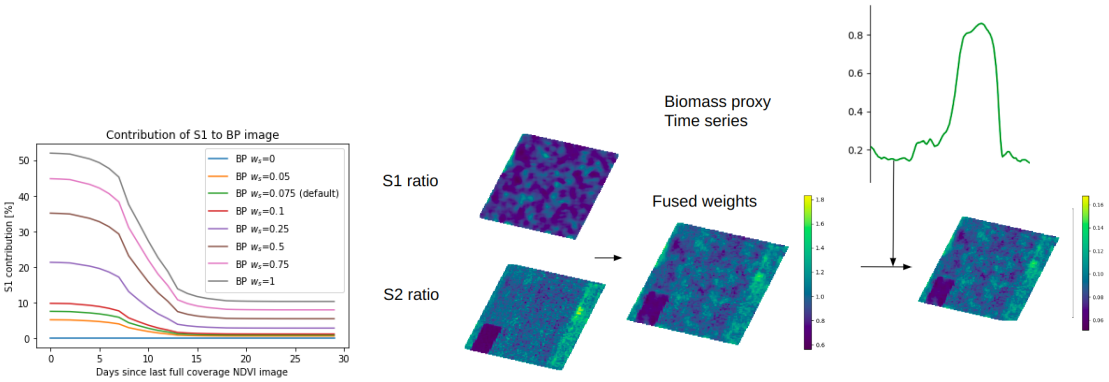

(a) Simulated contribution of the S1 index to the BP for daily full S1 coverage.

(b) Fusion process of the Biomass Proxy where the 'Fused weights' correspond to the combined static and dynamic weights following Equation (2.4).

Figure 2.8: Fusion of the NDVI and S1 index.

After the S1 index is scaled to NDVI, it is normalised and averaged over the last ~ 5 images to obtain the internal ratio. The NDVI is also normalised to an S2 ratio, after which the signals can be fused using the S1 contribution determined from the quality factors. A single image of the ratios is obtained and multiplied by the corresponding BP value from the time series.

The full processing pipeline is visualized in Figure 2.9.

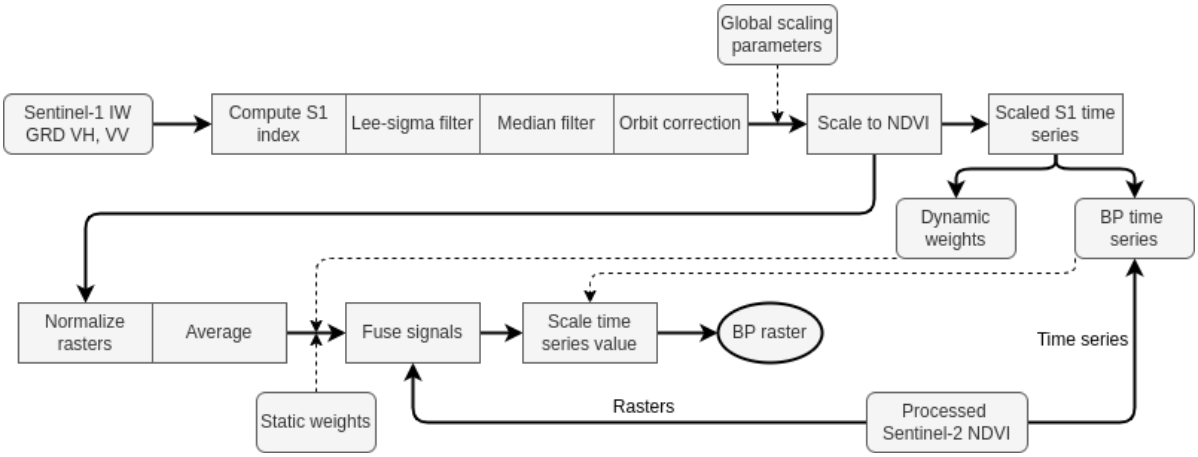

Figure 2.9: Flow chart of spatial S1 processing for the Biomass Proxy. The rounded squares denote inputs and the regular squares processing steps.

2.5. Spatial evaluation metrics

Various metrics have been tested to get an insight into which metric is most valuable to evaluate the radar data spatially. The following section will elaborate on the background of two principles from which most metrics are derived to support the analyses. This is not an exhaustive description of the used metrics but an introduction to their meaning and some of the reasoning behind it necessary to interpret the results. A complete evaluation falls outside the scope of this thesis.

2.5.1. Entropy

In 1948, Shannon introduced the concept of entropy as a measure of uncertainty associated with information. This idea stems from the information theory, in which the "informational value" of a communicated message depends on the degree to which the content of the message is surprising. If a highly probable event occurs, the message contains little information. Conversely, if an extremely unlikely event occurs, the message becomes far more informative (MacKay, 2003). So, applying this to the field of (agricultural) remote sensing, a homogeneous field will have lower entropy than a heterogeneous field since it contains less (surprising) information. Various entropy types have been applied for remote sensing analyses, e.g. Al Mashagbah (2016); Arun (2014); Gómez-Chova, Jenssen, and Camps-Valls (2012); Lu, Peng, and Lu (2006), where Shannon entropy is the most commonplace. In the field of remote sensing, entropy is also often computed from the eigenvalues of the decomposed coherency matrix, as first suggested by Robert Cloude and Pottier (1997). The found entropy values can then be used for landcover classification (e.g. Jiao et al. (2011); Nasirzadehdizaji et al. (2019)) and for identifying the dominant scattering mechanism (e.g. Alberga, Satalino, and Staykova (2008); Mc Nairn and Brisco (2004)).

For this study, however, entropy will be evaluated as *spatial metric*. Three different types of entropy were studied: Shannon, Leibovici and Altieri entropy. Contrary to Shannon entropy, Leibovici and Altieri provide information on the spatial distribution of the signals. An example of this concept is shown in Figure 2.10, and a description of each type follows.

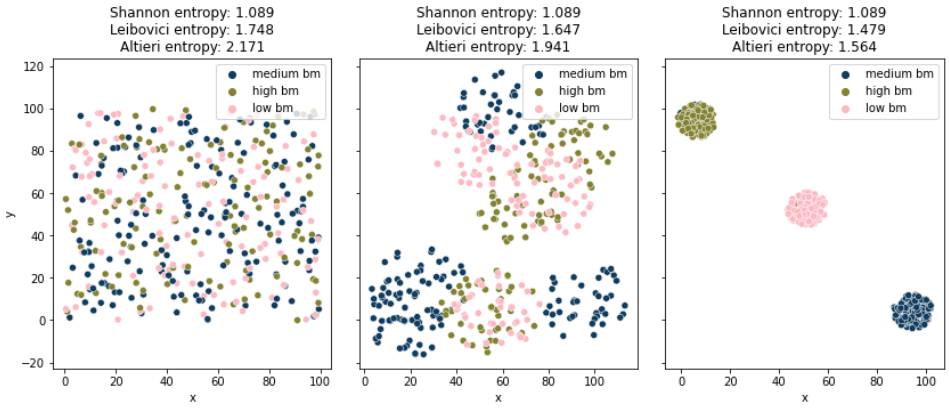

Figure 2.10: Effect of varying spatial distributions on the Shannon, Leibovici and Altieri entropy for different biomass (*bm*) distributions.

Shannon entropy

Shannon (1948) defines the information content of an event E as a function that increases as the event's probability, $p(E)$ decreases, i.e. there is more information when the specified event is unlikely. Hence, information content I reduces to zero when $p(E) \rightarrow 1$ and vice versa. The log function can satisfy these requirements, and the information content function can be defined as follows (MacKay, 2003):

$$I(E) = -log_2(p(E)) = log_2(\frac{1}{p(E)}) \tag{2.5}$$

Shannon's entropy H generalises this for a discrete random variable X and is then defined as the expected value of the information function of this variable (Shannon, 1948):

$$H(X) = E[I(p_X)] = \sum_{i=1}^{I} p(x_i) log(\frac{1}{p(x_i)}) \tag{2.6}$$

where X can assume a set of different values $x_i, i = 1,...,I$ with I the number of possible outcomes. $H(X)$ is in the range of $[0, log(I)]$, indicating that it is non-negative, and its maximum depends on the number of possible outcomes I. When X is uniformly distributed, the maximum entropy value is obtained, whereas the minimum value is obtained only in the extreme case of certainty about the variable outcome.

Note that these random variables are discrete, which is not the case for the raster data used in this thesis. Therefore, bins will be defined to categorise the numerical values.

As Figure 2.10 illustrates, the Shannon entropy is not influenced by the spatial distribution of the values. Many attempts have been made to develop Shannon's entropy further to function as an entropy measure that does capture this influence of space on variable outcomes, e.g. H. Li and Reynolds (1993); O'neill et al. (1988); Parresol and Edwards (2014); Riitters, O'neill, Wickham, and Jones (1996). These measures are often based on the co-occurrence of values or categories, which enables the measures to provide spatial information. However, many developments in this field are limited because all indices are computed conditionally on a single distance and do not cover the entire spatial configuration of the phenomenon under study. Furthermore, only some satisfy the desired additive property between local and global spatial measures (B. L. Altieri, Cocchi, & Roli, 2018). Two entropies that consider these limitations are the Leibovici and Altieri entropy. Since the Altieri entropy is a more extensive version of the Leibovici entropy, the latter will first be introduced.

Leibovici entropy

Leibovici, Claramunt, Le Guyader, and Brosset (2014) proposes a method based on co-occurrence or a set of observations located within a given spatial zone. The starting point for the spatial entropy measure is a univariate categorical value (Z) that identifies co-occurrences over space, i.e. $(x_i, x_{i'})$ with $i, i' = 1,...,I$. The order of the co-occurrences must be preserved to obtain an entropy sensitive to the spatial configuration of the co-occurrences, i.e. the realization $(x_i, x_{i'})$ with $i \neq i'$ is different from $(x_{i'}, x_i)$. The number of categories of Z is then $R = R^o = I^2$. Conversely, if the order is not preserved, $R = R^{no} = (I^2 + I)/2$. The Shannon entropy (Equation 2.6) for categorical value Z and probability mass function (pmf) $p_Z = (p(z_1), ..., p(z_R))$ then is

$$H(Z) = E[I(p_Z)] = \sum_{r=1}^{R} p(z_r) log(\frac{1}{p(z_r)}) \tag{2.7}$$

Note that because Shannon entropy does not account for spatial configurations, such that $R = R^{no}$ and $H(Z) = H(X)$. A neighbourhood definition is required to properly account for space in an entropy measure based on Z. A neighbourhood can be represented using an adjacency matrix, a square matrix whose elements indicate which realisations of X are associated to form couples. This adjacency matrix A is a symmetric, $N\,x\,N$ matrix in which $a_{uu'} = 1$ if $u' \in \mathcal{N}(u)$, the neighbourhood of spatial unit u. The diagonal elements of A will usually be zero. A subset of Z can be defined that only includes the co-occurrences identified by the non-zero elements of A, i.e. variable $Z|A$. Substituting this in the Shannon entropy (Equation 2.6) will yield a spatial entropy measure. The method deployed by Leibovici et al. (2014) uses this subset for a generic distance d. By first fixing d, a specific $Z|A$ can be defined. For each distance d, the co-occurrences can then be defined as simultaneous realizations of X at a distance $d^* \leq d$. This Leibovici adjacency matrix is denoted as L_d, which can be substituted in Equation 2.7 to obtain the Leibovici spatial entropy

$$H(Z|L_d) = E[I(p_{Z|L_d})] = \sum_{r=1}^{R^o} p(z_r|L_d)\,log(\frac{1}{p(z_r|L_d)}) \tag{2.8}$$

Note that the variable names are altered from the original formula to keep the symbols consistent and prevent confusion with the other entropies. Although this measure does indicate the spatial distribution, B. L. Altieri et al. (2018) mention two main disadvantages of this measure. Firstly, it is based on a conditional univariate distribution; thus, all results are based on an arbitrary adjacency index. Secondly, it is not decomposable, while additivity represents an appealing property in spatial statistics.

Altieri entropy

B. L. Altieri et al. (2018) proposes an enhanced version of the Leibovici entropy, also based on transformed variable Z, but with an additional variable W to represent space, thereby making it a bivariate distribution. By joining two variables, mutual information and residual entropy can be defined. Mutual information is a term from the information theory which quantifies the information shared by two variables. In contrast, residual entropy measures the amount of information on one variable after removing the effect of the other variable. The random variable W denotes intervals of all possible distances between co-occurrences as $w_k = [d_{k-1}, d_k]$, with $k = 1, ..., K$ and d_k representing the distances between points. Each distance category w_k results in the creation of a unique adjacency matrix A_k, which identifies co-occurrences at a distance w_k and thus defines the study variable $Z|A_k = Z|w_k$ with probability function $p_{Z|A_k} = p_{Z|w_k}$. As a result, K conditional univariate distributions cover the entire range of distances. This forms the basis for Altieri entropy, which can be decomposed into *spatial residual entropy* and *spatial mutual information*. These two definitions help to quantify the function of space, generalise prior spatial entropy measures, and possess the desirable additivity quality.

The variables are substituted in Shannon's entropy (Equation 2.6) to obtain the residual entropy, and a definition can be derived which can be interpreted as spatial partial entropies:

$$H(Z \mid w_k) = E\left[I\left(p_{Z|w_k}\right)\right] = \sum_{r=1}^{R^{no}} p(z_r \mid w_k) \log\left(\frac{1}{p(z_r \mid w_k)}\right) \text{ for } k = 1, \ldots, K \tag{2.9}$$

The information delivered by Z after the role of space has been regulated is quantified by each partial entropy k, conditional on a distance range w_k. This perspective enables investigation of the heterogeneity of the studied phenomenon by examining the remaining entropy given the contribution of space at various levels, i.e. partial terms consider different distance levels separately, as opposed to Leibovici's entropy, which uses a fixed distance d. By weighting the spatial partial entropies $H(Z \mid w_k)$ by the probabilities associated with each distance $p(w_k)$, the residual entropy as defined by Cover and Thomas (2005) can be formulated:

$$\begin{aligned} H(Z)_W &= E\left[H(Z \mid W)\right] = \sum_{k=1}^{K} p(w_k)\, H(Z \mid w_k) \\ &= E\left[E\left(I\left(p_{Z|w_k}\right)\right)\right] = \sum_{r=1}^{R^{no}} \sum_{k=1}^{K} p(z_r, w_k) \log\left(\frac{1}{p(z_r \mid w_k)}\right) \end{aligned} \tag{2.10}$$

This spatial global residual entropy $H(Z)_W$ controls the contribution of space and quantifies the amount of information still brought by Z after eliminating the spatial configuration W.

Cover and Thomas (2005) define mutual information as a measure of the association of two variables in terms of entropy. In particular, it measures how much information is communicated, on average, in one random variable about another. The mutual information of Z and W can be defined as follows (L. Altieri, Cocchi, & Roli, 2017)

$$MI(Z,W) = E\left[I\left(\frac{p_Z p_W}{p_{ZW}}\right)\right] = \sum_{r=1}^{R^{no}}\sum_{k=1}^{K} p(z_r, w_k)\log\left(\frac{p(z_r, w_k)}{p(z_r)\,p(w_k)}\right). \tag{2.11}$$

This MI is valuable to express as the proportional MI relative to the total entropy:

$$MI_{prop}(Z,W) = \frac{MI(Z,W)}{H(Z)} \tag{2.12}$$

This MI_{prop} essentially provides information on which percentage of the total entropy is caused by the spatial configuration of the data. Next, using the previously defined additivity property, $MI(Z,W)$ can be split into measures *partial information* (PI) as a function of k. The complete derivation falls outside this thesis's scope but can be found in B. L. Altieri et al. (2018). The definition of Altieri entropy can then be obtained by summing the residual entropy and mutual information as follows

$$\begin{aligned} H(Z) &= MI(Z,W) + H(Z)_W \\ &= \sum_{k=1}^{K} p(w_k)\,[PI(Z \mid w_k) + H(Z \mid w_k)] \end{aligned} \tag{2.13}$$

More examples of the effect of varying pmfs and spatial distributions are provided in Appendix B to aid the practical understanding of the entropies.

2.5.2. Texture analysis

Texture is a feature that characterises the spatial distribution of intensity levels in a neighbourhood of pixels. It provides information about how the different intensity levels are structured, and the information that can be retrieved from simple histogram features (Wirth, 2004). In the field of radar (remote sensing), texture becomes the spatial variation of σ^0 from one region to another Ulaby et al. (2019). Figure 2.11 shows an example of the importance of texture: the three images of the same amount of black and white pixels and thus the same intensity distribution, but have very different textures.

Figure 2.11: Example grid of binary intensity pixels, all pixels have the same intensity distribution, but different values for texture metrics (Wirth, 2004)

Texture consists of an ensemble of texture elements, also referred to as texels (Haralick, Shanmugam, & Dinstein, 1973). Each texel can describe tone, a feature based on pixel intensity properties, and structure, which describes the spatial relationship between texels. If texels are small and tonal differences between texels are large, the image has a fine texture. If texels are large and contain multiple pixels, the image will have a coarse texture (Tuceryan & Jain, 1993).

The most intuitive texture measures are range and variance within the kernel but do not provide any information about the repeating nature of texture (Wirth, 2004). A common metric that does provide information on the image structure is the Grey Level Co-occurrence Matrix (GLCM). The GLCM contains information about the positions of pixels having similar grey level values. A *co-occurrence matrix* is defined as a two-dimensional array, **P**, in which the rows and columns represent a set of possible image values. To determine

the GLCM co-occurrence matrix $\mathbf{P_d}[i, j]$, a displacement vector $\mathbf{d} = (d_x, d_y)$ must be specified and all pairs of pixels separated by $\mathbf{d}$ having grey levels i and j: $P_d[i, j] = n_{i,j}$ (Wirth, 2004). Here $n_{i,j}$ denotes the occurrences of pixel values (i, j), lying at distance $\mathbf{d}$ in the image. $\mathbf{P_d}$ has dimensions nxn, where n is the number of grey levels in the image. An example of a GLCM for $\mathbf{d} = (1, 1)$ is shown in Figure 2.12. The example image contains sixteen pixel pairs that satisfy the spatial separation, each having one of the three grey level intensities (0, 1 or 2). Therefore, $\mathbf{P}_d$ is a 3x3 matrix.

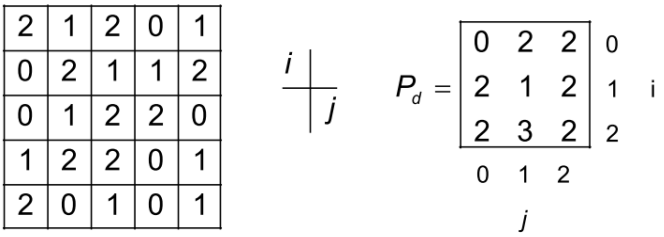

Figure 2.12: Example of a Grey Level Co-occurrence Matrix with three grey values and distance metric $\mathbf{d} = (1, 1)$ (Wirth, 2004).

GLCMs are useful for capturing texture properties of images but cannot be used for further analysis, e.g. comparing different textures. Numeric features can be computed from the matrices to represent the texture to overcome this (Tuceryan & Jain, 1993).

In this thesis, the GLCM features of the Python `PyRadiomics` (Van Griethuysen et al., 2017) package were used. An overview of these features is presented in Table 2.4.

Table 2.4: Grey Level Co-occurrence Matrix features from the *PyRadiomics* package (Van Griethuysen et al., 2017).

GLCM feature	Description	Formula
Autocorrelation	Measure of the magnitude of the fineness and coarseness of texture.	$\sum_{i=1}^{N_g}\sum_{j=1}^{N_g} p(i,j)\,i\,j$
Joint Average	Mean gray level intensity of the i distribution.	$\mu_x = \sum_{i=1}^{N_g}\sum_{j=1}^{N_g} p(i,j)\,i$
Cluster Prominence	Measure of the skewness and asymmetry of the GLCM. A higher values implies more asymmetry about the mean while a lower value indicates a peak near the mean value and less variation about the mean.	$\sum_{i=1}^{N_g}\sum_{j=1}^{N_g} \left(i+j-\mu_x-\mu_y\right)^4 p(i,j)$
Cluster Shade	Measure of the skewness and uniformity of the GLCM. A higher cluster shade implies greater asymmetry about the mean.	$\sum_{i=1}^{N_g}\sum_{j=1}^{N_g} \left(i+j-\mu_x-\mu_y\right)^3 p(i,j)$
Cluster Tendency	Measure of groupings of voxels with similar gray-level values.	$\sum_{i=1}^{N_g}\sum_{j=1}^{N_g} \left(i+j-\mu_x-\mu_y\right)^2 p(i,j)$
Contrast	Measure of the local intensity variation, favoring values away from the diagonal (i=j). A larger value correlates with a greater disparity in intensity values among neighboring voxels.	$\sum_{i=1}^{N_g}\sum_{j=1}^{N_g} \left(i-j\right) p(i,j)$
Correlation	Value between 0 (uncorrelated) and 1 (perfectly correlated) showing the linear dependency of gray level values to their respective voxels in the GLCM.	$\frac{\sum_{i=1}^{N_g}\sum_{j=1}^{N_g} p(i,j)\,i\,j-\mu_x\mu_y}{\sigma_x(i)\sigma_y(j)}$
Difference Average	Measures the relationship between occurrences of pairs with similar intensity values and occurrences of pairs with differing intensity values.	$\sum_{k=0}^{N_g-1} k p_{x-y}(k)$
Difference Entropy	Measure of the randomness/variability in neighborhood intensity value differences.	$\sum_{k=0}^{N_g-1} p_{x-y}(k)\log_2\left(p_{x-y}(k)+\epsilon\right)$
Difference Variance	Measure of heterogeneity that places higher weights on differing intensity level pairs that deviate more from the mean.	$\sum_{k=0}^{N_g-1} (k-DA)^2 p_{x-y}(k)$
Joint Energy	Measure of homogeneous patterns in the image. A greater Energy implies that there are more instances of intensity value pairs in the image that neighbor each other at higher frequencies.	$\sum_{i=1}^{N_g}\sum_{j=1}^{N_g} (p(i,j))^2$
Joint Entropy	Measure of the randomness/variability in neighborhood intensity values.	$-\sum_{i=1}^{N_g}\sum_{j=1}^{N_g} p(i,j)\log_2(p(i,j)+\epsilon)$
Informal Measure of Correlation 1 (IMC) 1	IMC1 assesses the correlation between the probability distributions of i and j (quantifying the complexity of the texture) , using mutual information I(x, y).	$\frac{HXY-HXY1}{\max(HX,HY)}$*
Informal Measure of Correlation 2 (IMC) 2	IMC2 assesses the correlation between the probability distributions of i and j (quantifying the complexity of the texture) , using mutual information I(x, y).	$\sqrt{1-e^{-2(HXY2-HXY)}}$*
Inverse Difference Moment	IDM is a measure of the local homogeneity of an image. IDM weights are the inverse of the Contrast weights (decreasing exponentially from the diagonal i=j in the GLCM).	$\sum_{k=0}^{N_g-1} \frac{p_{x-y}(k)}{1+k^2}$
Maximum Correlation Coefficient	Measure of complexity of the texture.	$MCC = \sqrt{\text{second largest eigenvalue of Q}}$ $Q(i,j) = \sum_{k=0}^{N_g} \frac{p(i,k)p(j,k)}{p_x(i)p_y(k)}$
Inverse Difference	ID is another measure of the local homogeneity of an image. With more uniform grey levels, the denominator will remain low, resulting in a higher overall value.	$\sum_{k=0}^{N_g-1} \frac{p_{x-y}(k)}{1+k}$
Inverse Variance	Inverse of the variance, where $k=0$ is skipped, since this would lead to division by 0.	$\sum_{k=0}^{N_g-1} \frac{p_{x-y}(k)}{k^2}$
Maximum Probability	Maximum Probability is occurrences of the most predominant pair of neighboring intensity values.	$\max(p(i,j))$
Sum Average	Measure of the relationship between occurrences of pairs with lower intensity values and occurrences of pairs with higher intensity values.	$\sum_{k=2}^{2N_g} p_{x+y}(k)\,k$
Sum Entropy	Sum of neighborhood intensity value differences.	$\sum_{k=2}^{2N_g} p_{x+y}(k)\log_2\left(p_{x+y}(k)+\epsilon\right)$
Sum of Squares	Measure in the distribution of neighbouring intensity level pairs about the mean intensity level in the GLCM.	$\sum_{i=1}^{N_g}\sum_{j=1}^{N_g} \left(i-\mu_x\right)^2 p(i,j)$

3

Methodology

In this chapter, the methodology of the research is presented. First, in Section 3.1, a description of the study area and the data sets used are discussed. Next, the steps to analyse the temporal and spatial behaviour resulting from changing biophysical parameters are explained in Section 3.2. Section 3.3 elaborates upon the methods to evaluate the potential of the selected spatial metrics and for what values these metrics contain valuable information. Section 3.4 then presents a method to extract temporal and spatial consistency using the spatial metrics. And finally, in Section 3.5, the steps to perform a sensitivity analysis of the Biomass Proxy to the S1 index data are described.

3.1. Data

This section contains a brief description of the study area in Section 3.1.1 and an overview of the used data in Section 3.1.2.

3.1.1. Study area

This study uses the Netherlands as case study due to its high agricultural output, frequent cloud cover, and high availability of ancillary data sets such as crop registration on parcel level and weather data. The province of Flevoland was selected as study area from all provinces based on the number of fields per crop type and field size. Figure 3.1 shows a map of Flevoland and the spatial distribution of the crops of interest. A box plot and pie chart are included to illustrate the distribution of parcel size and crop frequency. Boundaries and crop type of each parcel were determined from the Basisregistratie Gewaspercelen (BRP) (Ministerie van Economische Zaken en Klimaat, 2019).

Flevoland is a small area of reclaimed land located five meters below average sea level. The area is flat and open, and it is assumed that the climatological conditions of each parcel are the same. These conditions include an average minimum temperature during winter of -3.3°C, an average maximum temperature of 22°C during summer and a mean annual precipitation of 797 mm per year (Khabbazan et al., 2019). Because the main soil type in Flevoland is clay, it generally experiences less nutrient and water stress than other agricultural areas (Assinck, 2006).

Although the crops researched in this study are all cereals, they have slightly different growing seasons. The expected growing seasons per crop type in the Netherlands are presented in Table 3.1. These are expected sowing and harvest dates, but actual dates can deviate due to weather conditions (annual variations) and local variability between the fields. For instance, Stokkermans (2019b) reported the maize had to be harvested in September of 2018, due to a very dry summer. In 2019 however, the last maize parcels were harvested in November (Stokkermans, 2019a). Moreover, the month in which the oat is harvested is soil-type dependent. When growing on clay, the main soil type in Flevoland (Assinck, 2006), oat is usually harvested in August.

After a crop has been harvested, it is important to cover the soil with crops again as soon as possible to prevent (wind) erosion, dehydration, water stagnation and leaching of nutrients. The soil can be covered by planting cover crops: crops planted to cover the soil rather than to be harvested. In addition, well-chosen cover crops can stimulate the build-up of organic matter and nutrients in the soil (Natuur en milieu federatie,

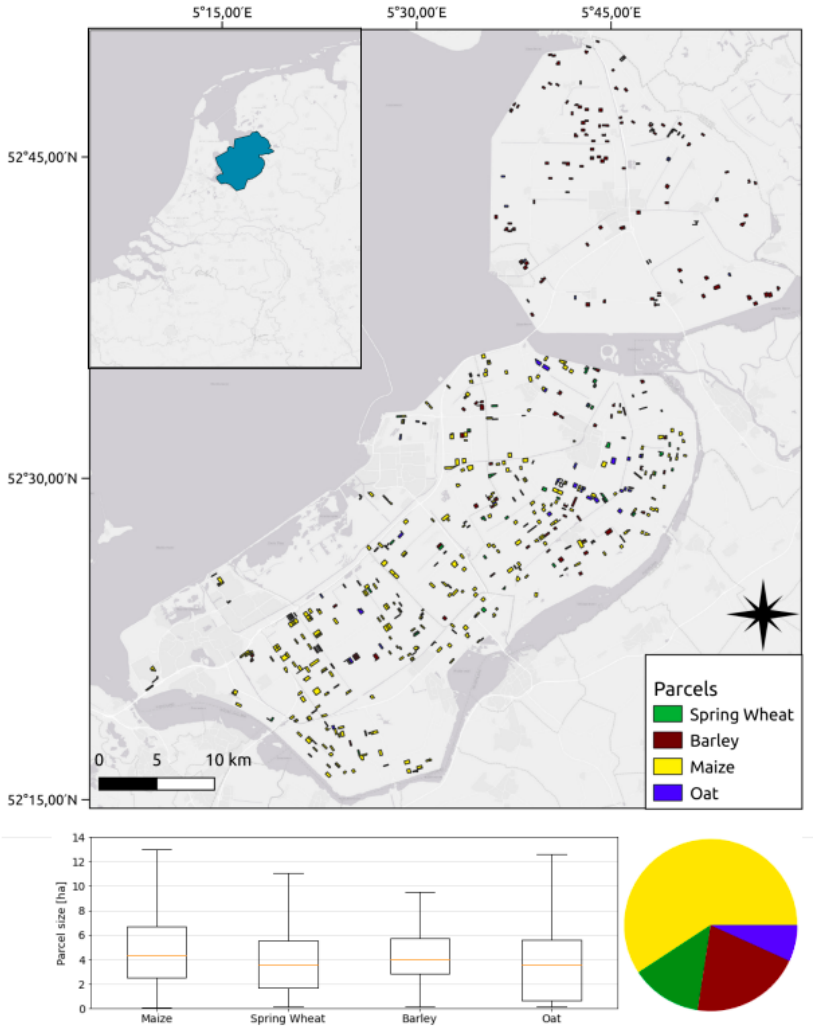

Figure 3.1: Map of all parcels in 2019 where maize, spring wheat, barley or oat is grown in Flevoland. The box plot shows the parcel sizes per crop type, and the pie charts visualize the frequency distribution per crop type.

Table 3.1: Growing season per crop type in the Netherlands (Interreg III, n.d.; Met, 1994; Praktijkonderzoek et al., 1999; Sibma, 1987).

Crop	Sewing	Harvest
Maize	Apr	Sep - Oct
Spring Wheat	Mar - Apr	Aug
Barley	Feb - Apr	Aug
Oat	Feb - Apr	Jul - Aug

n.d.). Since 2006 it has been mandatory in the Netherlands to grow a catch crop after growing maize on sandy or loess soil. The final sowing dates are set by law to ensure that this catch crop has time to grow. For undersowing or sowing directly after harvest, this final date is October 1. A new main crop has to be sown before the October 31. These catch crops absorb enough nitrogen from the soil that has not been used by the maize (Rijksdienst voor Ondernemend Nederland, 2019).

3.1.2. Data sets

Weather station data

Hydrometeorological data can provide necessary information to understand the radar signal, which can be strongly influenced by precipitation and frozen soils (Veloso et al., 2017). Besides that, strong wind gusts could change the geometry of the vegetation (Tan, Wu, Yan, & Zeng, 2018). Figure 3.2 visualizes the meteo-

rological data collected by the KNMI in Lelystad (KNMI, n.d.). Total precipitation in 2019 was 735.5 mm, of which 20% fell in October. The warmest month was June, and the coldest was January, in which there were seven consecutive days of sub-zero daily mean temperatures recorded.

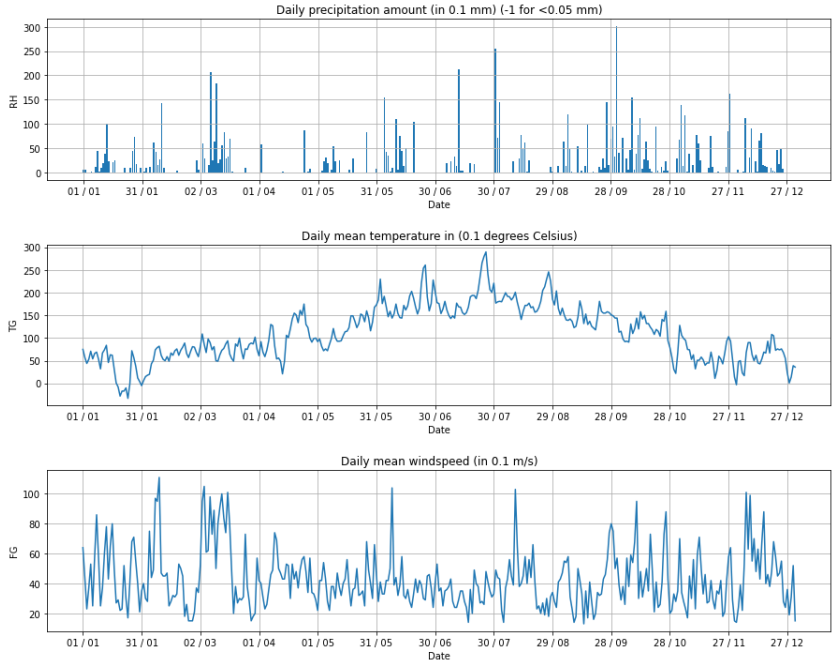

Figure 3.2: Meteorological data collected at the Lelystad KNMI weather station in 2019.

Basisregistratie gewaspercelen

The *Basisregistratie gewaspercelen* (BRP) is a data set provided by the Dutch government containing the locations of all agricultural parcels with their corresponding crop type (Ministerie van Economische Zaken en Klimaat, 2019). A new data set is generated yearly around the 15th of May. Each parcel has a corresponding category (grassland or agricultural land), crop type (e.g. spring wheat, maize silage, oat), crop code, year, field size, geometry and status (pending or confirmed). The data sets before 2020 also contain the parcel size as a feature.

Since this study only focuses on the previously described crops and the province of Flevoland, the data set was filtered based on these features. Another feature was added to combine the different plant varieties of a certain crop, e.g. 'maize silage' and 'sugar maize' both got the label 'maize'. This label was used to filter the crops that showed a similar backscatter response in the SAR and NDVI time series.

Besides location and crop type, the BRP data was filtered based on field size. This filtering was done because of a weak ($r \approx 0.22$) but significant ($p < 0.05$) correlation between field size and deviation from the mean. By removing the 10th percentile of the fields based on size, extremely small fields were removed. These very small fields often seemed incorrect and caused outliers. The total amount of parcels processed per crop type after the field size filters can be seen in Table 3.2. Note that, since the crop types were processed separately, this filtering was performed for each crop, causing a slightly different frequency distribution than presented in Figure 3.1.

Table 3.2: Number of processed parcels of each crop type.

Crop	**Nr. of parcels**
Maize	309
Spring wheat	56
Barley	180
Oat	59

Note that the BP is not dependent on an ancillary data set such as the BRP since the algorithm is capable of field delineation and uses global scaling parameters applicable to all crop types.

Field measurements Flevoland 2017

Unfortunately, no ground data was available to validate the results. However, Khabbazan et al. were kind enough to share the field measurements taken in their campaign in 2017. The field measurements include crop height, BBCH stage and soil moisture for maize and other crops, which are not analyzed for this study. The data was collected between the 18th of May and the 17th of August for five maize parcels. Meteorologically, the summers of 2017 and 2019 were both warm, but in 2019 precipitation values were lower than average (KNMI, n.d.). The data was, therefore, not used directly as validation but more as a benchmark.

Sentinel-1 data

The SAR data in this study is acquired by the Sentinel-1 (S1) satellites. The Copernicus Sentinel data 2019 was obtained from the Planet database, a collection of the data retrieved from the Sentinel Hub. S1 is an imaging radar mission based on a constellation of two satellites, equipped with a C-band SAR sensor which operates at a centre frequency of 5.405 GHz (Valero et al., 2021). Over (non-polar) land, it utilizes the Interferometric Wide (IW) swath mode, which provides dual polarization (VV and VH) with a spatial resolution of 20 meters (Khabbazan et al., 2019). By combining the data from the Sentinel-1A and 1B satellites, the Netherlands is covered by six relative orbits. Each relative orbit is described in Table 3.3. Unfortunately, on December 23 2021 the Sentinel-1B satellite ceased collecting data. Afterwards, only Sentinel-1A data is provided, decreasing the frequency of SAR observations. This study uses Sentinel-1A and B images before this outage, between the January 1, 2019, to the December 31, 2019. With Sentinel-1A and -1B in operation and a ground swath width of 250 km, the local temporal revisit time is 1.5–4 days over Europe (all orbits active). However, due to the acquisition scheme's energy-related limitations, this reduces to 6–12 days globally (down to only 1–2 orbits) (Vreugdenhil et al., 2020).

Table 3.3: Sentinel-1 IW data available over the study area in 2019.

Relative Orbit	Pass	Local Time	Min. Inc. Angle (°)	Max. Inc. Angle (°)
37	DESC	06:49	38.9	41.9
110	DESC	06:58	30.0	33.7
15	ASC	18:15	30.0	31.5
88	ASC	18:24	36.6	40.4
161	ASC	18:32	44.7	46.1

In many studies, a single orbit is selected to eliminate the effect of different incident angles and overpass times. For this study, however, all orbits are considered to maximize the available information. Using all orbits is possible because of the Biomass Proxy orbit correction (see Section 2.4): a preprocessing function used in the algorithm that 'learns' and corrects for the biases caused by the differences in relative orbit. The functionality of this orbit correction was tested by checking the influence of the relative orbits and the time of day of the image acquisition. The relative orbits were encoded, and acquisition times were divided into 'morning' and 'evening' and binary encoded. Then Pearson's r and its corresponding p-value between the deviation from the mean of all fields in a province and the relative orbit/acquisition time was computed. Except for maize and oat in Flevoland, the correlation between all crops and the relative orbits and acquisition times were insignificant ($p>0.05$). Maize and oat in Flevoland had a significant ($p<0.05$) but weak correlation of 0.19 and 0.21, respectively. Therefore it can be concluded that the relative orbit and acquisition times do not significantly influence the observations after the orbit correction, and thus all relative orbits can be used.

Sentinel-2 data

The NDVI data used in this study is acquired by the two Sentinel-2 (S2) satellites, which both carry a Multi-Spectral Instrument (MSI) at Level 1C (Blickensdörfer et al., 2022). The MSI samples thirteen spectral bands: four bands at 10m resolution, including visible and near-infrared (NIR), six bands at 20m and three bands at 60m spatial resolution (Chang & Shoshany, 2016). S2 is very suitable to map the NDVI since both the Red and NIR bands have a high (10m) resolution. The revisit time of a single satellite (A or B) is 10 days, so an image can be obtained by using both every 5 days. However, only a subset of these images is usable due to the cloud cover. The S2 data was also obtained from the Planet database.

3.2. Understanding the temporal and spatial behaviour of crops

In order to evaluate the potential of the SAR signal in the BP, a general understanding of the field data is indispensable. Although this research mainly focuses on data processing in the spatial domain, understanding temporal behaviour is the first step to linking the biophysical processes to what we see in the spatial field data. Therefore, Section 3.2.1 will go into the methods to analyse the temporal behaviour of the specified crops. Subsequently, Section 3.2.2 will discuss the methods to analyse the spatial behaviour of a subset of the fields.

3.2.1. Temporal behaviour

This method aims to link the temporal behaviour observed in the selected fields to the biophysical processes observed in the literature discussed in Section 2.2.3. Since the crops have (slightly) different structures and biomass, they are analysed separately and compared to the literature on the specific crop. It was assumed that the crops have similar temporal behaviours for the different years and regions in the other studies.

The uniform averages of the NDVI, VH, VV and S1 index signals were computed to minimise the influence of outliers and create a non-specific temporal profile. This averaging was done for each crop type for all fields. The time series plots were made to visualise the profile of the four signals. A threshold was applied to exclude extreme values from the S1 index time series based on a single or few fields. These outliers were often caused by fields at the edge of a swath, which were not averaged out by enough other fields. This threshold was set to 10% of the total fields, meaning that for each date plotted, at least 10% of the fields must have a value. An example of this filtering is provided in Appendix D.

The standard deviations of the NDVI and S1 index were computed and included in the plots to illustrate the variability between fields. Next, the extreme weather events, i.e. droughts, heavy precipitation and strong winds, were compared with the time series to take variations from these causes into account. Finally, an approximation of the growing stages was made using the validated temporal profiles discussed in Section 2.2.3.

As discussed in Section 3.1.2, no validation data was available to validate the approximations. However, to support the analysis, the data of the 2017 field campaign, together with the time series from the corresponding research (Khabbazan et al. (2019)), was compared with the 2019 time series.

3.2.2. Spatial behaviour

A subset of the processed fields needed to be selected to analyse the spatial behaviour of the signals. This way, spatial (raster) data could be visualised and qualitatively and quantitatively described. First, a minimum area threshold of six hectares (A_{min} = 6 ha) was set to reduce the number of fields. A_{min} was selected for two reasons. Firstly, it ensures a sufficiently large area to see large-scale spatial patterns since the BP spatial filtering is at the scale of one hectare. Secondly, each crop type still had a minimum of ten fields in its subset after applying the threshold, reducing the chance of selecting an outlier.

Subsequently, a single field was chosen from this subset to visualise the raster data. The temporal profiles of the individual fields were compared with the mean to select a representative field from the subset. The field with the smallest Root Mean Squared Error (RMSE) from the mean was chosen for each crop, thus assuming this field is also the most representative in the spatial domain. The time series of all fields were plotted for each crop type, with the selected field and mean highlighted to picture the temporal similarities and differences of the selected field.

After the field selection, the visualisation date(s) needed to be chosen. To account for differences in (spatial) signals during different periods in the growing season, the analysis of the temporal behaviour as described in Section 3.2.1, time series of the S1 index and NDVI were plotted and were (roughly) divided into the principal growing stages of the specified crop. A date was selected in each growing stage on a day with an NDVI observation such that the signals could be compared with minimal external differences. The selected dates were then labelled and plotted in the time series.

Finally, the S1 index, NDVI, VH, VV and CR were plotted for each field and date. The CR was computed by subtracting the VV raster from the VH raster in the logarithmic domain. To compare the rasters not only qualitatively but also quantitatively, the histogram of each raster was plotted above the respective raster. In the histogram plot, the mean μ, standard deviation σ, and coefficient of variation $CV = \frac{\sigma}{\mu}$ were added to support quick comparisons. The coefficient of variation (CV) is a statistical measure of how far apart data points in a series are from the mean (Brown, 1998). Even when the means of two data series strongly differ,

the CV can be used to compare the degree of variation between the two data sets. It is therefore a suitable statistical feature to compare the different dates and signals.

3.3. Cluster detection with spatial metrics

Once the rasters are obtained for the different crops, they can be analysed to evaluate if they contain spatial information that is of interest to include in the Biomass Proxy. This section present a method to answer the second research question: *'What spatial metrics can be used in which situations as indicators for clustering of the spatial S1 index data?'*

The methodology steps are all performed sequentially; therefore, the same fields are used for the spatial analysis of Section 3.2. Since the research objective is to analyse when there is relevant spatial information in the S1 index signal, only computations on the S1 index rasters are performed.

3.3.1. Metric selection

This step aimed to select metrics that best describe spatial information that is expected to be relevant. This *relevant* spatial information is defined as spatial behaviour that could potentially indicate large changes or anomalies in the field that would be of interest to the user. To detect this kind of behaviour in the spatial data, three characteristics are deemed important:

1. the amount of clustering, i.e. the grouping of similar backscatter values
2. the size of the clusters
3. the contrast between the clusters and their surrounding

Here it was assumed that change happens in a certain area of the fields, that small changes are more likely to be an artefact of the radar or simply irrelevant, and that higher contrast increases the probability of the cluster being an anomaly. With these specifications in mind, three metrics were selected, and their potential to describe the spatial data was analysed.

In order to select suitable metrics, the Shannon, Leibovici and Altieri entropy and several Grey Level Co-Occurrence Matrix (GLCM) metrics were computed. For each field, the metrics were computed during the crop-specific growing season. First, the different types of entropy were computed using a Python version of the R-package *Spatentropy* (Milk, 2021; Parresol & Edwards, 2014).

The values had to be discretised to compute the entropies. Bins of 0.1 dB were defined, and every pixel was assigned to its corresponding bin. The Shannon, Leibovici, and Altieri entropy were computed using Equation (2.6), Equation (2.8), and Equation (2.13) respectively.

The default distance values were used for both the Leibovici and Altieri entropy, which correspond to $d_{Leibovici} = 10$ and $d_{Altieri} = [0, 10]$. Since Altieri entropy works with distance intervals, $d_{Altieri} = [0, 10]$ is divided into $k = 10$ intervals w_k, for which the partial entropies are computed.

Subsequently, the GLCM metrics were computed with the Python `PyRadiomics` package (Van Griethuysen et al., 2017). This package computes the twenty-four different GLCM features discussed in Section 2.5.2. To use the functions, all rasters first had to be converted to `SimpleITK` (Insight Segmentation and Registration Toolkit) image format, which is a Python class built for image analysis (Beare, Lowekamp, & Yaniv, 2018).

The selection of the metrics was done by first analysing the metrics visually based on their ability to describe rasters with the described desired characteristics, and then by substantiating the selected metrics with the theory.

For each field, these metrics were computed during the growing season. In order to compare different metrics and crops, the data set was duplicated and normalised using min-max normalisation. Subsequently, each metric's minimum and maximum values were identified to select the metrics that best reflect the large-scale patterns, and their corresponding S1 index rasters were plotted. For each metric, subplots were made showing the S1 index rasters for the highest and lowest metric values of the growing season. The metrics that seemed to represent clusters most clearly, i.e. the maximum values showed clear clusters were selected.

metrics that met these requirements best were:

1. Altieri entropy
2. Cluster tendency
3. Cluster prominence

To motivate the choice for the Altieri entropy further, the theoretical background (Section 2.5) has highlighted its ability to describe the heterogeneity and the mutual information (MI) of the raster data. Both contain valuable information, since, ideally, it would be valuable to know when there are clusters (MI) if the field is not homogeneous (residual entropy). Thus, a change in the Altieri entropy indicates when the distribution of backscatter values changes and if these values are clustered. The equation for the Altieri entropy is given by Equation (2.13), and a more comprehensive explanation can be found in Section 2.5.

As their names suggest, the cluster tendency and cluster prominence are intuitive measures of clustering. The cluster tendency is a GLCM feature that measures groupings of voxels with similar grey-level values (Van Griethuysen et al., 2017). It is defined as

$$\text{cluster tendency} = \sum_{i=1}^{N_g} \sum_{j=1}^{N_g} \left(i + j - \mu_x - \mu_y\right)^2 p(i,j) \tag{3.1}$$

where N_g is the number of discrete interval levels in the image, i, j the (row, column) index values of the GLCM, $p(i,j)$ the normalised co-occurrence matrix, and μ_x and μ_y the mean grey level intensity of the marginal row and column probabilities respectively. These marginal row/column probabilities can be expressed as $p_x(i) = \sum_{j=1}^{N_g} p(i,j)$ and $p_y(j) = \sum_{i=1}^{N_g} p(i,j)$, such that $\mu_x = \sum_{i=1}^{N_g} p_x(i)\,i$ and $\mu_y = \sum_{j=1}^{N_g} p_y(j)\,j$.

The cluster prominence measures the skewness and asymmetry of the GLCM. A higher value implies more asymmetry about the mean, while a lower value indicates a peak near the mean value and less variation about the mean. It has the same variables as the cluster tendency and is defined as (Van Griethuysen et al., 2017)

$$\text{cluster prominence} = \sum_{i=1}^{N_g} \sum_{j=1}^{N_g} \left(i + j - \mu_x - \mu_y\right)^4 p(i,j) \tag{3.2}$$

Since all metrics provide field averages, understanding values at field-level is not always straight-forward. To support the analysis, the MI and residual entropy are used for the Altieri entropy. For the GLCM metrics, a voxel-based computation of the metrics was performed to visualise what aspects of each raster cause the high or low values. The voxels were defined as the same size as the pixels in the raster to keep the same spatial resolution. The output of these computations was two-dimensional *feature maps*.

3.3.2. Metric analysis

To better understand the information the metrics contain, an analysis for each of the selected metrics was performed, evaluating the information it describes and its computation time. This analysis consists of two parts. First, the time series of the metrics were compared with the S1 index time series. For each field, when there was a sudden change in the S1 index, the S1 index rasters were plotted with their corresponding metric values to see how these metrics represent these changes. These sudden changes usually corresponded to the (expected) harvest time.

Second, the time series of the three metrics were compared for each field. Dates were extracted where the metrics showed similar values and where the largest differences occurred. Again, the S1 index rasters corresponding to these dates were plotted and analysed.

Furthermore, to support the analysis, the feature maps of the GLCM features were plotted where deemed appropriate. Since this is not a function of the `SpatEntropy`, which is used to compute Altieri entropy, the analysis of this metric was supported by evaluating the residual entropy and the MI.

3.3.3. Defining thresholds

This step aims to identify suitable thresholds for each metric, such that they can be used as indicators when the S1 index raster contains relevant spatial information and the analysis can be quantified. To prevent overfitting the value to one field, for each crop, four other fields were randomly selected from the subset, which was filtered by size. For each metric and field, the S1 index rasters were sorted according to their metric value and plotted in descending order. A threshold was chosen by visual inspection for the same requirements as for the metric selection, with the specifications further refined as follows:

1. the raster contains at least two recognisable clusters of at least 10 pixels
2. at least one cluster covers an area of at least 20 pixels
3. at least one cluster has an edge with high contrast, where 'high' is defined as more than 1 dB difference

The metric values were converted back to the absolute values and averaged to define a crop-based threshold.

3.4. Pattern consistency

As previously mentioned in Section 1.2, this method is based on the premise that consistent patterns contain relevant information and quickly fluctuating areas or pixels do not. With the framework to test and select spatial features of the raster data developed, the next step was to analyse these persistent clusters in time and space. An overview of the steps in this method is presented in Figure 3.3.

3.4.1. Temporal consistency

The spatial (auto)correlation can be computed between sequential rasters to test whether spatial data is consistent in time. For each field, the spatial correlation between raster i and $i-1$ was computed for $i = 2, ..., N$ with N the number of available rasters in the growing season. The correlation was computed backwards to be applied near real-time. The correlation value and its corresponding p-value were obtained using the Pearson correlation function of the Python package `Scipy Stats` (Virtanen et al., 2020). If a correlation was significant ($p < 0.05$), the correlation coefficient was included in the analysis. Next, a time series from the autocorrelation values was created for each field. Following the definition of Greenwood (2014), a correlation is defined as 'strong' if $r > 0.5$. Therefore, to visualise potentially relevant periods, values in the time series were marked if two or more sequential data points had values above 0.5.

Since high correlation could also indicate consistency in completely homo- or heterogeneous rasters, the periods with high correlations were also tested against the different metrics defined in the previous section. The metric time series were marked above their threshold value and were plotted together with the autocorrelation time series. The dates of the periods which met the conditions were extracted, and the corresponding S1 index rasters were plotted to verify the expected consistent patterns. This step is denoted as (1) in Figure 3.3.

This temporal analysis was also performed on a larger scale by applying the described steps to all fields. To analyse whether there is a higher probability of persistent patterns during certain stages of the growing season, a plot of the distribution of occurrences was made per crop type. The plot is based on the histogram where each bin represents a date, and the count corresponds to the number of times a raster on a specific day is part of a persistent pattern. To compare the histogram profiles between the different crops, the values were normalised by dividing the count by the total number of fields of the specified crop.

3.4.2. Spatial consistency

After obtaining the temporal occurrence of persistent patterns, the patterns were analysed spatially. This spatial analysis was done for two reasons. The first reason is better to understand the spatial information, i.e. determine typical cluster characteristics (such as shape, size and average value) and to compare the clusters with the NDVI observations in the selected period. This both aids the understanding of what could cause the signal (can the pattern also be recognised by optical imagery?) and demonstrate the relevance of the radar data. The second reason is to set out a framework on how the information could be used to redefine the weights in the fusion process of the BP.

The steps taken to extract these spatial patterns are illustrated in Figure 3.3. The numbers from each processing step correspond to the following description. Step 1 was to select a (sequential) series of rasters (R) for each crop defined as $R_d(i, j)$ for $d = 1, .., N$ with N the number of days in the series and (i, j) the pixel values. In step 2, the rasters were scaled to their internal ratio, i.e. each scaled was expressed in $R^s_d(i, j) = X^* \mu_{R_d}$, where μ_{R_d} corresponds to the mean of the field on day d. Step 3 includes averaging the series $(\mu_{R^s(i,j)})$ in time. Then, in step 4, the average was subtracted from each raster in the series: $\delta R_d(i, j) = R^s_d(i, j) - \mu_{R^s(i,j)}$. In step 5, a boolean mask was created from the pixels where $\delta R_d(i, j) < 0.1$. Note that the ratio was taken such that these differences are only based on the spatial pattern. Otherwise, the first and last rasters in a series would be disadvantaged when there is biomass growth.

Once a mask was obtained for each raster in the series, the masks were combined to represent the pixels that remained consistent throughout the series in step 6. The combination was done by setting the condition

that all rasters must have the same boolean value (True). Next, in step 7, clusters (adjacent pixels with *True* values) were filtered by size, such that clusters with less than 5 pixels were removed and holes of less than 5 pixels were filled. Two morphological operations were performed using the `Scikit` Python package (Pedregosa et al., 2011). The final mask was then applied to the raster series in step 8, to visualise which parts of the field were classified as persistent.

Finally, the persistent spatial patterns of these rasters were compared with the NDVI rasters in the same period. This was done for two reasons: 1) to evaluate the relevance of the persistent radar patterns, i.e. could these persistent patterns have been detected from optical imagery, and 2) to identify possible causes of the pattern, i.e. if the NDVI observation does not show the same pattern the possible causes could be reduced (dependent on the time in the growing season).

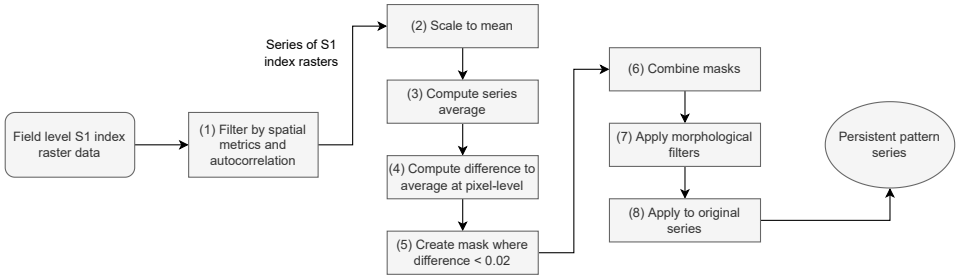

Figure 3.3: Methodology steps of extracting persistent patterns spatially.

3.5. Implementing spatial data in the Biomass Proxy

To answer the question '*How is the Biomass Proxy influenced by the static weight of the Sentinel-1 data, and how does this change throughout the growing season?*', a sensitivity analysis of the static weights on the Biomass Proxy was performed. The eventual objective was to find the 'tipping point' of when radar patterns become predominant in the BP. This is crucial information to determine how to include the spatial S1 information in the output signal.

3.5.1. Processing BP for varying static weight

The BP was processed for various static weights to perform the sensitivity analysis. As mentioned in step 4 of Section 2.4, the static weight is defined to range between 0 and 1. For the analysis, the BP was computed for static weights of 0, 0.1, 0.25, 0.5, 0.75 and 1. In the analysis, the default value of 0.075 was also considered.

3.5.2. Identifying radar-like spatial patterns

For visualization purposes, a distinction was made between the rasters shown in 2D and crop averages. The K-means clustering was only performed for these rasters. The dates of the plots were chosen to coincide with an NDVI observation again. The S1 index, NDVI and weighted BP rasters were then plotted beside each other and qualitatively described.

In order to quantify when radar characteristics become visible, a K-means clustering algorithm from the Python library `Scikit-learn` (Pedregosa et al., 2011) was applied. The *Silhouette score* was used to determine the optimal number of clusters. This method was chosen over the elbow method since determining 'the elbow' can be ambiguous. In a few small tests, the Silhouette score always had the same outcome as the Davies-Bouldin index but a slightly shorter computation time. It was therefore used to determine the optimal cluster number. The distance metric used is the Euclidean distance. A visual inspection was done for each field with different weights to see when patterns became visible in the BP rasters.

3.5.3. Determining spatial correlation

In order to visualize the spatial relation between the weighted BP rasters for all fields, the spatial Pearson correlation and its corresponding p-value were computed between the rasters and the S1 index and NDVI using the `Scipy Signal` Python package (Virtanen et al., 2020). If the correlation between two rasters was significant ($p < 0.05$), the correlation value was included in the computation. These correlations were computed for each field and date in the growing season and averaged for the different static weights. The start and end date of the growing season were taken as the first of the months specified in Table 3.1. Combining this throughout

the growing season defined a relationship for each crop. The intersection point between the correlation with the S1 index and the correlation with the NDVI signal was then determined from the plot to extract the value above which static weight the output signal is more similar to the S1 index than NDVI. Finally, the intersection points of the different crops were compared.

4

Results & Discussion

This chapter presents the results obtained in this study. To improve readability, each result is directly discussed. The main sections of this chapter are structured the same way as the methodology. First, the temporal and spatial analysis of the SAR and NDVI signals are analysed for the four crops in Section 4.1. Then, in Section 4.2, the selected metrics are discussed and a suitable threshold is selected. Next, Section 4.3 provides the findings on when and where persistent patterns occur. Last, the results from sensitivity analysis of the BP to the static weights is presented in Section 4.4.

4.1. Understanding the temporal and spatial behaviour of crops

In order to finally be able to redistribute weights between the SAR and NDVI signals, one must understand the information the signals contain. This chapter will therefore go into the question: *'How do NDVI and SAR data describe biophysical changes in the temporal and spatial domains?'*. Both the temporal as well as the spatial aspect of the signals are analysed per crop type to answer this question, which will be done in Section 4.1.1 and Section 4.1.2 respectively. Descriptions of the phenological stages used in the analysis can be found in Appendix A.

4.1.1. Temporal behaviour

Figure 4.1 illustrates the S1 index and NDVI signal of the four summer crops. The time series show that barley, oat, and wheat have a similar growing season, which could be expected from the literature (or Table 3.1). As expected, the growing season of maize starts later and continues after the other cereals are already harvested.

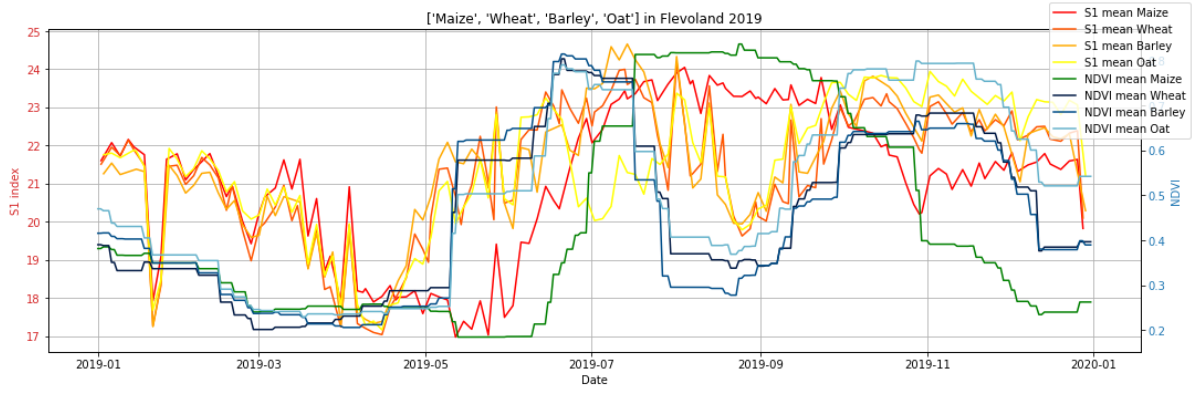

Figure 4.1: S1 index time series of maize, wheat, barley and oats.

Besides a similar growing season, barley, oat and wheat all show an increase in S1 index and NDVI signal after harvest. This could be caused by the radar backscatter of cover crops, the backscatter of crop residue, the influence of soil moisture, or a combination of the three.

All crops show a sharp drop in the S1 index in January but not in the NDVI signal. The days this occurs correspond to the days where the daily mean temperature was sub-zero (see Section 3.1.2). All crops also show an increase at the beginning of March and a sharp peak on April 1. Looking back at Figure 3.2, it is clear that these periods of increased S1 index coincide with increased precipitation. Since the soil is not yet covered with crops in this period, the S1 index is mostly affected by soil moisture.

Maize

Figure 4.2 shows the time series of the S1 backscatter (VV, VH and S1 index) and the NDVI signal of all maize parcels in Flevoland. Between January 1 and mid-May, the S1 index slowly decreased, with a few exceptions caused by weather conditions, as stated above. This decrease is also visible in VH and VV, which agrees with the findings of Veloso et al. (2017), who attributed this to the smoothing of the soil. From mid-May onwards, the slope of the S1 index becomes positive, indicating an increase in water. This period corresponds to the expected emergence from the plants (Sibma, 1987) and is, therefore, probably caused by the increasing VWC. Note that the NDVI signal is not sensitive yet to the small plants. Only ten days later, when the chlorophyll in the leaves starts to develop, does the signal start to increase.

After initial emergence (BBCH 10), VH backscatter (and therefore S1 index) start to increase because the vegetation provides the main volume scattering contribution to the backscattered signal. This is analogous to the results of C. Liu et al. (2013) and Wiseman et al. (2014). The same authors both subsequently saw an increase in VV, which can also be observed in Figure 4.2 at the start of July. This is presumably due to the stem elongation stages (BBCH 31-39), in which the vertical structure of the stalks reflects the VV backscatter more strongly and the double bounce backscatter between the stalks and soil increases. Recall from Veloso et al. (2017) that during this period, the influence of the soil becomes marginal, and the soil moisture variations do not influence the backscatter. This corresponds to the presented time series when this is compared to the precipitation data from Section 3.1.2: on July 10 and 30, heavy precipitation was recorded, which is not visible in the S1 index time series.

At the end of July, the VH backscatter and S1 index start to plateau. Multiple studies (e.g. Ferrazzoli et al. (1992); Jiao et al. (2011); Vreugdenhil et al. (2018)) showed similar saturation of the radar backscatter around this period in which the grains start to develop (BBCH 71) and as the LAI reaches a value of 2-3. After this, follow the late fruit development (BBCH 75) and the ripening stages (BBCH 89), at which the plants are harvested. For this region in the Netherlands, this is usually around mid-September (Khabbazan et al., 2019). During these last stages, it is difficult to distinguish between a decrease in the S1 index due to reduced VWC as reported by Vreugdenhil et al. (2018) and harvest because of the averaging over the fields. As also noted by Khabbazan et al. (2019), abrupt decreases occur in backscatter at individual parcel level between mid-September and mid-October as maize is harvested. Harvesting precipitously decreases backscatter, most prominently in VH, and increases the standard deviation of the VV, VH and S1 index. With the soil left bare again, the soil moisture starts to influence the backscattered signal again. Making it more difficult to detect harvest in wet autumn months. However, it is visible from the S1 index time series in Figure 4.2 that the harvest occurs between mid-September and mid-October, as the standard deviation of the signal starts to increase of both the S1 index as well as the NDVI.

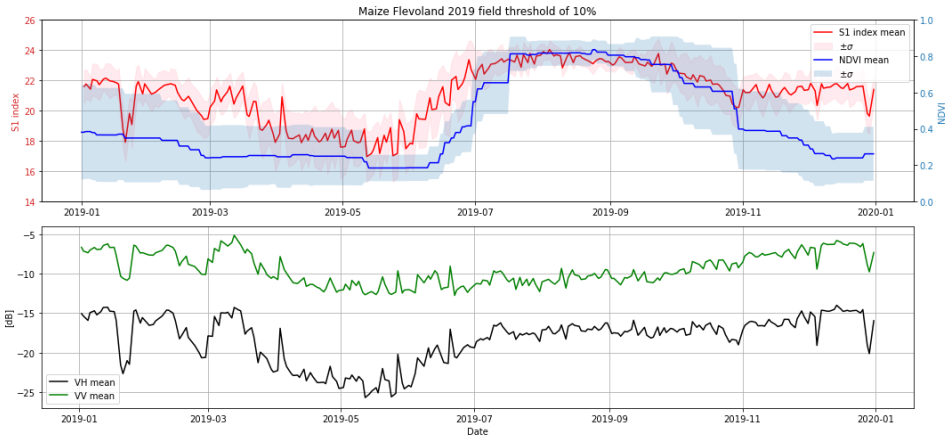

Figure 4.2: Time series of Sentinel-1 backscatter (VV, VH and S1 index) and the NDVI signal of all maize parcels in Flevoland. Top: S1 index, NDVI and their respective standard deviations. Bottom: vertical (VV) and cross (VH) polarized signal.

Barley

The temporal profile of barley is presented in Figure 4.3. Again, the backscatter is essentially determined by the soil before emergence. At the beginning of April, there was a slight decrease in direct (VV) and an increase in volume (VH) scattering, which also caused an increase in the S1 index. This is probably caused by the emergence of vegetation, as was also observed by Vreugdenhil et al. (2018) and C. Liu et al. (2013).

Then, from mid- to end-May, the S1 index starts to decrease slightly, which agrees with the findings of Chakhar et al. (2021), who observed this during the stem elongation stages (BBCH 30-39). Recall that Veloso et al. (2017) and Vreugdenhil et al. (2018) also reported attenuation of the signals due to stem elongation. This effect is visible in both polarisations and enlarged in the S1 index. Analogous to the results of Skriver et al. (1999) and Larranaga et al. (2013), the VH, VV and S1 index start to increase again after the stem elongation stages around the start of June. They found that the heading stages of the barley caused this. From mid-July to the end of August, the VH and S1 index slope becomes negative again. This period coincides with the expected harvest, as discussed in Table 3.1. Interesting to see is the two peaks in this period, one on the 30th of July and the other on the 10th of August. Comparing this to the weather data, the former coincides with heavy precipitation and the latter with a day with very strong wind gusts and heavy precipitation.

Just before the decrease in the S1 index, the NDVI decreases rapidly. Veloso et al. (2017) observed a similar decrease before the harvest for wheat due to their colour transformation from green to yellow. Since NDVI is sensitive to the plant's greenness (chlorophyll), the signal no longer detects the yellow biomass.

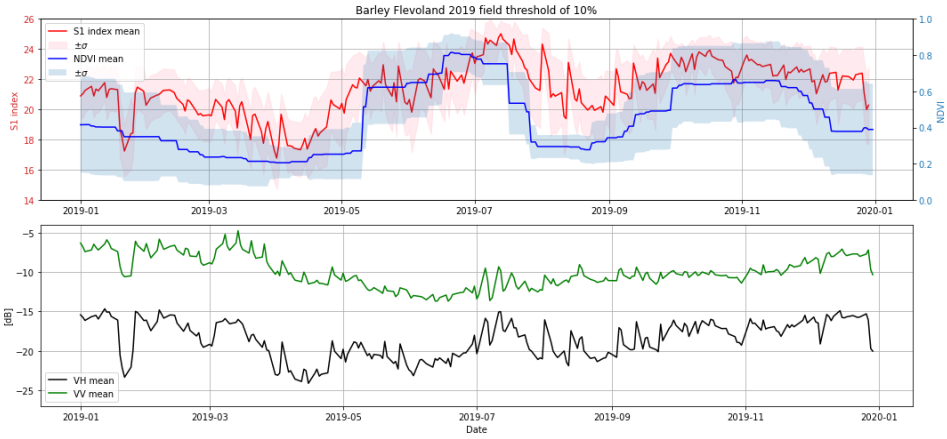

Figure 4.3: Time series of Sentinel-1 backscatter (VV, VH and S1 index) and the NDVI signal of all barley parcels in Flevoland. Top: S1 index, NDVI and their respective standard deviations. Bottom: vertical (VV) and cross (VH) polarized signal.

The increase in the S1 index from September onwards could be caused by the cover crops planted after the harvest. Since this time series represents the mean of all fields, no clear harvest event can be designated. Looking at the individual field level, this is a clear event in both the S1 index time series and the NDVI series (provided that there is no gap in the data due to clouds).

Oat

As discussed in Section 2.3, oat has a very similar growing season to barley. The S1 index and VH start to increase, while there is a slight decrease in VV again around the start of April. When comparing the time series, however, it can be seen that the local maximum is reached only in mid-June, a month later than for barley.

A similar difference in slope was observed by Shang et al. (2020). After reaching this local maximum around the same level of barley (22 dB), there is a decrease in VH while VV slightly increases. This causes a similar local minimum as was seen in barley a month earlier. This period of decrease is again expected to correspond to the stem elongation stages. Around the first of July appears to be the start of the next stage, presumably caused by the heading stages again. Note that the maximum of ca. 23 dB it reaches around the first of August is significantly lower than this maximum for barley of ca. 25 dB. This was also observed by Lopez-Sanchez et al. (2013), who found that oat has a lower sensitivity from the radar response. Finally, the S1 index reaches a minimum again at the end of August, when all plants are expected to be harvested.

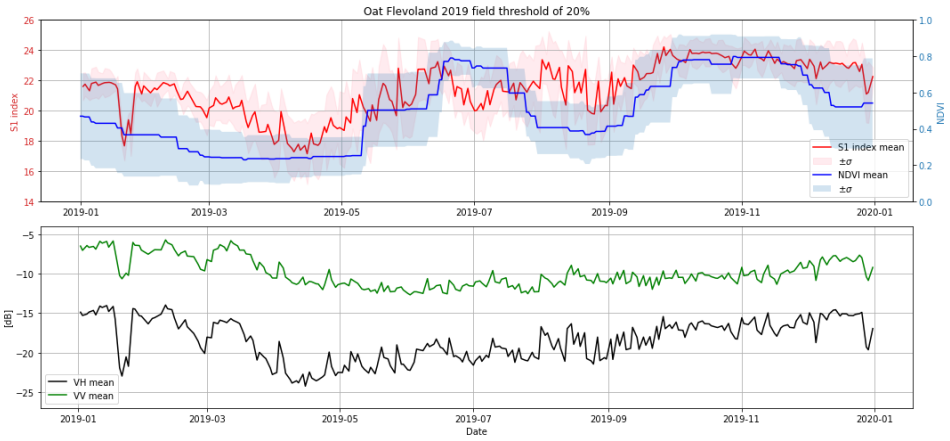

Figure 4.4: Time series of Sentinel-1 backscatter (VV, VH and S1 index) and the NDVI signal of all oat parcels in Flevoland. Top: S1 index, NDVI and their respective standard deviations. Bottom: vertical (VV) and cross (VH) polarized signal.

Wheat

Finally, wheat has a similar temporal profile to barley and oat. The same phenological stages can be estimated when comparing the time series to those of barley and oat. At the beginning of April, the plants are expected to emerge; then, in mid-May, the VV starts to decrease slightly, resulting in a plateau of the S1 index. This period is expected to correspond to the stem elongation phase, which is less pronounced in the average signal than for barley and oat. Comparing this to the CR profile of wheat from Veloso et al. (2017), a similar decrease is expected. The effect could be lost due to the temporal Lee-sigma filter applied to the S1 index. The period in which the stem elongation takes place could be too short to show a small negative slope.

Around the first of July, the S1 index slope becomes positive again due to an increasing VH and a slowly decreasing VV, which are expected to correspond to the heading stages (BBCH 50-59). Like barley, it reaches its maximum at the start of July and starts to decrease after harvest or senescence. Like the other cereals, due to the early harvest, there seems to be another growth cycle of a (cash) crop after September. Interestingly, the standard deviation of this period seems to be much larger in NDVI, which could be caused by the different crop types planted after wheat.

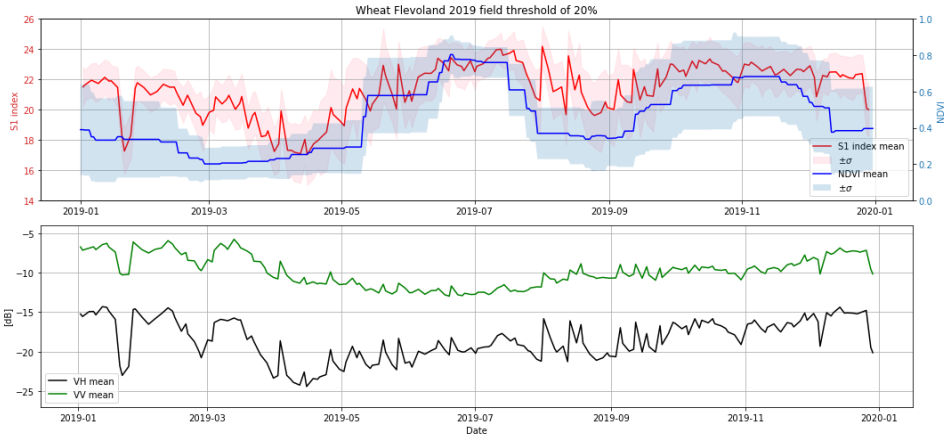

Figure 4.5: Time series of Sentinel-1 backscatter (VV, VH and S1 index) and the NDVI signal of all wheat parcels in Flevoland. Top: S1 index, NDVI and their respective standard deviations. Bottom: vertical (VV) and cross (VH) polarized signal.

4.1.2. Spatial behaviour

As described in Section 3.2.2, single fields needed to be selected to visualise the spatial behaviour. The selected fields are shown in Appendix E, with the root mean square (RMS) differences between the crop mean and the field. For each crop, the time series of the single field is shown with the corresponding rasters for the chosen date in their corresponding subsections. In each time series, four dates are labelled corresponding to the estimated phenological stages from the previous section. Recall that the dates were chosen to coincide

with NDVI observations, therefore singling out (most) external parameters influencing the signals. This way, the different signals can be compared based on their inherent differences.

A more elaborate discussion will follow on the first (maize) rasters. After that, to avoid redundancy, only relevant features not present in the maize rasters are discussed.

Maize

The four selected dates of maize are shown in Figure 4.6 and their corresponding spatial rasters are presented in Figure 4.7. The first date (label 1) corresponds to June 17, which is most likely in the leaf development phase (BBCH 10-19), since both the NDVI and S1 index have started to increase. Label 2 is placed on July 2, presumably corresponding to the start of the stem elongation phase. In 2017, during the field campaign of Khabbazan et al. (2019), the five fields of which phenological stages were recorded all had a BBCH stage 39, the last stage of the stem elongation, on July 3. On July 31, label 3 is placed to represent the start of the fruit development stage (BBCH 71-75), which is a saturated period of both the NDVI and the S1 index. Finally, label 4 on August 31 represents the approximated ripening stage (BBCH 83-89). These approximated growing stages again corresponded to the field campaign of Khabbazan et al. (2019).

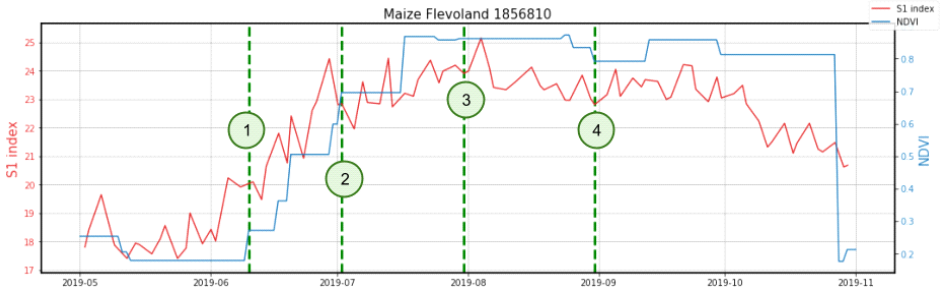

Figure 4.6: Time series of selected maize field for the S1 index and NDVI. The green dashed lines correspond to the dates which are visualised spatially: (1) 17/6, (2) 2/7, (3) 31/7, (4) 31/8.

Figure 4.7 shows the rasters corresponding to the dates 1 to 4. The S1 index, NDVI, VH, VV, and CR is visualised for each date. Analysing the rasters at separate dates, the differences between the signals are immediately clear. Firstly, there are patterns in the S1 index that are not visible in the NDVI nor directly visible in the VH, VV and CR rasters. These patterns could either be caused by the intrinsic sensor properties or by the physical properties of the target. These physical properties may vary between the terrain parameters discussed in Section 2.2.3. Noteworthy is that there are also patterns in the NDVI rasters which do not show in the S1 index rasters, e.g. the area in the lower right corner of the field on day (2). The pattern could be caused by an area lagging with fewer or smaller leaves, therefore having lower chlorophyll contents. Possible reasons that this is not visible in the radar image are that a) the VWC is the same despite the lower LAI, or b) the differences in structure are more dominant in the signal.

In the NDVI images, a border effect is also present, which is not visible in the other signals. This could be caused due to the field delineation of the BRP data set. Secondly, looking at the VH, VV and CR, it is evident that these rasters are dominated by speckle. Even though the S1 index is the filtered CR, patterns visible in the S1 index are barely recognisable in the CR raster. This difference is also visible when comparing the histograms of the CR and the S1 index. On day 1, for instance, the coefficient of variation (CV) of the CR is more than fourteen times as large as that of the S1 index, indicating a very large, evenly distributed spread in values (which is not expected of an agricultural field). This difference emphasises the importance of filtering the radar signal for interpretation. Lastly, the histograms (and rasters) demonstrate one of the disadvantages of the NDVI, namely the saturation. For days 3 and 4, the field is completely homogeneous except for the edges. This is not the case for the S1 index (or the other radar indices), which still shows spatial variability for these dates. Note that the histogram values of the NDVI observations are biased because of the edge effects and will, therefore, not be compared with the other signals.

Then, the rasters could be compared between dates. Note, however, that the colour bar and histogram ranges are not set. This was purposely done to visualise the spatial patterns at every part of the growing season. When comparing the S1 index rasters, a few things are noteworthy. Firstly, because the values do not

have defined peaks in the histogram, such as NDVI, the spatial information varies quite strongly, even though the histogram values are similar. This highlights the necessity of spatial information to understand crop development at field level. Secondly, these strong in-field variations also demonstrate the drawback of the S1 index signal since, without validation data, interpretation cannot be done with certainty.

Next, the NDVI signals can be compared. As discussed in Section 2.1, the interpretation of the NDVI is much simpler. However, the disadvantages of poor temporal resolution and saturation are obvious from Figure 4.6 and Figure 4.7 respectively. Due to the combination of these two factors, only a small time window and thus few observations are useful for crop monitoring. Finally, the other radar indices can be compared. As discussed, interpretation of this raw spatial data is difficult. However, as expected from the theory (Equation (2.3)), it seems that the noise is higher when the backscatter is weaker. For instance, when comparing day 1 CR with the S1 index, the pattern of the S1 index is not recognisable. However, on day 4, the dark area in the middle is (vaguely) recognisable, as well as the light area in the lower right corner of the field.

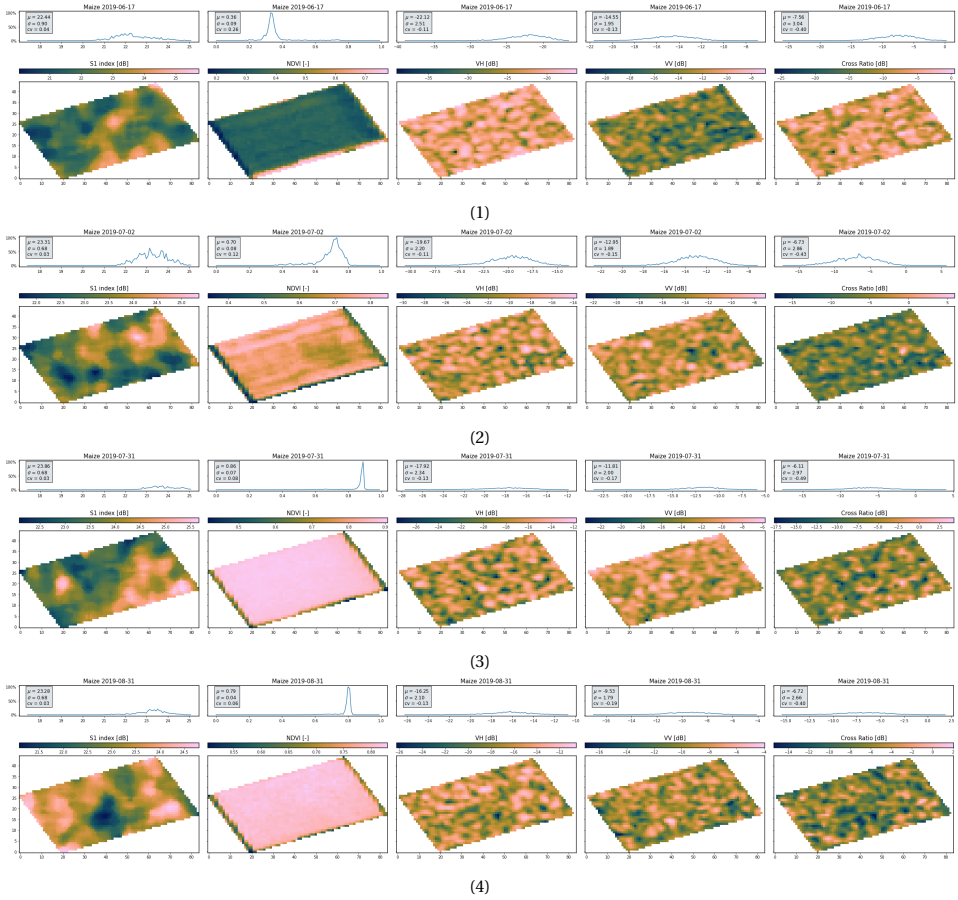

Figure 4.7: Spatial signals of the S1 index, NDVI, VH, VV and Cross Ratio of maize, where the subfigure caption corresponds to the labelled dates from Figure 4.6.

Barley

The time series of the selected barley field is presented in Figure 4.8, where the labels 1 to 4 correspond to April 18, May 13, June 17 and June 30, respectively. The expected corresponding phenological stages are 1) leaf development (BBCH 10-19), 2) stem elongation (BBCH 30-39), 3) heading (BBCH 50-59) and 4) the fruit development or ripening stage (BBCH 70-89).
As discussed in Section 4.1.1, the harvest is distinguishable at field level (around July 20). Interestingly, the NDVI has decreased earlier than the S1 index. This could be due to the transformation from green to yellow during the ripening stage. Because the previous observation was at the end of June, it might appear that this happened overnight, but there is a two-week difference between the observations.

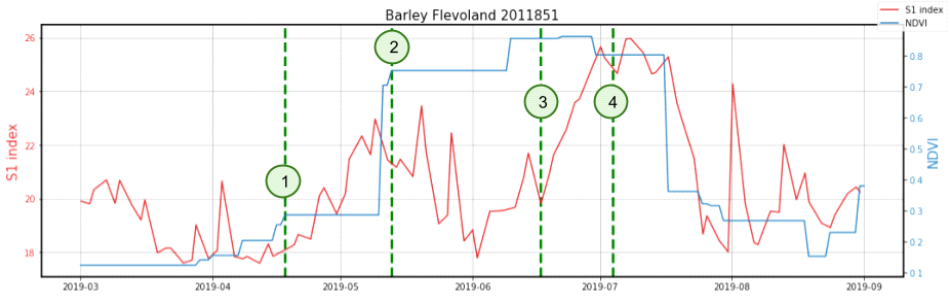

Figure 4.8: Time series of selected barley field for the S1 index and NDVI. The green dashed lines correspond to the dates which are visualised spatially: (1) 18/4, (2) 13/5, (3) 17/6, (4) 30/6.

Comparing Figure 4.9 to Figure 4.7, a similar spatial behaviour can be seen. Again, the S1 index shows very different patterns than the NDVI, and the NDVI signal demonstrates saturation and strong edge effects. Note that the NDVI raster on day 3 does not represent the whole field because no full-coverage NDVI image was available in this period.

Moreover, it should be noted that subtle differences in single polarisations, such as an increase in VV due to the tipping of the heads, were not captured by the time series since only the S1 index and NDVI were plotted. From the spatial data alone, such observations do not seem visible.

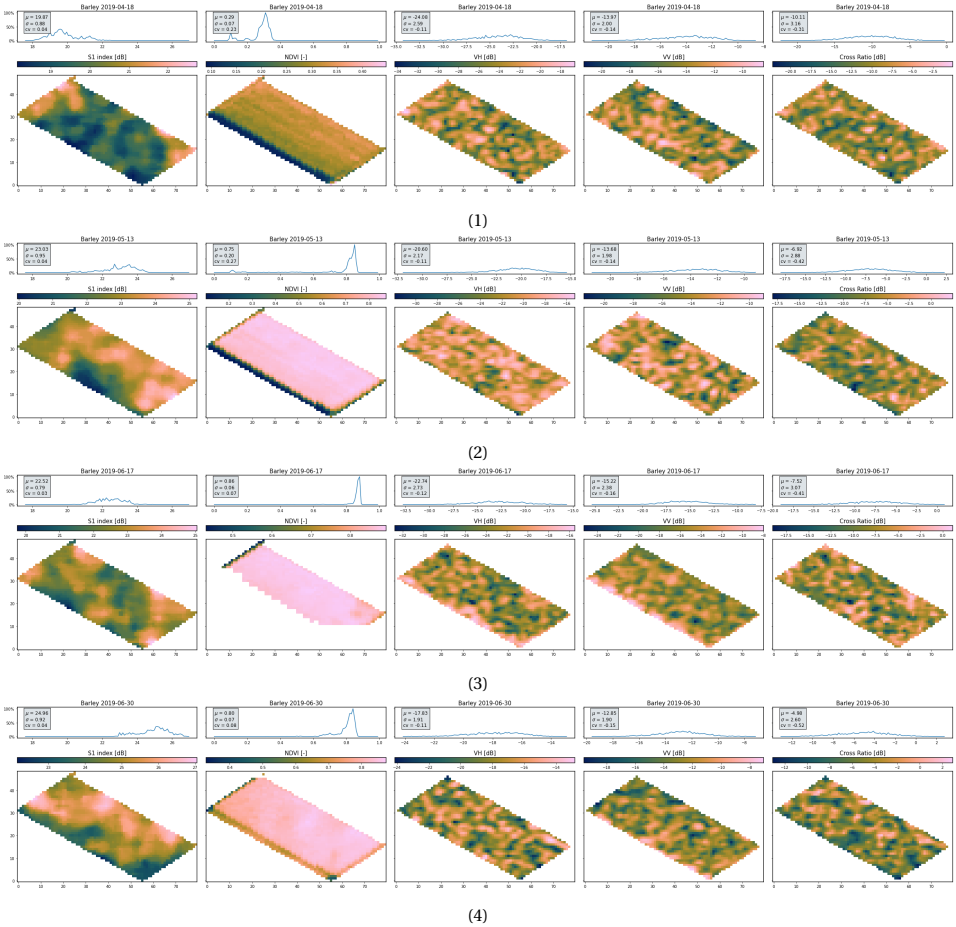

Figure 4.9: Spatial signals of the S1 index, NDVI, VH, VV and Cross Ratio of barley, where the subfigure caption corresponds to the labelled dates from Figure 4.8.

Oat

Figure 4.10 presents the time series of the selected oat field. The labelled dates are 1) April 18, 2) May 13, 3) June 25, and 4) July 30. Because of the limited availability of NDVI observations, the selected dates coincide

with slightly different phenological stages. The approximated stages are 1) germination/leaf development (BBCH ~5-11), 2) leaf development/tillering (BBCH 12-29), 3) stem elongation (BBCH 30-39), 4) fruit development/ripening (BBCH 75-85). Interesting to see is the high NDVI value during the stem elongation (day 3) and the low NDVI value during the latest growing stages. The fact that the signals show opposite behaviour (while reflecting the same field) confirms the complementary character of the SAR data.

As with barley, one can clearly distinguish the harvest date at parcel-level. Right before the harvest, a slight decrease in S1 index can be observed. This is most likely due to the decrease in VWC, as expected from the BBCH phenological stages (BBA et al., 2001) and is analogous to the findings of Vreugdenhil et al. (2018).

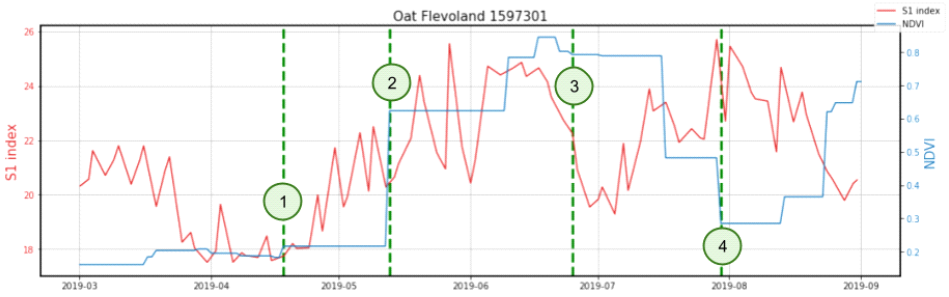

Figure 4.10: Time series of selected oat field for the S1 index and NDVI. The green dashed lines correspond to the dates which are visualised spatially: (1) 18/4, (2) 13/5, (3) 25/6, (4) 30/7.

Some interesting features can be observed in Figure 4.11, which were not visible for maize or barley. On the first day, a completely homogeneous NDVI raster can be seen (except for the recurring edge effects). On this day, the average S1 index value is also still low. Despite the same observation date, the raster is relatively homogeneous compared to the S1 index on the first day of barley (Figure 4.91). The areas with similar backscatter values, i.e. *clusters*, are much larger for the oat raster, while the mean value only differs by 1.16 dB. A possible explanation could be that the barley just emerged and unfolded the first leaves (BBCH 11), creating a heterogeneous field. If oat had not yet emerged, the observed pattern is caused by variations in soil moisture, which is expected to be more homogeneous. In addition, a lower, more homogeneous backscatter pattern corresponds to the findings of Veloso et al. (2017), who observed the smoothing of the soil before emergence.

If one would only look at the NDVI rasters of day 1 and day 4, it would seem the vegetation in the field would be similar. However, comparing the S1 index rasters on the respective dates shows large differences in (presumably) vegetation. (Note once more that this cannot be stated with absolute certainty due to the lack of validation data. However, comparing the temporal profile to the literature and with the knowledge of the average harvest dates, it would be quite safe to assume the pattern caused by the vegetation.) According to the BBCH scale, the oat plants turn yellow in the ripening stage (Earth Observation Research Branch Team, 2011). This would explain the homogeneous NDVI raster and the heterogeneous S1 index raster.

On day 2 and 3, a star-shaped pattern is visible on the right side of the NDVI rasters, which is not visible in the S1 index rasters nor the other radar rasters. On days 2 and 3, the S1 index rasters show clear clusters in the middle and lower left corners, respectively. Based on the estimated phenological stages, one could assume structure differences cause these due to varying numbers of leaves and tillers on day 2, and a varying number of nodes on day 3.

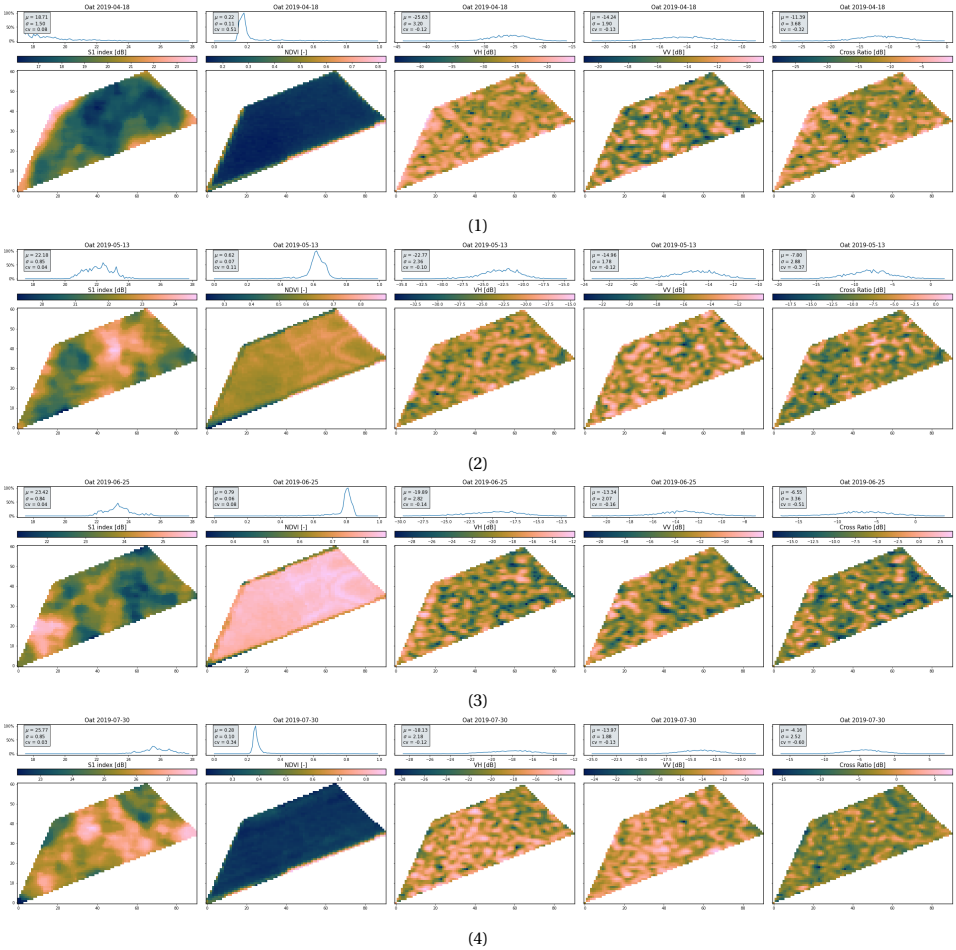

Figure 4.11: Spatial signals of the S1 index, NDVI, VH, VV and Cross Ratio of oat, where the subfigure caption corresponds to the labelled dates from Figure 4.10.

Wheat

Finally, the time series of wheat is presented in Figure 4.12. The observation dates are 1) April 18, 2) May 11, 3) July 2, and 4) August 10. Again assumed to represent the leaf development (BBCH 10-19), stem elongation (BBCH 30-39), heading (BBCH 50-59), and senescence (BBCH 97).

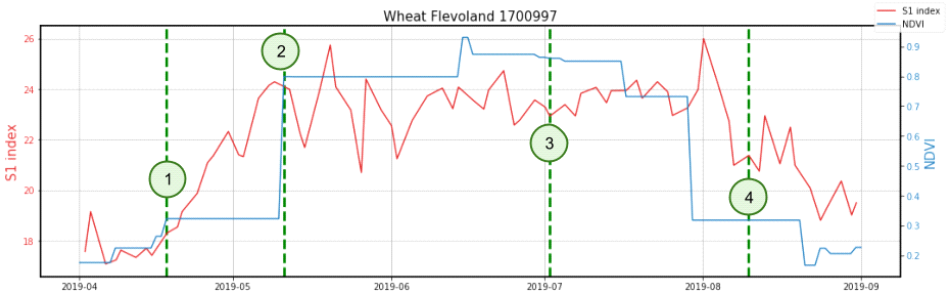

Figure 4.12: Time series of the selected wheat field for the S1 index and NDVI. The green dashed lines correspond to the dates which are visualised spatially: (1) 18/4, (2) 11/5, (3) 2/7, (4) 10/8

The wheat rasters in Figure 4.13 appear very similar to those of oat. The first and last NDVI observations show little variability (except near the edges), and the observations on the second and third days are saturated. The S1 index rasters on the first and fourth day are similar to the NDVI rasters: while the NDVI rasters appear similar, the backscatter response on the fourth day is much stronger than on the first day.

It is remarkable that in the NDVI rasters, an L-shaped feature is present with much lower NDVI values.

This could be a structure such as a greenhouse in the field. The VH, VV and CR rasters show how the algorithm filters such persistent structures. The feature is, however, not visible in the S1 index due to spatial filtering. Therefore, areas with such areas that are masked in the BP algorithm are visible in the BP rasters if the spatial contribution of the NDVI is dominant.

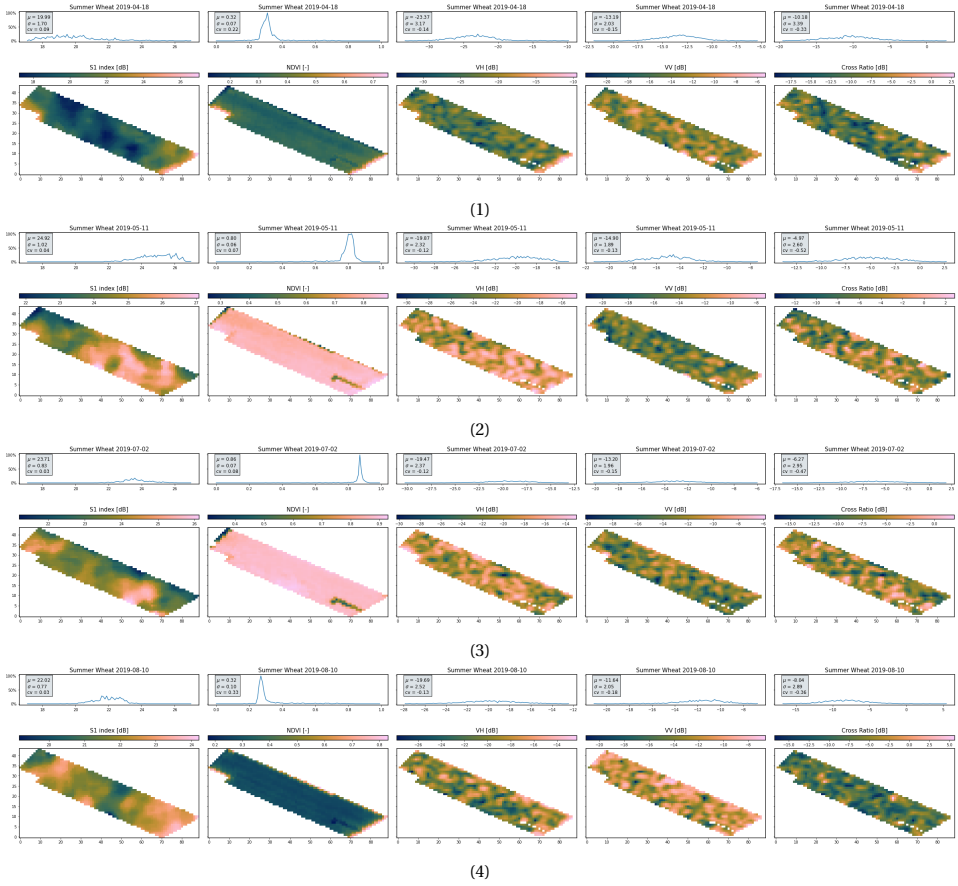

Figure 4.13: Spatial signals of the S1 index, NDVI, VH, VV and Cross Ratio of wheat, where the subfigure caption corresponds to the labelled dates from Figure 4.12.

4.1.3. Conclusions on temporal and spatial behaviour

The temporal signal correspond well with the temporal profiles described in the literature for all crops. Extracting the principal phenological stages from the time series seems possible but would need to be verified using field data. Moreover, the time series demonstrate the differences between maize and the cereals in the SAR and NDVI signals.

The spatial information of the VH, VV and CR did not contain clear spatial patterns due to the presence of speckle, and could, therefore, not be interpreted visually. The comparison between the NDVI and S1 index observations on the same dates demonstrated the inherent differences between the signals. The NDVI spatial data was homogeneous for significant periods of the growing season, and the spatial S1 index data demonstrated the difficulty of distinguishing between the different causes of the spatial features in the SAR data. Therefore, from the spatial data alone, phenological stages or biomass cannot be estimated but must be complimented with the time series.

4.2. Cluster detection with spatial metrics

Because this step is based on image-processing, crop differences were deemed irrelevant when the rasters showed similar cluster shapes and sizes. Therefore, a selection was made to minimise the redundant information. In the following sections, the maize field is visualized as an example. The plots of the other crops can be found in Appendix F.

4.2.1. Metric analysis

As set out in the methodology (Section 3.3.2), the three selected metrics (Altieri entropy, cluster tendency and cluster prominence) were analysed for three scenarios. First, the behaviour of the metrics during sudden changes in the S1 index is analysed temporally and spatially. Second, the S1 index rasters are compared for periods when metrics are similar. Third, the rasters were compared for dissimilar metric behaviour. This way, a better understanding was obtained of what the metrics describe and which metric would be the most suitable in which situation.

The same sections and plots can be found in Appendix F for the barley, oat and wheat. Additionally, Appendix F contains a comparison of the computation times for the different metrics.

S1 index change effects

The two dashed, black lines mark a period of a sudden change in the S1 index in Figure 4.14. Between October 3 and 11, the average S1 index (red line) decreased from 23.4 dB to 21.4 dB. During this period, the Altieri entropy, the cluster tendency and cluster prominence remained almost constant, only showing a small decrease and increase from the observations of October 9 and 11, respectively.

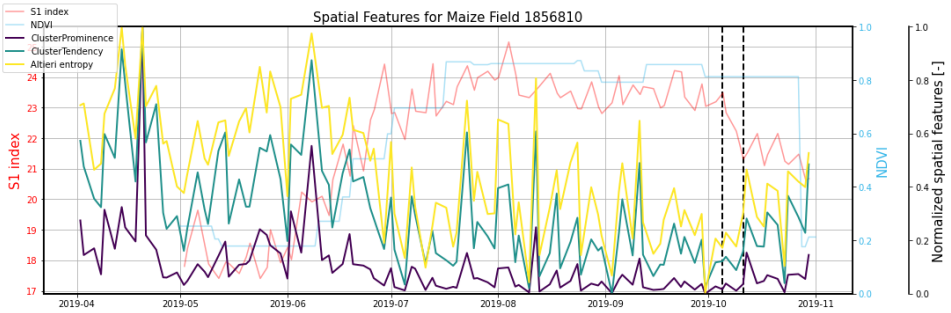

Figure 4.14: Effect of a sudden change in S1 index on spatial metrics of a maize field in time, where the dashed vertical lines denote the start and end of the period of interest.

There are no clear changes in the spatial pattern analysing the S1 index rasters in this period. This is confirmed by the histogram, which has a similar shape every day but is shifted to a lower mean value. Results for the other crops were very similar in the sense that the changes in the S1 index could not be identified by only looking at the spatial pattern (see Appendix F).

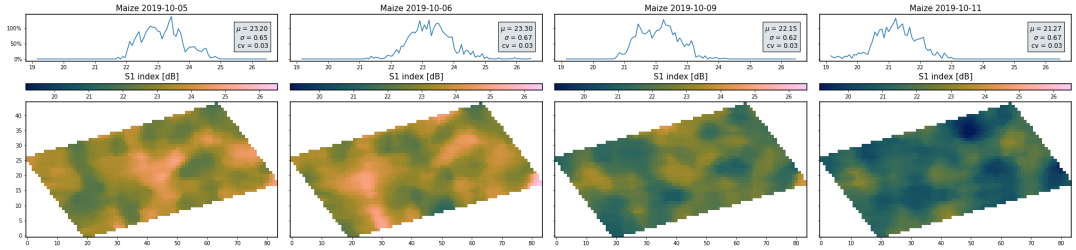

Figure 4.15: Maize S1 index rasters during a period of great S1 index changes.

This is an interesting result since this implies that no distinction based on spatial pattern can be made between a fully grown field and a harvested field. The spatial metrics confirm the lack of change in spatial pattern between the rasters, which could be expected since the rasters demonstrate a similar amount of clustering. However, it cannot be said with certainty that the harvest occurred in this period. This assumption

was made based on the expected harvest time from literature and the S1 index values but would have to be verified by a field with a known harvest date.

Comparing these results to those of barley, oat and wheat (Appendix F.1), changes in spatial metrics appear not to be proportional to large changes in the S1 index. Therefore, the metrics do not seem suitable for detecting harvest or other changes that are applied to the field simultaneously.

Metric similarities

Periods with similar and dissimilar behaviour are analysed to understand the spatial metrics better. Since the cluster prominence is a modification of the cluster tendency where one of the terms in the sum is squared (see Equation (3.1) and Equation (3.2)), the high and low values are amplified. Therefore, the distribution of the normalised values is different, and only at the highest or lowest values do the cluster tendency and cluster prominence have the same values. The normalized Altieri entropy also has a higher mean value than the cluster prominence, so the metric values do not match except for the highest and lowest values. A period was chosen to compare similar metric behaviour where the three metrics follow the same pattern but with different biases, and is presented in Figure 4.16.

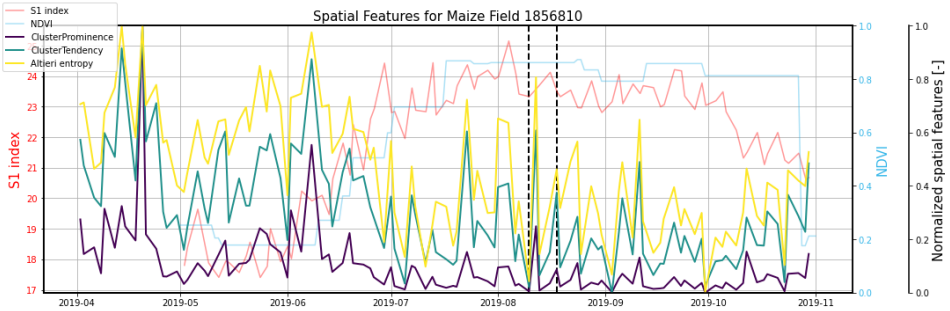

Figure 4.16: Time series of spatial metrics of the selected maize field, where the dashed vertical lines denote the start and end of a period with similar metric behaviour.

Since the metrics were selected based on their ability to describe large clusters, it was expected that the increase and decrease of the values would coincide with larger and smaller clusters. This corresponds well to the values in the time series and the rasters in Figure 4.17, where the second, fourth and fifth rasters have more clearly defined clusters than the first and third raster.

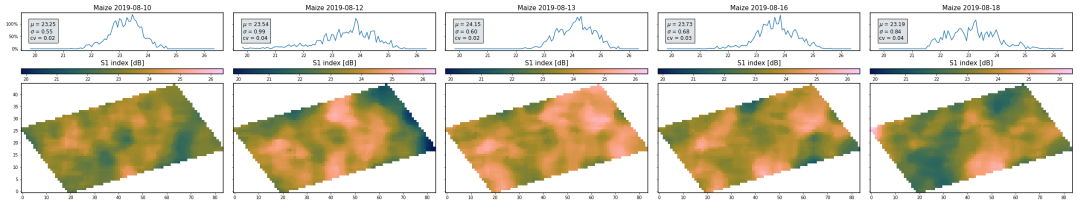

Figure 4.17: Maize S1 index rasters during a period of similar metric behaviour.

When comparing the second and fourth raster, however, it is not immediately clear what causes the large difference in all three metrics. Both rasters appear to have four clusters of approximately the same size, with areas between the clusters with slightly lower values. To better understand what causes the discrepancy in the average values, the GLCM features were computed again at voxel-level, such that two-dimensional feature maps of the metrics could be made. The results of the cluster tendency and cluster prominence feature maps can be seen in Figure 4.18a and Figure 4.18b respectively. The feature maps demonstrate the cause of the discrepancy and immediately highlight both metrics' limitations.

Firstly, cluster tendency is a measure of the grouping of pixels for similar grey-level values. These grey-level values do not necessarily correspond to very high or low backscatter values, i.e. dominant clusters. In the case of Figure 4.18a, on August 12 (left figure), it shows that areas in between clusters seem to have similar values, and at the right edge, there is a group of lower values. On August 16, Figure 4.17 shows a large cluster on the right side, which is not recognised by the cluster tendency in Figure 4.18a. This could be caused by small differences within the cluster that fall into separate bins and are therefore not detected as a co-occurrence.

Secondly, the feature maps of the cluster prominence are compared in Figure 4.18b, where the differences are less clear. This could be expected since the difference between the two dates in the normalized time series was also smaller (0.21 vs 0.46). Recall that a higher value implies more asymmetry around the mean of the GLCM, while a lower value indicates a peak near the mean value and less variation about the mean. This agrees with the histograms from Figure 4.17, where the histogram of the second raster has a larger standard deviation (0.99 vs 0.68) and shows the highest peak around 23.85 dB, which is 0.31 dB higher than its mean. This unevenness in the histogram directly translates into the GLCM since there is a higher probability of certain co-occurrences when the possible values are not uniformly distributed over the bins. The feature maps of the cluster prominence in Figure 4.18b show the outlines of the prominent clusters. For August 12, the outlines of the three main clusters in the upper half of the raster can be seen, but it appears that the contrast needs to be higher for the clusters in the lower half. This immediately illustrates the difference with cluster tendency, for which these values were similar and assigned high values. For the raster on August 16, a few pixels have a much higher value than the rest of the raster. These pixels correspond to the edge between the small cluster of low values and the larger, high-valued cluster. Since this raster of the fourth observation has fewer areas with strong contrast, the cluster prominence has a lower mean value.

Note that this could be a limitation of the cluster prominence: if there are many very small clusters with high contrast, cluster prominence would be high even though the raster would not meet the set requirements of large clusters. However, due to the filtering of the S1 index, these small clusters are often smoothed enough not to induce high values. Moreover, a limitation of the cluster prominence is that it does not fully capture large clusters in the corners of the rasters.

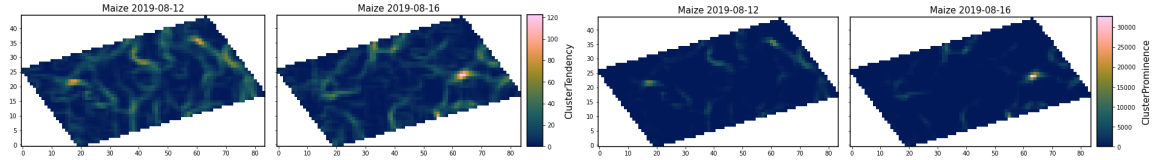

(a) (b)

Figure 4.18: Comparison of the feature maps of (a) the cluster tendency and (b) the cluster prominence for the S1 index rasters of the selected maize field on August 12 and August 16.

No feature maps were created for the Altieri entropy, but the spatial configuration can be assessed in terms of residual entropy and MI. Recall that the residual entropy represents the information on one variable when the other variables are removed. At the same time, the MI is used to identify the strength of the overall role of space. Substituting the overall entropy and the MI in Equation (2.12), it shows that the percentage of entropy due to the spatial configuration is 3.0% and 0.1% for the rasters on August 12 and 16, respectively, explaining why the values agree with the other spatial metrics. The residual entropy is responsible for the largest part of the overall entropy and is dependent on the uniformity of the data. This higher uniformity can be seen in the histograms of Figure 4.17, where the raster of August 12 has a lower peak and a larger standard deviation.

Metric differences

A period is demarcated for dissimilar metric behaviour in the time series of Figure 4.19. During the four observations in this period, the second and third observations show divergent metric values: the second raster from May 20 has an increased Altieri entropy, decreased cluster tendency and constant cluster prominence with respect to the first observation. The third raster from May 21 displays a decrease in Altieri entropy, a constant cluster tendency value, and a slight increase in cluster prominence with respect to the second raster. Finally, all three metrics increase for the fourth observation.

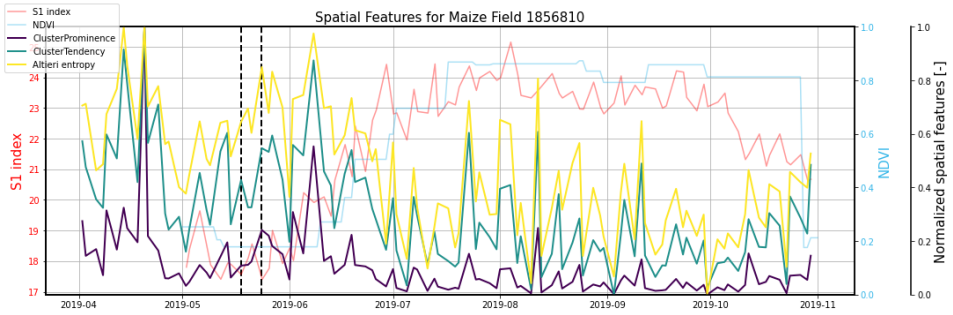

Figure 4.19: Time series of spatial metrics of the selected maize field, where the dashed vertical lines denote the start and end of a period with dissimilar metric behaviour.

An increase in Altieri entropy is observed for the second raster. Comparing the entropy's elements to the first raster, a similar residual entropy (7.11 vs 7.10) is observed. However, the spatial mutual information more than doubles from 0.06 to 0.15. The main driver of this change is hard to discriminate by eye but could be further evaluated using the partial entropy terms of the Altieri entropy to explain the spatial contribution for each distance interval. Complete interpretation of the results falls outside of the scope of this thesis.

The Altieri entropy has decreased for the third raster due to a slightly lower residual entropy and MI. The reduced residual entropy could be due to the marginally smaller variability ($CV = 0.04$ vs 0.05). The MI might have decreased due to the similar values around the edges. Since co-occurrence distances are defined with Euclidean distances, the measure is more sensitive to spherical shapes than the elongated clusters around the edges. However, the differences are small (0.15 vs 0.11), and further analysis is required to state this with certainty.

A decrease in cluster tendency is observed between the first and second raster. This seems logical comparing the rasters in Figure 4.20: the first raster shows more and larger clusters of similar values. This was verified by the feature maps for the two rasters, which showed little to no cluster tendency in the middle part of the second raster. Thereby causing a lower overall value.

Finally, a constant cluster prominence is observed between the two observations. This is presumably due to the similar distribution of values, as can be seen in the histograms of Figure 4.20. Computing the cluster prominence spatially shows the higher values around the edges of both rasters, where the clusters are defined the most clearly.

The cluster tendency and prominence stay almost constant between the second and third rasters due to the similar pattern and contrast between the rasters. The histograms confirm this, showing a similar but shifted distribution towards higher backscatter values. The fourth raster shows larger, spherical clusters, which shows in all three spatial metrics by an increase.

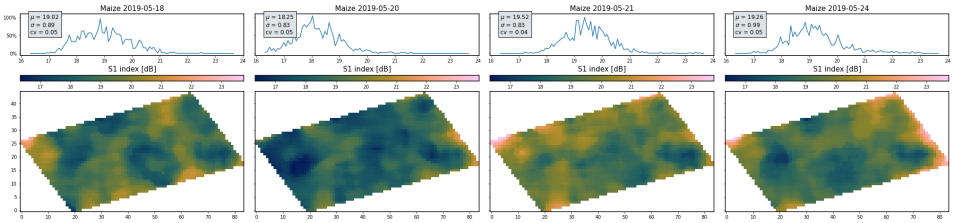

Figure 4.20: Maize S1 index rasters during period of dissimilar metric behaviour.

The differences between the metrics demonstrate the sensitivity to the different spatial features in the rasters. The Altieri entropy is most sensitive to the probability of certain backscatter values and only in small parts dependent on the spatial configuration. The cluster tendency performs well when capturing the presence of clusters. However, it is also sensitive to areas between clusters with similar backscatter values, i.e. it has few 'false negatives'. Cluster prominence, on the other hand, is much less sensitive and only detects prominent clusters, i.e. cluster prominence has few false positives.

Because all three metrics are based on co-occurrences, results depend on the selected bin size. Adjusting

this parameter could emphasize or diminish certain spatial features, resulting in other spatial metric values. However, a deeper analysis falls outside this thesis's scope.

Limitations of analysis

The previous scenarios have proven useful in exploring the capabilities of the three selected metrics and providing an initial assessment of their potential. Nevertheless, there are several limitations to this approach. First, the metrics selection is based on comparing the minima and maxima of varying GLCM and entropy features for one field per crop type. Although the theoretical description of the features supported this decision, the sample size was small. Besides the GLCM features, the `PyRadiomics` package provides many more spatial metrics, either based on shape or variations of the GLCM. A full comparison falls outside the scope of this thesis but could assess the potential of the other metrics.

Furthermore, the analysed scenarios only represent a small subset of possible scenarios. Other periods that would be interesting to analyse include right before leaf emergence, right after harvest, and during a long period of saturation. Ideally, field data would be collected such that the analysis could be turned around: if a certain event happens in the field, how do the different metrics capture this event? Is this response the same for all crops and all parts of the growing season? By answering these questions, metric behaviour could be matched with physical events.

Lastly, since rasters are selected based on certain metric values, the method is subjective to a confirmation bias, i.e. the rasters are selected with the knowledge of the expected behaviour in mind. For instance, if the Altieri entropy is high, one could explain this in light of a large number of classes, even though the actual cause could be a combination of factors.

4.2.2. Defining thresholds

Based on the field inspection per crop type of five fields, the metric thresholds were defined and can be seen in Table 4.1. A visual example of how the thresholds were selected can be found in Appendix G.

Table 4.1: Spatial metric threshold values per crop type, each value is the average of five field thresholds.

	Maize	Barley	Oat	Wheat
Altieri	6.62	6.45	6.86	6.49
Cluster tendency	250.00	303.08	437.41	329.50
Cluster prominence	225611.36	453664.53	447072.31	325152.97

Even though these values cannot be measured to a 'true' value, their variability does provide information on how clearly a threshold can be defined. For instance, if there is a clear 'tipping point' when sorting the rasters, a similar threshold will be chosen for each field, and thus the variability between the values is smaller. From Table 4.1, it can be seen that variability between thresholds is lowest for the Altieri entropy. A further discussion on this can be found in Appendix G.2.

The metric values of the rasters that were selected as limit, i.e. the first rasters that did not meet the requirements, were recorded as normalised values to reduce a possible bias when manually selecting them. This way, no value could be 'recognised' since the normalisation was done with min-max scaling, resulting in different distributions.

However, there are quite some limitations related to this method for threshold selection. First, the selection is done by eye and, therefore, fairly subjective. Despite having set certain requirements, these were not tested quantitatively. Results are, therefore, not completely reproducible, which is a severe limitation of the method. Another limitation connected to this problem of subjectivity is that threshold selection is very time-consuming. For this reason, the sample size is small, and the uncertainties are large. By automating the process, the threshold values could be determined at a larger scale. However, yet another metric would need to be implemented to evaluate the metric's clusters, which would possibly introduce other sources of uncertainty.

4.2.3. Conclusions on cluster detection with spatial metrics

The analysis has made the first steps towards understanding the spatial metrics and their potential. By comparing the three metrics in different scenarios, it highlighted the strengths and weaknesses of each of the

metrics. An overview of these strengths and weaknesses is provided in Table 4.2. The next step in the application of these metrics would be to identify when which sensitivity is required, e.g. if the detection of stem elongation clusters would require better detection of prominent clusters or of larger clusters with a constant value. However, this would require field measurements to determine the cause of the spatial data.

Table 4.2: Strengths and weaknesses of the three spatial metrics.

	Strengths	**Weaknesses**
Altieri entropy	· provides measure on heterogeneity and spatial configuration · low threshold variability · could provide further analysis of distance measures	· longer computation time · less intuitive interpretation · not able to detect S1 index changes
Cluster tendency	· sensitive to clusters · few false negatives · short computation time · intuitive interpretation	· does not account for (small) intra·cluster variability · sensitive to homogeneous areas in between clusters · not able to detect S1 index changes · very sensitive to bin size parameter
Cluster prominence	· only captures dominant clusters · few false positives · short computation time · intuitive interpretation	· low sensitivity to clusters with a gradient around the edge · does not represent large clusters in corners proportionally · high threshold variability · not able to detect S1 index changes

4.3. Pattern consistency

Once the rasters that possibly contain relevant spatial features have been identified, the consistency between sequential observations could be tested both temporally and spatially. First, the temporal consistency is discussed in Section 4.3.1 for the same maize field. Then, in Section 4.3.2, an example of the persistent spatial pattern extraction is presented.

4.3.1. Temporal consistency

Step one of the processing was to define the periods of interest. First, the temporal consistency of the example maize field is analysed at field level to understand the autocorrelation behaviour and the metrics better. Next, results are generalised for all crops and metrics.
Since these periods differ per metric, the example of the maize field is shown for each of the three metrics in the following subsections. Examples of the other crops can be found in Appendix H.

Consistency at field level

Figure 4.21 shows the time series of the Altieri entropy and the autocorrelation for the example maize field. The correlation is black, with values above the threshold value (0.5) marked red. Note that a red line between two data points corresponds to three correlated observations in a row because correlation is computed between two rasters. The blue line shows the Altieri entropy, which is marked above the threshold value (6.87) from Table 4.1.
Since the cluster prominence and cluster tendency demonstrated similar behaviour, the analysis is included in Appendix H. Additionally, it contains the time series of the other crops.

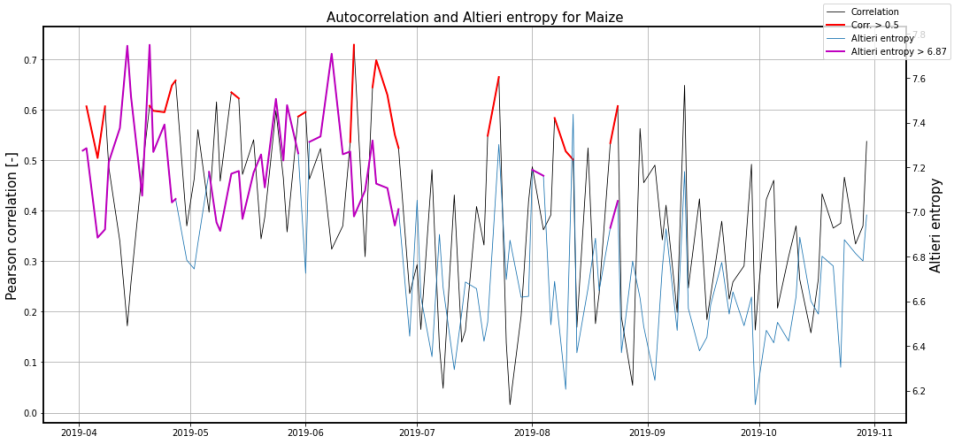

Figure 4.21: Time series of autocorrelation and Altieri entropy, where periods with two or more subsequent observations are marked for both metrics.

A few things are noteworthy in analysing this plot. First, a general trend opposite to that of the S1 index can be seen. This result was expected from the literature and the plots shown in Section 4.1.2: the surface is much less dynamic than when vegetation grows. Hence, changes in soil moisture are presumably the main driver for changes. In addition to the slower changing backscatter (and thus higher autocorrelation), the S1 index rasters from this period also showed a more homogeneous pattern with larger clusters, hence the high Altieri entropy.

Second, interesting to see is that even though both metrics have the highest values before July, they do not always agree. The spatial patterns in the radar data after July are driven by the vegetation and show a few occurrences where either the autocorrelation is high (e.g. July 19-23), the Altieri entropy is high (August 1-4), or both (August 22-24). To understand these values, one must look at the spatial data presented in Figure 4.22.

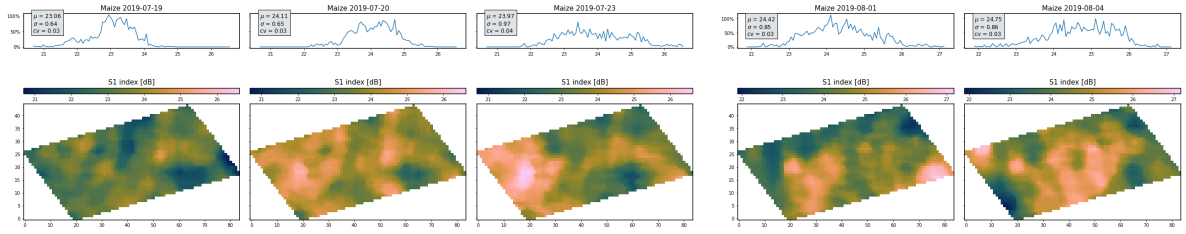

(a) (b)

Figure 4.22: Spatial S1 index data in periods of (a) high autocorrelation values and low Altieri entropy, and (b) high Altieri entropy and low autocorrelation values.

Figure 4.22a shows the S1 index series between July 19 and July 23, a period with high autocorrelation values but without Altieri entropy values above the threshold for all days. Between the rasters, a pattern is recognisable, hence the autocorrelation values. However, the first two rasters have an insufficient Altieri entropy to be deemed relevant. This is understandable for the first rasters, which do not clearly show any clusters. However, the relevance of the second rasters is disputable: some clusters are visible, but the contrast is low. The currently defined threshold would, therefore, not include this raster, but, dependent on the application, it could be of interest.

Figure 4.22b demonstrates the importance of combining the two metrics. Intuitively, if a constant spatial metric value such as Altieri entropy is (approximately) constant, the spatial data could also be constant. These two rasters show that, despite their similar entropy values (7.18 and 7.16), there is no constant spatial pattern.

Consistency at crop level

The computation was performed on all fields of all crops for the three metrics to generalise the occurrences of cluster consistency. The resulting histograms for the Altieri entropy, cluster tendency and cluster prominence can be seen in Figure 4.23, where the average S1 index time series are plotted in red. Note that the bars with low values are caused by observations from relative orbits that not cover the entire study area, hence their lower value after the normalisation using the total number of fields.

Two comparisons can be made between the figures: one between crops and one between the metrics. Firstly, crops can be compared for each metric. Figure 4.23a, Figure 4.23b, and Figure 4.23c show this for the Altieri entropy, cluster tendency and cluster prominence, respectively. It can be seen that frequency often has an inversely proportional profile of the S1 index for all crops, although this opposite relation is more pronounced for maize, barley and wheat than for oat. For maize, this corresponds to the findings for the single maize field for all metrics (Figure 4.21, Figure H.1, and Figure H.1). Compared to the other crops, maize shows the largest range in values, with a peak around the end of May of values between 0.5 and 0.65 and an almost constant minimum between the start of August to the end of September between 0 and 0.2. The peak occurs at the start of the growing season, around the time of emergence. It shows that, in this period, 50 to 65% of the fields display consistent clusters. Based on the analysis from Section 4.1.1, soil moisture plays an important role in the spatial patterns at this stage, but vegetation likely also plays a role, as it has already emerged during this period.

However, similar values of the other crops would be expected around emergence. A possible cause for this discrepancy is the difference in soil moisture in May as opposed to April, which will not influence the spatial signal of the cereals after they have already entered the leaf development stage. Another possibility is a difference in agricultural practices, i.e. how the land is worked or the crops are watered. Furthermore, the histograms of maize show a lower minimum, which stays constant over a longer period. This result can indicate 1) the highly dynamic nature of the spatial data (low autocorrelation), 2) little to no clustering, or both. Comparing this to the other crops, the minima all seem to have a higher absolute value in terms of normalised frequency and relative compared to the maximum. The single field consistency time series of maize (Figure 4.21, Figure H.1, and Figure H.1) and the other crops (Appendix H) demonstrate that autocorrelation for the cereals is higher during the later phenological stages (after leaf development). This would mean that the cereals contain more persistent clusters during this period. This might be due to the saturated S1 index in this period, in which small variations in structure or VWC are not detected and fluctuations in noise dominate the spatial signal. Another possible cause is the influence of soil moisture on the spatial signal. In

Section 4.1.1, it was discussed how precipitation events were visible in the average time series of the cereals but not in maize. If the crops hold the rainwater for a few days, the spatial pattern could be influenced by the increased soil moisture. However, this would need to be verified with field measurements.

The cereals appear to have a similar profile to some degree. During the stem elongation stages established in Section 4.1.1, the frequency decreases for all crops. Observations from the spatial analysis at this stage (Section 4.1.2) show clear spatial clustering. However, due to the dynamic nature of this period, i.e. large structure changes over a short period, the frequency of persistent patterns decreases. Next, all crops show a slight increase at the start of the heading stage. Although this is also a change in structure, the increase could be due to the less substantial change in geometry in time (less dynamic change) and in space (smaller changes could cause values to still fall in the same bins). During the final stages of the phenological cycle, when the S1 index is highest, the minima are reached. Comparing Figure 4.23c with Figure I.1 shows that the decrease in frequency is most likely due to a combination of the less defined clusters and lower spatial autocorrelation.

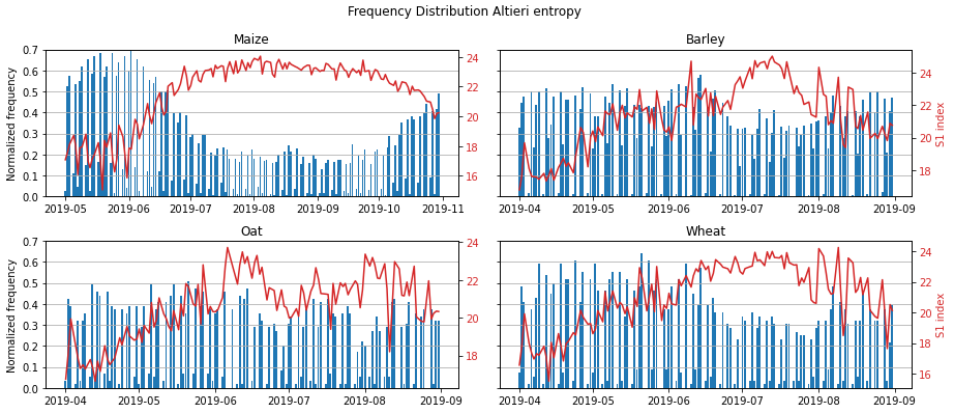

(a)

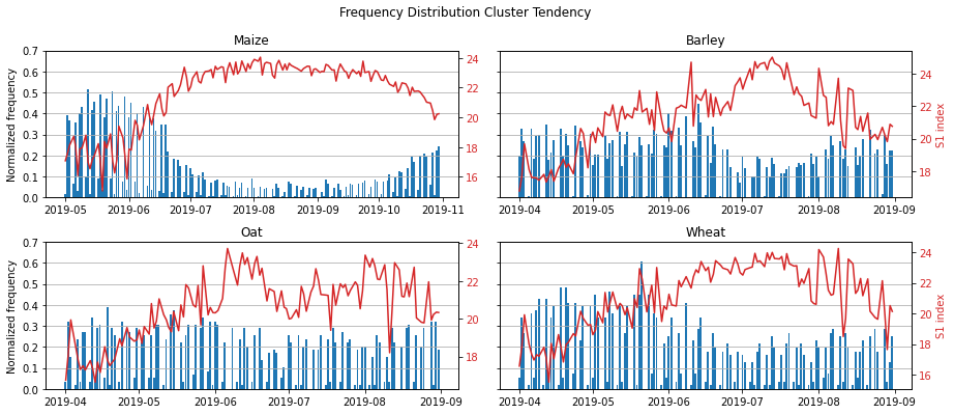

(b)

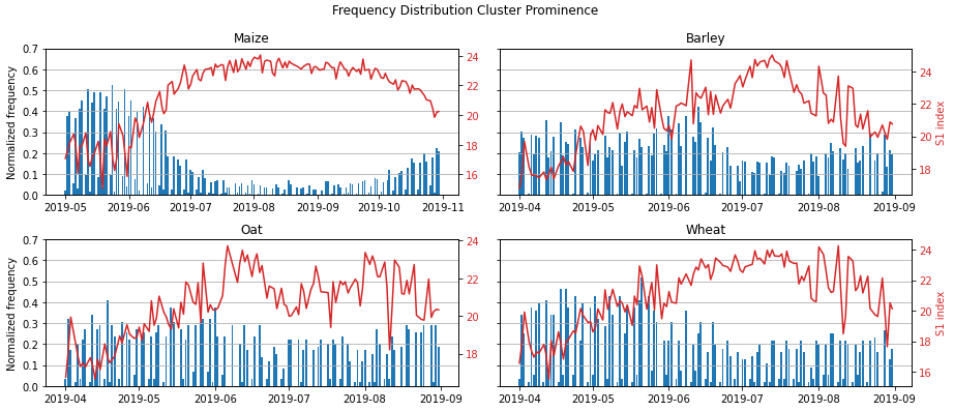

(c)

Figure 4.23: Normalized frequency distribution of the occurrences of high autocorrelation and (a) Altieri entropy, (b) cluster tendency, and (c) cluster prominence. Small bars are caused by observations from relative orbits covering only part of Flevoland, which are disadvantaged due to the normalisation with the total number of fields, and can be ignored for the purpose of the analysis.

The distributions ordered by crop type instead of metric are presented in Appendix I to see the metrics side by side per crop type. The differences between the metrics can be analysed by comparing the figures in Figure 4.23. This demonstrates two things. First, it shows a similar profile of the histograms in time, indicating the sensitivity to similar spatial patterns. Second, absolute value differences can be seen, especially between the Altieri entropy and the GLCM metrics. This could either be due to the higher sensitivity of the entropy or due to a less strict threshold.

A final note on the limitations of this method is that results and interpretations are susceptible to the choice of threshold values and time window of the autocorrelation. Both can be linked to the nature of the changes to detect the spatially and temporally relevant periods and should therefore be altered according to

their application.

4.3.2. Spatial consistency

To illustrate how the persistent spatial patterns are extracted, Appendix K presents an image corresponding to each step of the spatial processing (steps 2 to 8 in Figure 3.3). This section will first present the results of the applied method and the discussion on this result. After, it discusses possible methods to implement the found patterns in the BP.

Extracting persistent clusters

Step 1 of the process is the selection of a suitable period. For this example, a period is selected for which all three spatial metrics were above the threshold values but far enough in the growing season that there is already vegetation. This period is from June 19 to 23. The rasters from this period are shown in Figure 4.24.

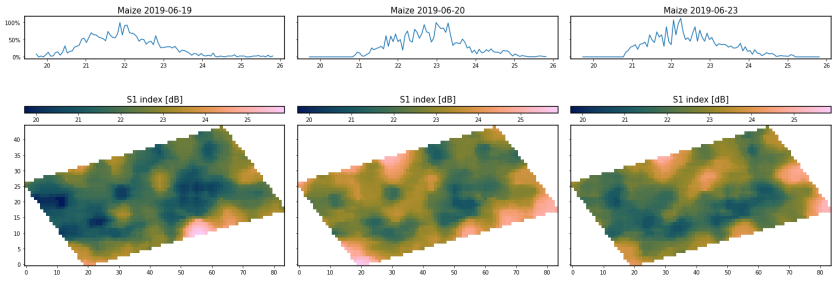

Figure 4.24: S1 index rasters of the selected period with high autocorrelation and high spatial metric values.

The following steps (2 to 5) create a mask for each raster, marking the pixels classified as persistent throughout the series. The persistent clusters were obtained by applying this final mask to Figure 4.24, as shown in Figure 4.25. The histogram shows here that, for this field, the consistency of the pixels does not appear to be linked to backscatter intensity. The histograms of the original and filtered rasters show similar shapes and ranges, indicating that no particular values have been filtered. The range did decrease slightly, presumably because outliers are not constant in time and thus deviate from the mean. Furthermore, it can be seen that the pixels grouped as clusters do not necessarily have the same backscatter values. The isolated spherical clusters on the bottom left do, but the pixels connecting the spherical parts of the clusters deviate.

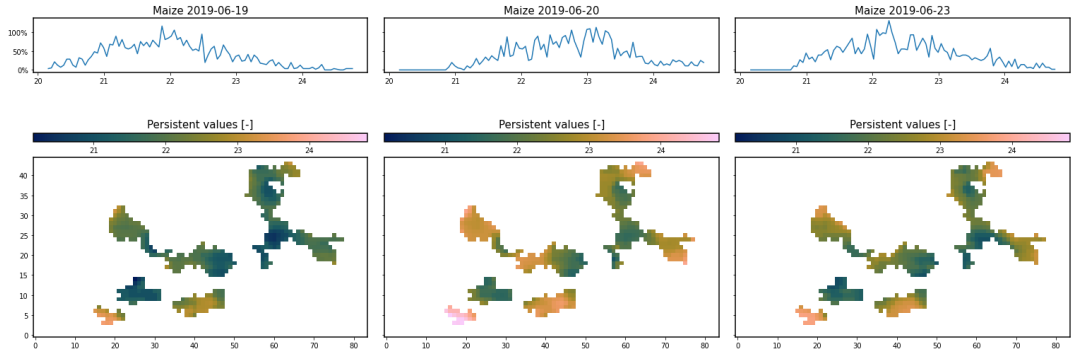

Figure 4.25: S1 index rasters filtered by persistent clusters in data.

During these persistent S1 index rasters, one NDVI observation was acquired, which is shown in Figure 4.26. Comparing these filtered rasters to the NDVI raster, no obvious similarities between patterns can be seen.

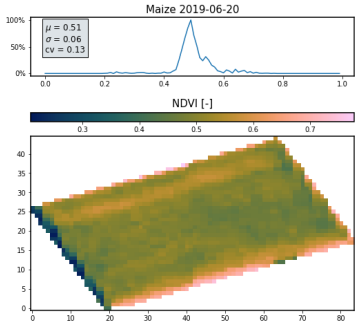

Figure 4.26: NDVI raster from the period of S1 index raster series.

The NDVI displays a light horizontally striped pattern, which is neither visible in the filtered rasters from Figure 4.25, nor in the unfiltered S1 index rasters in Figure 4.24. In Section 4.1.1, it was established that stem elongation is expected to occur during this period. The structure changes could therefore induce the patterns in the rasters. However, in-situ data would be necessary to validate this.

A limiting factor in this analysis is the result's dependency on several selected parameters. More research is crucial to optimise the use of these parameters, as they strongly influence the classification of clusters as persistent. For instance, by adjusting the bin size of the metrics, clusters will become larger as the intra-cluster variability can be larger. Other examples of the influence of parameters and a sensitivity analysis of these parameters can be found in Appendix J.

If the user is mainly interested in harvest detection (of part of the field), a longer period of autocorrelation might be expected since this is a (semi) permanent change. Nevertheless, if the user is interested in monitoring the phenological stages of his or her crops, more dynamic cluster changes could be used as indicators of structure and VWC changes in the crop. Furthermore, even in the latter example, refinements could be made between, e.g. alarming conditions of part of the field lagging or everyday checks. One would require stricter threshold values than the other or other parameter settings such as bin sizes.

Using spatial patterns as parameter BP fusion

In order to use the information on pattern consistency in the BP, a method must be established to detect persistent clusters and to weigh the rasters accordingly. There are three possibilities to adjust these weights based on spatial consistency:

1. Time - increasing the weight of the whole S1 index raster
2. Space - redistributing the weight locally where persistent clusters are detected
3. Time & space - spatially redistributing the temporally increased weight

Firstly, weights could be adjusted in time by, for instance, increasing the weight for each sequential observation with at least an X % or an X number of clusters. However, if a significant area in the field is harvested and has a persistent cluster of other backscatter values, but the rest of the field is strongly fluctuating, these fluctuations will also be introduced in the output signal.

Secondly, by adjusting the weights in space, fluctuations in parts of the field would not be a limiting factor as the weights would be redistributed locally. However, this could introduce unwanted discontinuities in the output signal when using a mask (such as Figure K.3). Alternatively, one could introduce a mask based on the inverse variance of the rasters in the series, where more persistent pixels are assigned higher weights. A disadvantage of applying this method like that would be that no morphological operations to remove single pixels or small holes can be applied. To compensate for this, other operations are necessary, e.g. spatial filters.

Thirdly, the mentioned possibilities could be combined: increasing the weight per raster as each subsequent raster meets the requirements and redistributing the increased weights accordingly. An advantage of this would be that, although clusters become smaller as time increases, the weight would become even higher. A disadvantage of this method would be that it introduces more complexity to the output signal, possibly making interpretation more difficult.

Additionally, if the method is to be implemented, it must be transformed to be used in near real-time. A possible solution would be to compute the rolling mean of the rasters to compute the differences. The time window of this mean could be varied depending on the application. For dynamic changes, a time window of two observations could be set, providing spatial consistency from the third observation onwards. However, this would not show the difference between clusters with longer periods of consistency and those with consistency only within the time window. The opposite will happen by selecting a larger time window, so a trade-off would have to be made.

Alternatively, one could consider adding the persistent clusters as an extra layer or as metadata to the product. That way, no compromise has to be made due to the fusing of the signals. However, this would consequently not improve biomass estimations but would serve a different function. The best method is application dependent and falls outside the scope of this thesis.

4.3.3. Conclusions on pattern consistency

Field-based time series of the combined metrics and autocorrelation demonstrated the complementary nature of the two. Applying the method to all fields showed the decreased consistency of all crops during their maximum S1 index values, which is most significant for maize. For the other cereals, changes in plant structure seemed to influence the frequency of consistent patterns. Moreover, the developed method to extract persistent spatial clusters appears effective, but parameters must be fine-tuned depending on the application. Finally, the example showed that the pattern classified as persistent was not recognizable in the NDVI image, demonstrating its complementary value. The detected patterns could be implemented in the BP by adjusting the weights of the S1 index in time, space or both, which all come with advantages and complications.

4.4. Implementing spatial data in the Biomass Proxy

This section provides an analysis of the spatial BP data for varying static weights for the fusion of the S1 index rasters with the NDVI rasters. First, the weighted rasters of the maize field are presented throughout the growing season together with the clustered outputs. Second, the spatial correlation of all fields was combined per crop type as a function of the static weights.

4.4.1. Identifying radar-like spatial patterns

The sensitivity of the BP to the input spatial S1 index data was tested by plotting the selected field for each crop on the dates from Section 4.1.2. For conciseness, only one day of the maize field will be shown and discussed extensively since the other days and crops yielded similar results. These results can be found in Appendix L. Recall that the BP uses the spatial information of the NDVI and S1 index to distribute the time series values over the field. Because a rolling mean is used in the fusion process, a lag is introduced in the time series, influencing the average field value of the BP. To better understand the signal values, the time series with the selected date is shown in Figure 4.27.

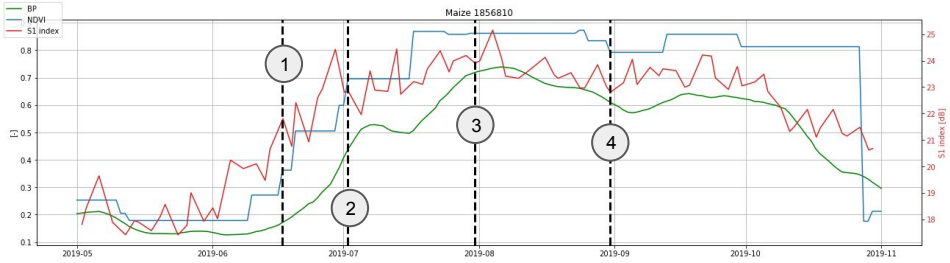

Figure 4.27: Time series of the maize field with four days of interest at which the static weight sensitivity analysis was performed.

In Figure 4.28, the weighted BP rasters (a) and the corresponding clusters (b) of the third day can be seen. Due to the homogeneous NDVI signal, the detected clusters in Figure 4.28b originate from the S1 index signal. Two interesting observations can be done from this example. Firstly, comparing the S1 index raster with the weighted BP $w_{s1} = 1$ raster, the patterns appear dissimilar. This is caused by a combination of temporal averaging and scaling of the spatial S1 index. Recall that the S1 index values are scaled to the NDVI scale to fuse the two signals. The scaling is done using an exponential function with a linear tail, causing the high S1 index values to be amplified and the low values to be smoothed. Since the current BP has a maximum S1 index contribution of 40% because of the $w_{s1} = 0.075$, this cannot occur. However, this effect should be kept in mind if dynamic weights allow exceeding this limit.

Secondly, there is a clear difference between the clustered raster of $w_{s1} = 0.1$ and $w_{s1} = 0.25$, indicating a tipping point between these values in which the cluster configuration changes. By narrowing this down, it could be determined for which contribution of the S1 index the radar features become visible in the BP raster. With this information, the weights of the S1 index could be increased during a period of saturation in the NDVI, enabling it to provide in-field variability during this period which it does not provide now (see the BP raster $w_{s1} = 0.075$ in Figure 4.28a).

Note that, although clusters are detected from $w_{s1} = 0.25$ onwards, spatial correlation at this static weight is still very low ($r = 0.05$). For this example, spatial correlation of the S1 index with the BP rasters only exceeds the correlation between the NDVI and BP rasters for a static weight of $w_{s1} = 0.59$ onwards.

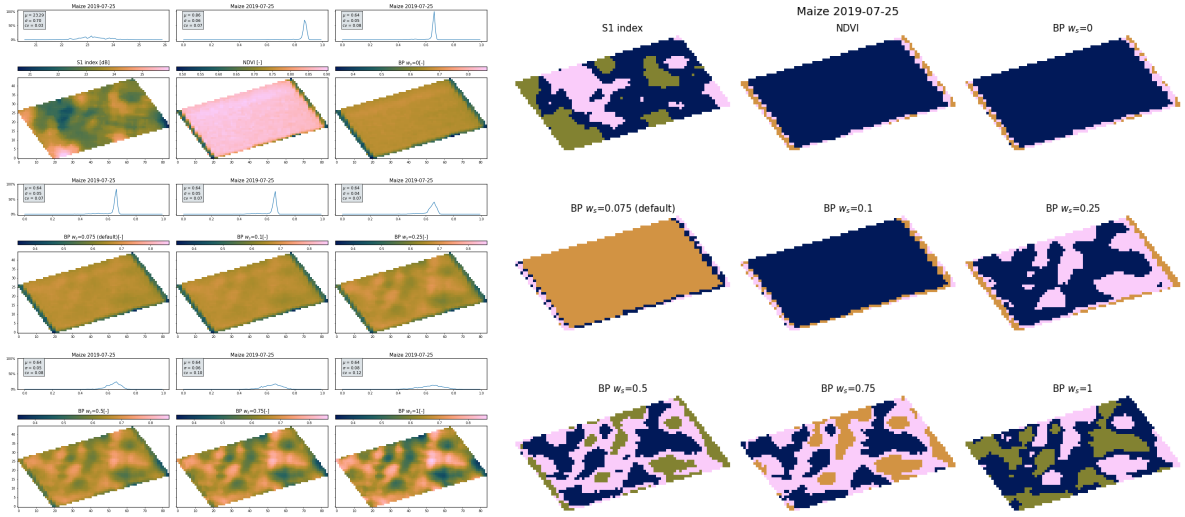

(a) (b)

Figure 4.28: BP weighted rasters for varying static weights of day 3, regular (a) and clustered (b).

A few side notes apply here, however. One is that the weight of this tipping point will be different for all fields, crops, or parts of the growing season. As discussed, the scaling function smoothes the S1 index if values are low or alters the pattern by amplifying certain values and diminishing others. In addition, patterns in the NDVI rasters will alter the exact tipping point. Applying such sensitivity analysis on a more narrow scale is thus more complex due to the dependence on multiple variables. However, a first step could be taken by performing such an analysis during a period of NDVI saturation to exclude the NDVI patterns as a variable.

Second, note that these rasters were all computed on days with full-coverage NDVI observations. Since the final weight is a product of the dynamic and static weights, the S1 index contribution increases over time. Thus spatial features from the radar could become visible in the BP raster at lower weights than might appear from this analysis. For a static weight of 0.075, the contribution of the S1 index to the output image would be the same after approximately 12 days as the contribution with static weight of 0.25 on the date with an NDVI observation.

4.4.2. Spatial correlation

The spatial correlations were computed per crop type to quantify the relationship between the S1 index and the NDVI rasters with the weighted BP rasters. Results for all crops are shown in Figure 4.29.

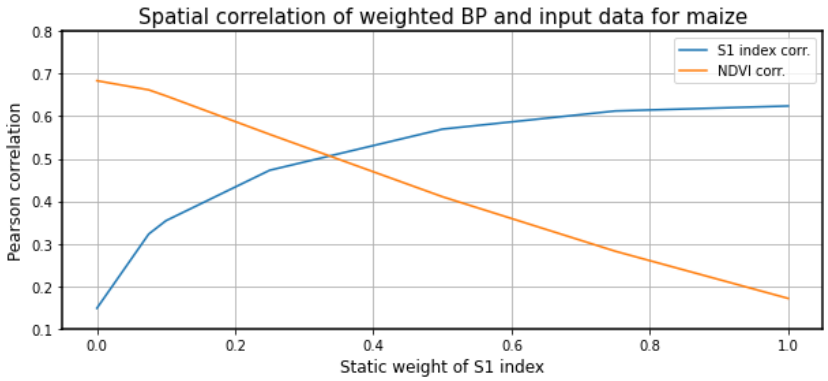

(a) Intersection point at weight=0.34 with Pearson correlation 0.51.

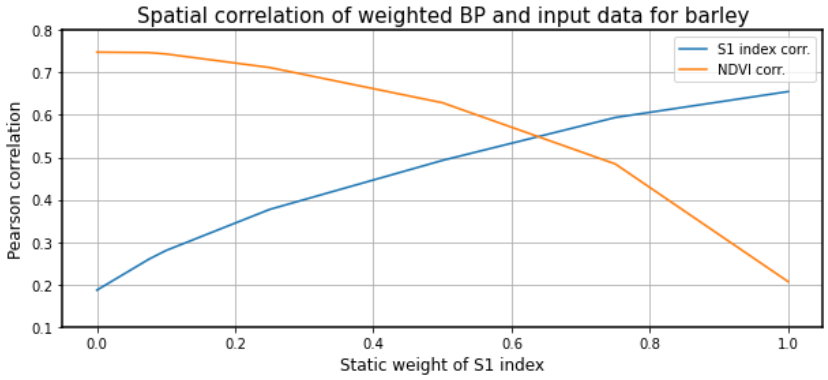

(b) Intersection point at weight=0.64 with Pearson correlation 0.55.

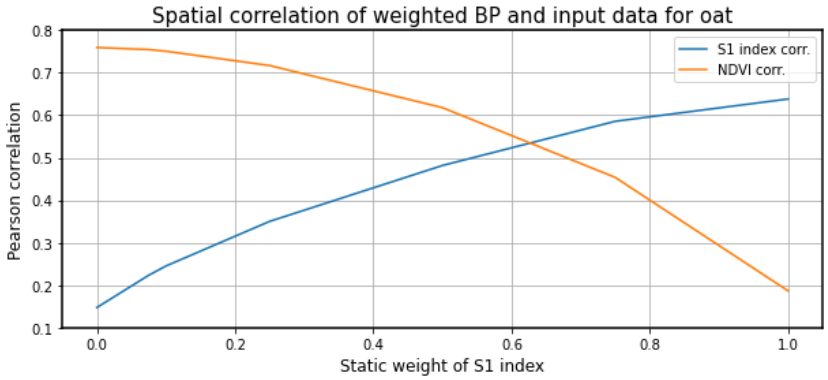

(c) Intersection point at weight=0.63 with Pearson correlation 0.53.

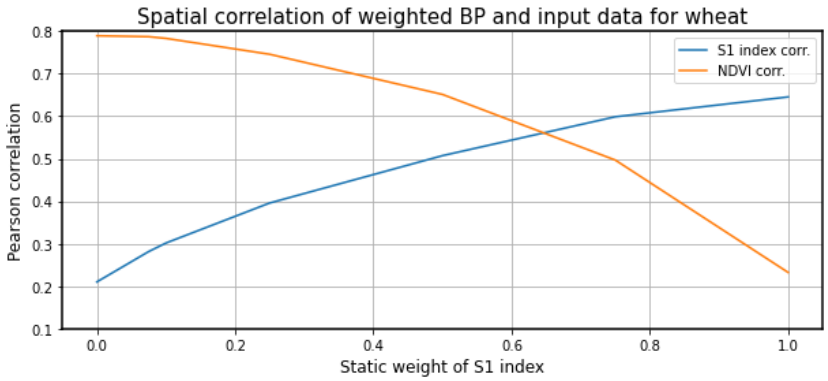

(d) Intersection point at weight=0.65 with Pearson correlation 0.56.

Figure 4.29: Spatial Pearson correlation of all fields per crop type.

The results demonstrate three things. Firstly, it shows that even for $w_s = 0$ and $w_s = 1$, the correlations do not equal 1. As discussed in the previous section, this is due to the averaging and the scaling of the signals and does not depend on the fusion.

Secondly, the relationship between the input signals and the weighted BP rasters is almost identical for the cereal types. The intersection points for barley, oat and wheat are at static weights of 0.64, 0.63 and 0.65, respectively. In addition, the Pearson correlation values at these intersection points are 0.55, 0.53 and 0.56.

Thirdly, there is a clear discrepancy between the spatial correlation relationships between cereals and maize. Although the Pearson correlation at the intersection is similar (0.56), the static weight at the intersection of 0.33 is significantly lower than the static weights at the intersections of the cereals. This is an intriguing result, which could be caused by the structure differences between the cereals and maize or by the relatively long period of NDVI and S1 index saturation of maize. On average, 29% of the days in the growing season have an NDVI ≥ 0.80 for maize, against 6% for barley, 0% for oat and 13% for wheat. Because maximum S1 index values deviate, the amount of saturation of the S1 index depends on the definition of saturation. Since the maximum value of the S1 index for maize is lower than that of, e.g. barley but is more stable, it was chosen to define S1 index saturation based on the maximum value of the respective crop time series, i.e. observations are saturated when the S1 index $\geq 0.90 \cdot max(S1)$. This results in an average of 66% days in the growing season with a saturated S1 index signal against 29% for barley, 37% for oat and 42% for wheat.

This could explain the difference in spatial correlation between maize and cereals but would neglect the differences between the cereal types, while these demonstrate almost identical spatial correlations. Therefore, plant structure likely plays a role in the sensitivity to the S1 index. This may explain why the radar-like pattern became visible at the static weight of $w_s = 0.25$ for maize, while it only became visible for $w_s = 0.5$ for oat, wheat and two from the three barley rasters.

Alternatively, the discrepancy could also be caused by the definition of the growing season. Since the cereals were analysed for the same dates (April 1 to September 1), and maize has a slightly longer and later growing season (May 1 to November 1), external factors that influence the relationship between the BP and the input signals could play a significant role here. Correlation values could be compared for the same crops and growing seasons in other years to verify this.

Note that for the current settings of the BP, a static weight of 0.075 is used, at which point the difference is smaller between maize and the cereals, but can already be seen in Figure 4.29. The correlations of the input signals at the default setting of the BP are presented in Table 4.3, showing the skewed representation of the signals for the different crops.

Table 4.3: Spatial Pearson correlation of input signals with the Biomass Proxy with the default static S1 index weight of $w_s = 0.075$.

	Maize	**Barley**	**Oat**	**Wheat**
NDVI correlation	0.67	0.75	0.75	0.79
S1 index correlation	0.33	0.27	0.24	0.28

Although $w_s = 0.075$ is far from the 'tipping point' for all crops, in Figure L.2 it was shown that even at this static weight, some spatial features from the radar data were detected by the K-means algorithm. This presents a limitation of this method: it does not show when the first (most prominent) clusters from the radar data become visible. Since the goal is not to increase the weight until the BP looks like the S1 index raster but to include the *relevant* S1 index spatial information, adjusting the weight such that only the most prominent clusters become visible in the BP is sufficient. Another limitation of this method is that it does not account for the different phenological stages and, thus, not the different backscatter responses. This section has highlighted the important role saturation (and possibly structure) plays in the correlation between the input signals and the BP, and Section 3.4 and Appendix L show the spatial examples of change throughout the growing season. However, the methods used to obtain the results in the latter section and appendix are not scalable. A compromise must be made in which general insights, such as sensitivity to saturation and structure, are supported by small-scale analyses at the field level.

4.4.3. Conclusions on implementing spatial data in the Biomass Proxy

It was shown that, for the example, clusters only became visible at a static weight of 0.25, both visually and from the K-means algorithm. Additionally, the analysis demonstrated that even for the extreme case of $w_s = 1$, the BP is not the same as the S1 index due to scaling and temporal averaging, emphasising weights should

be adjusted deliberately. Moreover, it showed the role saturation in the NDVI plays in the ability to recognise clusters.

At crop-level, it was demonstrated that sensitivity to the static weights of the S1 index could be crop type dependent, but an inter-annual comparison is necessary to verify this. Differences in sensitivity are likely due to signal saturation, plant structure differences or definition of the growing season.

5

Conclusions and Recommendations

This thesis assessed the potential of spatial SAR signal from Sentinel-1 in the Biomass Proxy for monitoring agricultural fields in the Netherlands. This chapter contains the key points, main conclusions and recommendations for further research.

5.1. Conclusions

This section first presents the key points of this study by providing answers to the four research sub-questions. Then, the general conclusion of this thesis is discussed.

How do NDVI and SAR data describe biophysical changes of various crops in the temporal and spatial domains?
The S1 index, the NDVI, and the radar polarisations were analysed temporally and spatially to evaluate the signal responses of biophysical changes. The averaged time series in the temporal analysis were in agreement with reviewed literature, and the principal phenological stages of maize and the three types of cereal could be recognised. Moreover, the literature review and time series showed that for the cereals, plant structure changes clearly influenced the S1 signal but not the NDVI.

The spatial analysis demonstrated the inherent differences between the signals. The spatial information from the radar polarisations was dominated by speckle and could, therefore, not be analysed from isolated rasters. It was found that the NDVI was able to detect the greenness of the monitored crops with high spatial resolution but that the signal quickly became saturated and could, therefore, not capture differences in later phenological stages. Lastly, the S1 index displayed spatial patterns throughout the growing season, presumably caused by VWC, plant structure or soil moisture variability. Distinguishing causes from the spatial S1 index data alone is, therefore, not reliable, and field measurements should be carried out to verify the causes of spatial patterns.

What spatial metrics can be used in which situations as indicators for clustering of the spatial S1 index data?
The ability of the Altieri entropy, cluster tendency, and cluster prominence to describe spatial clustering of the S1 index data was assessed. The Altieri entropy showed the lowest variability in the selected threshold for all crops and between crops and could be suitable as a global indicator. The cluster tendency is sensitive to grouping of similar backscatter values, making it suitable for applications where few false negatives are desired. However, intra-cluster variability of large clusters could lead to cluster division, and homogeneous areas in between clusters could be misleading. The cluster prominence proved promising in detecting dominant clusters with strong contrast to their surroundings but could not capture clusters with a gradient around the edge. This characteristic could be useful for anomaly detection. All three metrics did not seem to capture strong changes in the S1 index, making the metrics unsuitable for harvest detection.

How often are clusters in the radar signal persistent, and what causes these persistent clusters?
Histograms of the normalised occurrences of persistent patterns in the spatial S1 data were created for each crop and metric. Periods with the lowest amount of consistency corresponded to periods of the maximum

S1 index values and varied between 0% and 20%. The period with the most consistency was observed at the start of the growing season, where, on average, 60% of all fields contained persistent clusters. Spatial clustering is presumably driven by soil moisture and roughness variations and is thus more consistent than growing vegetation. Besides this, the frequency of persistent clusters decreased during the stem elongation stages and increased during the heading stages for all cereals. Comparing a persistent pattern to an NDVI observation in the same period showed that the optical imagery could not capture the pattern. Therefore, it was not caused by biophysical parameters linked to NDVI.

How is the Biomass Proxy influenced by the static weight of the Sentinel-1 data, and how does this change throughout the growing season?
The influence of the static weight was tested by performing a sensitivity analysis on the BP, which showed that, on the days with an NDVI observation, spatial features from the S1 index data could be detected for a static weight of 0.25 for all cases of the example and rasters became more similar to the S1 index for even higher static weights. However, due to the scaling and temporal averaging of the S1 index, clusters become more prominent and are compressed, and the BP never becomes identical to the S1 index.

Furthermore, the comparison between the spatial correlations showed that the BP's sensitivity to the input signal differed between maize and the cereals. This is likely due to either plant structure or signal saturation, and will therefore vary throughout the growing season.

Main conclusion
The main objective of this study was to assess the potential value of the spatial SAR signal from Sentinel-1 in the Biomass Proxy for monitoring agricultural fields in the Netherlands. Extensive temporal and spatial analyses in Section 4.1 demonstrated the complexity of the spatial SAR data; it contains elements with a dynamic nature that do not necessarily correspond to biomass. It was assumed that consistent SAR patterns in the spatial signal correspond to biophysical changes in the monitored crops that are of interest to the user. In Section 4.2, it was shown that consistency of spatial patterns could be detected by combining spatial autocorrelation with different spatial metrics. However, results are sensitive to the type of metric, metric parameters and thresholds for consistency. In Section 4.3.1, it was shown that the timing and frequency of consistent patterns depend on crop type. Furthermore, in Section 4.3.2, a period where consistency was determined temporally showed a spatial pattern which could not be observed in the corresponding NDVI observation, indicating the complementary value of the spatial SAR data. There are multiple methods to implement the detected patterns, each with advantages and complications. Finally, Section 4.4 evaluated the effect of increasing the contribution of the S1 index in the BP, demonstrating that the sensitivity to the input signal presumably depends on plant structure and signal saturation.

This research has made the first steps in understanding the spatial data, and the insights gained could be valuable in redefining the spatial weights of the S1 index for varying applications. However, a deeper understanding of these patterns is crucial to implement the detected patterns to improve the BP. In-situ data is essential for this cause, but with the knowledge of when and where the patterns occur, targeted research can be done to better understand the spatial SAR signal and, thereby, optimally use all available information.

In conclusion, the method proposed in this thesis demonstrated the complementary value of the spatial SAR data to the NDVI and, therefore, the promising potential. Although limitations exist, this framework could support the next steps in utilising radar data spatially and consequently contribute to the transition towards precision agriculture, which could play a crucial part in the challenge of meeting the global ever-growing demand for food production.

5.2. Recommendations

The results and discussion highlight several limitations of the method and the need for validation data. This section presents some suggestions for future research. First, suggestions are made regarding the methods used in this thesis. Second, recommendations are given on possible implementation in the biomass proxy and on a strategy for future field work.

Method improvements

The first recommendation to improve the methods presented in this thesis is to assess the influence of varying parameters of the computations performed. For instance, the bin sizes of the metric computations lie at the basis of a better part results since slightly larger or smaller bin sizes could strongly influence the output values of the spatial metrics. Another example of this is the definition of the distance intervals of the Altieri entropy.

Second, an objective method to determine the threshold values for the spatial metrics should be implemented. This would increase the reproducibility of the results and support the interpretation of the rasters.

Third, there is room for improvement in the metric selection and analysis. The current method only compared three entropy features and twenty-four GLCM features, but there are many more entropy features and features based on co-occurrences available. Ideally, the method should be replicated in a study where spatial validation data is available, so suitable metrics could be selected based on the biophysical data. Other clusters could potentially be understood if certain metric values could be derived from a cluster with a known cause.

The final suggestion for method improvements would be distinguishing between polarisations and between relative orbits. Since the different polarisations interact differently with the vegetation, it might be possible to isolate the cause for certain patterns. Additionally, distinguishing between rasters obtained from varying relative orbits could show if this influences the spatial output. Currently, orbit correction is only implemented in the temporal domain in the Biomass Proxy. A potential bias should be taken into account if the spatial weight of the S1 index is increased.

Future research

If the spatial S1 index data were to be increased in the BP, decisions would have to be made regarding the data representation. For instance, with the obtained knowledge of how strongly structure changes in cereals influence the output signal, increasing the weight of the S1 index would not make the output a better proxy for biomass. As discussed, the BP could potentially add this information as an extra layer in the output, which is another product. However, biomass estimation could also be improved from the S1 index signal if changes induced by the VWC could be isolated. A possible method to isolate these changes would be using some type of signal decomposition (e.g. Pauli decomposition), which analyses the scattering components. Ideally, this could be combined with fieldwork to narrow down the causes of the scattering. This information could support the biomass estimation while, if desired, diminishing the effects of structure or soil.

One key aspect that came forward in this thesis is the need for validation data. This data is essential to improve understanding of the signals and would help decision-making in the design of the algorithm. However, as addressed in Section 1.1, spatial biomass data is complicated to obtain since it requires destructive samples, and spatial patterns can, therefore, not be analysed in time. However, by first creating a thorough understanding of the link between the biophysical parameters and the biomass, field measurements could focus on obtaining these parameters, such as the phenological stage. The spatial data would not only support the understanding of the spatial patterns but could also provide information on other fields with similar metric values.

References

Abdikan, S., Sekertekin, A., Ustunern, M., Balik Sanli, F., & Nasirzadehdizaji, R. (2018). Backscatter analysis using multi-temporal Sentinel-1 SAR data for Crop growth of Maize in Konya Basin, Turkey. *International Archives of the Photogrammetry, Remote Sensing and Spatial Information Sciences - ISPRS Archives*, *42*(3), 9–13. doi: 10.5194/isprs-archives-XLII-3-9-2018

Alberga, V., Satalino, G., & Staykova, D. K. (2008, 6). Comparison of polarimetric SAR observables in terms of classification performance. *International Journal of Remote Sensing*, *29*, 4129–4150. Retrieved from https://www.tandfonline.com/action/journalInformation?journalCode=tres20 doi: 10.1080/01431160701840182

Al-Doski, J., Mansor, S. B., & Shafri, H. Z. M. (2013). Image Classification in Remote Sensing. *Journal of Environment and Earth Science*, *3*(10). Retrieved from www.iiste.org

Al Mashagbah, A. F. (2016). The Use of GIS, Remote Sensing and Shannon's Entropy Statistical Techniques to Analyze and Monitor the Spatial and Temporal Patterns of Urbanization and Sprawl in Zarqa City, Jordan. *Journal of Geographic Information System*, *08*(02), 293–300. doi: 10.4236/JGIS.2016.82025

Altieri, B. L., Cocchi, D., & Roli, G. (2018). A new approach to spatial entropy measures. *Environ Ecol Stat*, *25*, 95–110. Retrieved from https://doi.org/10.1007/s10651-017-0383-1 doi: 10.1007/s10651-017-0383-1

Altieri, L., Cocchi, D., & Roli, G. (2017). The use of spatial information in entropy measures. (March). Retrieved from http://arxiv.org/abs/1703.06001

Andela, N., Liu, Y. Y., M. Van Dijk, A. I., De Jeu, R. A., & McVicar, T. R. (2013). Global changes in dryland vegetation dynamics (1988-2008) assessed by satellite remote sensing: Comparing a new passive microwave vegetation density record with reflective greenness data. *Biogeosciences*, *10*(10), 6657–6676. doi: 10.5194/BG-10-6657-2013

Aranganayagi, S., & Thangavel, K. (2007). Clustering Categorical Data using Silhouette Coefficient as a Relocating Measure. In *International conference on computational intelligence and multimedia applications*. IEEE. doi: 10.1109/ICCIMA.2007.328

Arun, P. V. (2014). A Comparative Analysis on the Applicability of Entropy in Remote Sensing. *Indian Society of Remote Sensing*, *42*(1), 217–226. doi: 10.1007/s12524-013-0304-1

Asner, G. P. (1998, 6). Biophysical and Biochemical Sources of Variability in Canopy Reflectance. *Remote Sensing of Environment*, *64*(3), 234–253. doi: 10.1016/S0034-4257(98)00014-5

Assinck, F. (2006). *Grondsoortenkaart - WUR*. Retrieved from https://www.wur.nl/nl/show/Grondsoortenkaart.htm

Awad, M. M. (2019). Toward Precision in Crop Yield Estimation Using Remote Sensing and Optimization Techniques. *MDPI*, *9*(54). Retrieved from www.mdpi.com/journal/agriculture doi: 10.3390/agriculture9030054

BBA, BSA, & IVA. (2001). *Growth stages of mono-and dicotyledonous plants - BBCH Monograph* (Tech. Rep.). Federal Biological Research Centre for Agriculture and Forestry.

Beare, R., Lowekamp, B., & Yaniv, Z. (2018). Image Segmentation, Registration and Characterization in R with SimpleITK. *Journal of statistical software*, *86*. Retrieved from /pmc/articles/PMC6168008//pmc/articles/PMC6168008/?report=abstracthttps://www-ncbi-nlm-nih-gov.tudelft.idm.oclc.org/pmc/articles/PMC6168008/ doi: 10.18637/JSS.V086.I08

Behzad, A., Aamir, M., Raza, S. A., Qaiser, A., Fatima, S. Y., Karamat, A., & Mahmood, S. A. (2019, 6). Estimation of Wheat Area using Sentinel-1 and Sentinel-2 Datasets (A Comparative Analysis). *International Journal of Agriculture & Sustainable Development*, *01*(03), 81–93. doi: 10.33411/ijasd/2019010306

Blaes, X., Defourny, P., Wegmüller, U., Vecchia, A. D., Guerriero, L., & Ferrazzoli, P. (2006). C-band polarimetric indexes for maize monitoring based on a validated radiative transfer model. *IEEE Transactions on Geoscience and Remote Sensing*, *44*(4), 791–799. doi: 10.1109/TGRS.2005.860969

Blickensdörfer, L., Schwieder, M., Pflugmacher, D., Nendel, C., Erasmi, S., & Hostert, P. (2022). Mapping of crop types and crop sequences with combined time series of Sentinel-1, Sentinel-2 and Landsat 8 data for Germany. *Remote Sensing of Environment*, *269*(112831). doi: 10.1016/j.rse.2021.112831

Broder, A., Garcia-Pueyo, L., Josifovski, V., Vassilvitskii, S., & Venkatesan, S. (2014, 2). Scalable K-Means by Ranked Retrieval. In *Wsdm*. New York. Retrieved from http://dx.doi.org/10.1145/2556195.2556260. doi: 10.1145/2556195.2556260

Brown, C. E. (1998). Coefficient of Variation. *Applied Multivariate Statistics in Geohydrology and Related Sciences*, 155–157. Retrieved from https://link-springer-com.tudelft.idm.oclc.org/chapter/10.1007/978-3-642-80328-4_13 doi: 10.1007/978-3-642-80328-4{_}13

Butt, B. (2018, 6). Environmental indicators and governance. *Current Opinion in Environmental Sustainability*, *32*, 84–89. doi: 10.1016/J.COSUST.2018.05.006

Cable, J. W., Kovacs, J. M., Jiao, X., & Shang, J. (2011). Agricultural Monitoring in Northeastern Ontario, Canada, Using Multi-Temporal Polarimetric RADARSAT-2 Data. *Remote Sensing*, *6*, 2343–2371. Retrieved from www.mdpi.com/journal/remotesensingArticle doi: 10.3390/rs6032343

Canty, M. J. (2014). *Image analysis, classifaction and change detection in remote sensing : with algorithms for ENVI/IDL and Python* (Third ed.). Boca Raton: CRC Press.

Chakhar, A., Hernández-López, D., Ballesteros, R., & Moreno, M. A. (2021). Improving the Accuracy of Multiple Algorithms for Crop Classification by Integrating Sentinel-1 Observations with Sentinel-2 Data. *Remote Sensing*, *13*(243). Retrieved from https://doi.org/10.3390/rs13020243 doi: 10.3390/rs13020243

Chang, J., & Shoshany, M. (2016, 11). Mediterranean shrublands biomass estimation using Sentinel-1 and Sentinel-2. In *International geoscience and remote sensing symposium (igarss)* (Vol. 2016-Novem, pp. 5300–5303). Institute of Electrical and Electronics Engineers Inc. doi: 10.1109/IGARSS.2016.7730380

Cover, T. M., & Thomas, J. A. (2005). *Elements of Information Theory* (2nd ed.). Hoboken, N.J.: John Wiley and Sons. Retrieved from https://onlinelibrary-wiley-com.tudelft.idm.oclc.org/doi/book/10.1002/047174882X doi: 10.1002/047174882X

Cui, M. (2020, 10). Introduction to the K-Means Clustering Algorithm Based on the Elbow Method. *Accounting, Auditing and Finance*, *1*(1), 5–8. Retrieved from http://www.clausiuspress.com/article/592.htmlhttp://www.clausiuspress.com/article/592.html#abstract doi: 10.23977/ACCAF.2020.010102

De Bernardis, C., Vicente-Guijalba, F., Martinez-Marin, T., & Lopez-Sanchez, J. M. (2016). Contribution to Real-Time Estimation of Crop Phenological States in a Dynamical Framework Based on NDVI Time Series: Data Fusion with SAR and Temperature. *IEEE Journal of Selected Topics in Applied Earth Observations and Remote Sensing*, *9*(8), 3512–3523. doi: 10.1109/JSTARS.2016.2539498

Dumitru, C. O., & Datcu, M. (2013). Information content of very high resolution SAR images: Study of feature extraction and imaging parameters. *IEEE Transactions on Geoscience and Remote Sensing*, *51*(8), 4591–4610. doi: 10.1109/TGRS.2013.2265413

Earth Observation Research Branch Team. (2011). Crop Identification and BBCH Staging Manual: SMAP-12 Field Campaign. , 23.

ESA. (n.d.). *Single Look Complex - Sentinel-1 SAR Technical Guide - Sentinel Online*. Retrieved from https://dragon3.esa.int/web/sentinel/technical-guides/sentinel-1-sar/products-algorithms/level-1-algorithms/single-look-complex

ESA. (2012). *Sentinel-1: ESA's radar observatory mission for GMES operational services* (Vol. 1) (No. 1322). Retrieved from https://sentinel.esa.int/documents/247904/349449/S1_SP-1322_1.pdf

European Space Agency. (2012). *Sentinel-1 ESA's Radar Observatory Mission for GMeS Operational Services* (Tech. Rep.). Noordwijk: ESA communications. Retrieved from www.esa.int

Fang, P., Yan, N., Wei, P., Zhao, Y., & Zhang, X. (2021). Aboveground Biomass Mapping of Crops Supported by Improved CASA Model and Sentinel-2 Multispectral Imagery. *Remote Sensing*, *13*(2755). Retrieved from https://doi.org/10.3390/rs13142755 doi: 10.3390/rs13142755

Ferrazzoli, P., Paloscia, S., Pampaloni, P., Schiavon, G., Solimini, D., & Coppa, P. (1992). Sensitivity of Microwave Measurements to Vegetation Biomass and Soil Moisture Content: A Case Study. *IEE Transactions on Gescience and Remote Sensing1*, *30*(4).

Frantz, D. (2019, 5). FORCE—Landsat + Sentinel-2 Analysis Ready Data and Beyond. *Remote Sensing 2019, Vol. 11, Page 1124*, *11*(9), 1124. Retrieved from https://www.mdpi.com/2072-4292/11/9/1124/htmhttps://www.mdpi.com/2072-4292/11/9/1124 doi: 10.3390/RS11091124

Godfray, H. C. J., Beddington, J. R., Crute, I. R., Haddad, L., Lawrence, D., Muir, J. F., ... Toulmin, C. (2010, 2). Food security: The challenge of feeding 9 billion people. *Science*, *327*(5967), 812–818. Retrieved from https://www-science-org.tudelft.idm.oclc.org/doi/10.1126/science.1185383 doi: 10.1126/SCIENCE.1185383/ASSET/A8EAC75B-BEB7-481A-A81A-C845AFA2F0EE/ASSETS/GRAPHIC/327{_}812{_}F3.JPEG

Gómez-Chova, L., Jenssen, R., & Camps-Valls, G. (2012). Kernel Entropy Component Analysis for Remote Sensing Image Clustering. *IEEE GEOSCIENCE AND REMOTE SENSING LETTERS*, *9*(2). Retrieved from http://ieeexplore.ieee.org. doi: 10.1109/LGRS.2011.2167212

Google Developers. (2022). *Synthetic Aperture Radar (SAR) Basics*. Retrieved from https://developers.google.com/earth-engine/tutorials/community/sar-basics

Greenwood, M. C. (2014). *Intermediate Statistics with R* (3rd ed., Vol. 1). Montana: Montana State University. Retrieved from https://scholarworks.montana.edu/xmlui/bitstream/1/2999/10/Greenwood_Book_Version3p1_optimized.pdfhttps://scholarworks.montana.edu/xmlui/handle/1/2999 doi: 10.15788/2019.08.19

Groten, S. M. (1993). NDVI-crop monitoring and early yield assessment of burkina faso. *International Journal of Remote Sensing*, *14*(8), 1495–1515. doi: 10.1080/01431169308953983

Haralick, R. M., Shanmugam, K., & Dinstein, H. (1973). *Textural Features for Image Classification* (Tech. Rep.). doi: 10.1109/TSMC.1973.4309314

Hinds, M. R., Sofko, G. J., Wacker, A. G., & Koehler, J. A. (1993). Ku-band polarization characteristics of crops and fallow. *Radar Polarimetry*, *1748*(May), 47. doi: 10.1117/12.140633

Huang, S., Tang, L., Hupy, J. P., Wang, Y., & Shao, G. (2021). A commentary review on the use of normalized difference vegetation index (NDVI) in the era of popular remote sensing. *Journal of Forestry Research*, *32*(1), 1–6. Retrieved from https://doi.org/10.1007/s11676-020-01155-1 doi: 10.1007/s11676-020-01155-1

Interreg III. (n.d.). Praktijkgids Biologische akkerbouw Deel Zomertarwe.

Ji, L., & Peters, A. J. (2003, 9). Assessing vegetation response to drought in the northern Great Plains using vegetation and drought indices. *Remote Sensing of Environment*, *87*(1), 85–98. doi: 10.1016/S0034-4257(03)00174-3

Jiao, X., Mc Nairn, H., Shang, J., Pattey, E., Liu, J., & Champagne, C. (2011). The sensitivity of RADARSAT-2 polarimetric SAR data to corn and soybean leaf area index. *Canadian Journal of Remote Sensing*, *37*(1), 69–81. doi: 10.5589/m11-023

Khabbazan, S., Steele-Dunne, S. C., Vermunt, P., Judge, J., Vreugdenhil, M., & Gao, G. (2022, 1). The influence of surface canopy water on the relationship between L-band backscatter and biophysical variables in agricultural monitoring. *Remote Sensing of Environment*, *268*. doi: 10.1016/j.rse.2021.112789

Khabbazan, S., Vermunt, P., Steele-Dunne, S., Arntz, L. R., Marinetti, C., van der Valk, D., … van der Sande, C. (2019). Crop monitoring using Sentinel-1 data: A case study from The Netherlands. *Remote Sensing*, *11*(16). doi: 10.3390/rs11161887

KNMI. (n.d.). *Daggegevens van het weer in Nederland*. Retrieved from https://www.knmi.nl/nederland-nu/klimatologie/daggegevens

Kobayashi, H., & Dye, D. G. (n.d.). Atmospheric conditions for monitoring the long-term vegetation dynamics in the Amazon using normalized difference vegetation index. Retrieved from www.elsevier.com/locate/rse doi: 10.1016/j.rse.2005.06.007

Kogan', F., & Ciren', B. (1994). *Improvement in 1985-1993 NDVI time-series for world desert targets using post-launch calibration* (Tech. Rep.). doi: 10.1109/IGARSS.1994.399722

Kuester, T., & Spengler, D. (2018). Structural and spectral analysis of cereal canopy reflectance and reflectance anisotropy. *Remote Sensing*, *10*(11). doi: 10.3390/rs10111767

Kuusk, A. (1991, 9). Determination of vegetation canopy parameters from optical measurements. *Remote Sensing of Environment*, *37*(3), 207–218. doi: 10.1016/0034-4257(91)90082-H

Lacorn, M., Weiss, T., Wehling, P., Arlinghaus, M., & Scherf, K. (2019). Quantification of Wheat, Rye, and Barley Gluten in Oat and Oat Products by ELISA RIDASCREEN® Total Gluten: Collaborative Study, First Action 2018.15. *Journal of AOAC International*, *102*(5), 1535–1543. Retrieved from https://pubmed-ncbi-nlm-nih-gov.tudelft.idm.oclc.org/31284896/ doi: 10.5740/JAOACINT.19-0094

Lakna. (2019, 6). *What is the Difference Between Barley and Oats - Pediaa.Com*. Retrieved from https://pediaa.com/what-is-the-difference-between-barley-and-oats/

Laksono, A., Saputri, A. A., Pratiwi, C. I. B., Arkan, M. Z., & Putri, R. F. (2020, 10). Vegetation covers change and its impact on Barchan Dune morphology in Parangtritis Coast, Indonesia. *E3S Web of Conferences*, *200*, 02026. Retrieved from https://www.e3s-conferences.org/articles/e3sconf/abs/2020/60/e3sconf_icst2020_02026/e3sconf_icst2020_02026.html doi: 10.1051/E3SCONF/202020002026

Larranaga, A., Alvarez-Mozos, J., Albizua, L., & Peters, J. (2013). Backscattering behavior of rain-fed crops along the growing season. *IEEE Geoscience and Remote Sensing Letters*, *10*(2), 386–390. doi: 10.1109/LGRS.2012.2205660

Lee, J. S. (1983, 11). Digital image smoothing and the sigma filter. *Computer Vision, Graphics, and Image Processing*, *24*(2), 255–269. doi: 10.1016/0734-189X(83)90047-6

Lee, J. S., Jurkevich, L., Dewaele, P., Wambacq, P., Oosterlinck, A., & OOSTERLINCK Leuven-ESAT-Ml, A. K. (1994). Speckle filtering of synthetic aperture radar images: A review. *Remote Sensing Reviews*, *8*, 313–340. Retrieved from https://www.tandfonline.com/action/journalInformation?journalCode=grsr20 doi: 10.1080/02757259409532206

Lee, J.-S., & Pottier, E. (2009). *Polarimetric Radar Imaging* (1st ed.). Boca Raton. doi: https://doi.org/10.1201/9781420054989

Lee, J. S., Wen, J. H., Ainsworth, T. L., Chen, K. S., & Chen, A. J. (2009, 1). Improved sigma filter for speckle filtering of SAR imagery. *IEEE Transactions on Geoscience and Remote Sensing*, *47*(1), 202–213. doi: 10.1109/TGRS.2008.2002881

Leibovici, D. G., Claramunt, C., Le Guyader, D., & Brosset, D. (2014). Local and global spatio-temporal entropy indices based on distance-ratios and co-occurrences distributions. *International Journal ofGeographical Information Science*, *28*(5), 1061–1084. Retrieved from https://www.tandfonline.com/action/journalInformation?journalCode=tgis20 doi: 10.1080/13658816.2013.871284

Li, C., Li, H., Li, J., Lei, Y., Li, C., Manevski, K., & Shen, Y. (2019). Using NDVI percentiles to monitor real-time crop growth. *Computers and Electronics in Agriculture*, *162*, 357–363. Retrieved from www.elsevier.com/locate/compag doi: 10.1016/j.compag.2019.04.026

Li, H., & Reynolds, J. F. (1993). *A new contagion index to quantify spatial patterns of landscapes* (Vol. 8; Tech. Rep. No. 3).

Li, W., & Guo, Q. (2010). A maximum entropy approach to one-class classification of remote sensing imagery. *International Journal of Remote Sensing,*, *31*(8), 2227–2235. Retrieved from https://www.tandfonline.com/action/journalInformation?journalCode=tres20 doi: 10.1080/01431161003702245

Lievens, H., Demuzere, M., Marshall, H.-P., Reichle, R. H., Brucker, L., Brangers, I., ... De Lannoy, G. J. M. (2019). Snow depth variability in the Northern Hemisphere mountains observed from space. *Nature communications*, *10*(4629). Retrieved from https://doi.org/10.1038/s41467-019-12566-y doi: 10.1038/s41467-019-12566-y

Liu, C., Shang, J., Vachon, P. W., & McNairn, H. (2013). Multiyear crop monitoring using polarimetric RADARSAT-2 data. *IEEE Transactions on Geoscience and Remote Sensing*, *51*(4), 2227–2240. doi: 10.1109/TGRS.2012.2208649

Liu, J., Pattey, E., Miller, J. R., McNairn, H., Smith, A., & Hu, B. (2010, 6). Estimating crop stresses, aboveground dry biomass and yield of corn using multi-temporal optical data combined with a radiation use efficiency model. *Remote Sensing of Environment*, *114*(6), 1167–1177. doi: 10.1016/J.RSE.2010.01.004

Liu, X., Zhu, X., Pan, Y., Li, S., Liu, Y., & Ma, Y. (2016, 4). Agricultural drought monitoring: Progress, challenges, and prospects. *Journal of Geographical Sciences 2016 26:6*, *26*(6), 750–767. Retrieved from https://link.springer.com/article/10.1007/s11442-016-1297-9 doi: 10.1007/S11442-016-1297-9

Liu, Y. Y., van Dijk, A. I., McCabe, M. F., Evans, J. P., & de Jeu, R. A. (2013, 6). Global vegetation biomass change (1988-2008) and attribution to environmental and human drivers. *Global Ecology and Biogeography*, *22*(6), 692–705. doi: 10.1111/geb.12024

Liu, Y. Y., Van Dijk, A. I. J. M., De Jeu, R. A. M., Mccabe, M. F., & Evans, J. P. (2012). *Development and evaluation of a global long-term passive microwave vegetation product* (Vol. 14; Tech. Rep.).

López-Dekker, P., & De Zeeuw Van Dalsen, E. (2021). *Geodesy & Natural Hazards Module 2 : Synthetic Aperture Radar Fundamentals*. Delft: TU Delft.

Lopez-Sanchez, J. M., Vicente-Guijalba, F., David Ballester-Berman, J., & Cloude, S. R. (2013, 12). Estimating phenology of agricultural crops from space. In *Esa living planet symposium 2013*. Edinburgh, UK.

Lopez-Sanchez, J. M., Vicente-Guijalba, F., Erten, E., Campos-Taberner, M., & Garcia-Haro, F. J. (2017). Retrieval of vegetation height in rice fields using polarimetric SAR interferometry with TanDEM-X data. *Remote Sensing of Environment*, *192*, 30–44. Retrieved from http://dx.doi.org/10.1016/j.rse.2017.02.004 doi: 10.1016/j.rse.2017.02.004

Lu, J., Peng, M., & Lu, X. (2006). Information entropy of remote sensing images and its applications in image fusion. *Remote Sensing of the Environment: 15th National Symposium on Remote Sensing of China*, *6200*(June 2006), 62000I. doi: 10.1117/12.681714

Lv, Z., Hu, Y., Zhong, H., Wu, J., Li, B., & Zhao, H. (2010). Parallel K-Means Clustering of Remote Sensing Images Based on MapReduce. In *Lncs* (Vol. 6318, pp. 162–170).

MacDonald. (2011). Sentinel-1 Product Definition.

MacKay, D. J. C. (2003). *Information theory, inference, and learning algorithms*. Cambridge, UK ;: Cambridge University Press,.

Marsetič, A., Oštir, K., & Fras, M. K. (2015). Automatic Orthorectification of High-Resolution Optical Satellite Images Using Vector Roads. *IEEE TRANSACTIONS ON GEOSCIENCE AND REMOTE SENSING*, *53*(11). Retrieved from http://www.ieee.org/publications_standards/publications/rights/index.html doi: 10.1109/TGRS.2015.2431434

Maselli, F. (n.d.). Analysis of GAC NDVI Data for Cropland Identification and Yield Forecasting in Mediterranean African Countries Determining the current and potential extent of the Prosopis invasion in East Africa View project Integrated method for the Actual Evapotranspiration estimation on a regional scale View project Analysis of GAC NDVI Data for Cropland Identification and Yield Forecasting in Mediterranean African Countries. Retrieved from https://www.researchgate.net/publication/279965255

Mattia, F., Le Toan, T., Picard, G., Posa, F. I., D'Alessio, A., Notarnicola, C., ... Pasquariello, G. (2003). Multitemporal C-band radar measurements on wheat fields. *IEEE Transactions on Geoscience and Remote Sensing*, *41*(7 PART I), 1551–1560. doi: 10.1109/TGRS.2003.813531

Mc Nairn, H., & Brisco, B. (2004). The application of C-band polarimetric SAR for agriculture: A review. *Canadian Journal of Remote Sensing*, *30*(3), 525–542. doi: 10.5589/m03-069

McNairn, H., Duguay, C., Brisco, B., & Pultz, T. J. (2002, 5). The effect of soil and crop residue characteristics on polarimetric radar response. *Remote Sensing of Environment*, *80*(2), 308–320. doi: 10.1016/S0034-4257(01)00312-1

McNairn, H., & Shang, J. (2016). *Multitemporal Remote Sensing Book* (20th ed.; Y. Ban, Ed.). Stockholm, Sweden: Springer. doi: 10.1007/978-3-319-47037-5

Meivel, S., Maheswari, S., & Grade, S. (2020). *Optimization of Agricultural Smart System using Remote Sensible NDVI and NIR Thermal Image Analysis Techniques*. Retrieved from https://orcid.org/0000-0002-8717-3881

Meng, J., Du, X., & Wu, B. (2013). Generation of high spatial and temporal resolution NDVI and its application in crop biomass estimation. *http://dx.doi.org.tudelft.idm.oclc.org/10.1080/17538947.2011.623189*, *6*(3), 203–218. Retrieved from https://www-tandfonline-com.tudelft.idm.oclc.org/doi/abs/10.1080/17538947.2011.623189 doi: 10.1080/17538947.2011.623189

Meroni, M., d'Andrimont, R., Vrieling, A., Fasbender, D., Lemoine, G., Rembold, F., ... Verhegghen, A. (2021, 2). Comparing land surface phenology of major European crops as derived from SAR and multispectral data of Sentinel-1 and -2. *Remote Sensing of Environment*, *253*. doi: 10.1016/j.rse.2020.112232

Met, S. R. (1994). teelt van HAVER. (61).

Milk, M. (2021). *SpatialEntropy: A python implementation of spatial entropy*. Retrieved from https://github.com/Mr-Milk/SpatialEntropy#readme

Ministerie van Economische Zaken en Klimaat. (2019, 5). *PDOK BRP*. Retrieved from https://www.pdok.nl/introductie/-/article/basisregistratie-gewaspercelen-brp-

Miranda, N., & Meadows, P. J. (2015, 5). *Radiometric Calibration of S-1 Level-1 Products Generated by the S-1 IPF* (No. 1). European Space Agency. Retrieved from https://sentinels.copernicus.eu/documents/247904/685163/S1-Radiometric-Calibration-V1.0.pdf/66e69a62-11ae-4160-916b-f2b97cb8a350?t=1432307754000

Mkhabela, M. S., Bullock, P., Raj, S., Wang, S., & Yang, Y. (2011). Crop yield forecasting on the Canadian Prairies using MODIS NDVI data. *Agricultural and Forest Meteorology*, *151*, 385–393. doi: 10.1016/j.agrformet.2010.11.012

Mkhabela, M. S., Mkhabela, M. S., & Mashinini, N. N. (2005). Early maize yield forecasting in the four agro-ecological regions of Swaziland using NDVI data derived from NOAA's-AVHRR. *Agricultural and*

Forest Meteorology, *129*(1-9). Retrieved from www.elsevier.com/locate/agrformet doi: 10.1016/j.agrformet.2004.12.006

Moreira, A., Prats-iraola, P., Younis, M., Krieger, G., Hajnsek, I., & Papathanassiou, K. P. (2013, 3). A Tutorial on Synthetic Aperture Radar. *IEEE Geoscience and Remote Sensing Magazine*, *1*(1), 6–43. doi: 10.1109/MGRS.2013.2248301

Nasirzadehdizaji, R., Sanli, F. B., Abdikan, S., Cakir, Z., Sekertekin, A., & Ustuner, M. (2019). Sensitivity analysis of multi-temporal Sentinel-1 SAR parameters to crop height and canopy coverage. *Applied Sciences (Switzerland)*, *9*(4). doi: 10.3390/app9040655

Natuur en milieu federatie. (n.d.). *Bodembedekking met groenbemesters en mulch - Natuurinclusieve Landbouw*. Retrieved from https://www.landbouwmetnatuur.nl/maatregelen/groenbemesters-vanggewassen/

Oliver, C., & Quegan, S. (2004). *Understanding synthetic aperture radar images*. SciTech Publishing.

O'neill, R. V., Krummel, J. R., Gardner, R. H., Sugihara, G., Jackson, B., Deangelis, D. L., ... Graham, R. L. (1988). *Indices of landscape pattern* (Vol. 1; Tech. Rep. No. 3).

Onojeghuo, A. O., Blackburn, G. A., Wang, Q., Atkinson, P. M., Kindred, D., & Miao, Y. (2018, 9). Rice crop phenology mapping at high spatial and temporal resolution using downscaled MODIS time-series. *https://doi-org.tudelft.idm.oclc.org/10.1080/15481603.2018.1423725*, *55*(5), 659–677. Retrieved from https://www-tandfonline-com.tudelft.idm.oclc.org/doi/abs/10.1080/15481603.2018.1423725 doi: 10.1080/15481603.2018.1423725

Ottinger, M., & Kuenzer, C. (2020). Spaceborne L-Band synthetic Aperture Radar Data for geoscientific analyses in coastal land applications: A review. *Remote Sensing*, *12*(14). doi: 10.3390/rs12142228

Paris, J. F. (1983). Radar Backscattering Properties of Corn And Soybeans at Frequencies of 1.6, 4.75, And 13.3 GHz. *IEEE Geoscience and Remote Sensing Magazine*, *21*(3), 392–400. doi: 10.1109/TGRS.1983.350472

Park, J. W., Won, J. S., Korosov, A. A., Babiker, M., & Miranda, N. (2019). Textural noise correction for sentinel-1 TOPSAR cross-polarization channel images. *IEEE Transactions on Geoscience and Remote Sensing*, *57*(6), 4040–4049. doi: 10.1109/TGRS.2018.2889381

Parresol, B. R., & Edwards, L. A. (2014). An entropy-based contagion index and its sampling properties for landscape analysis. *Entropy*, *16*(4), 1842–1859. doi: 10.3390/e16041842

Pastor-Guzman, J., Atkinson, P. M., Dash, J., & Rioja-Nieto, R. (2015, 11). Spatiotemporal Variation in Mangrove Chlorophyll Concentration Using Landsat 8. *Remote Sensing 2015, Vol. 7, Pages 14530-14558*, *7*(11), 14530–14558. Retrieved from https://www.mdpi.com/2072-4292/7/11/14530/htmhttps://www.mdpi.com/2072-4292/7/11/14530 doi: 10.3390/RS71114530

Patel, P., Srivastava, H. S., Panigrahy, S., Singh Parihar, J., Srivastava, H. S., Panigrahy, S., & Singh Parihar, J. (2007). Comparative evaluation of the sensitivity of multi-polarized multi-frequency SAR backscatter to plant density. *International Journal of Remote Sensing*, *27*(2), 293–305. Retrieved from https://www.tandfonline.com/action/journalInformation?journalCode=tres20 doi: 10.1080/01431160500214050

Pedregosa, F., Michel, V., Grisel, O., Blondel, M., Prettenhofer, P., Weiss, R., ... Duchesnay, (2011). Scikit-learn: Machine Learning in Python. *Journal of Machine Learning Research*, *12*(85), 2825–2830. Retrieved from http://jmlr.org/papers/v12/pedregosa11a.html

Petrovic, S. (2006). A Comparison Between the Silhouette Index and the Davies-Bouldin Index in Labelling IDS Clusters. In *11th nordic workshop on secure it-systems* (pp. 53–64). Retrieved from https://xp-dev.com/svn/b_frydrych.../silhuetteIndexRegulaStopu.pdf

Pettorelli, N., Vik, J. O., Mysterud, A., Gaillard, J. M., Tucker, C. J., & Stenseth, N. C. (2005, 9). Using the satellite-derived NDVI to assess ecological responses to environmental change. *Trends in Ecology & Evolution*, *20*(9), 503–510. doi: 10.1016/J.TREE.2005.05.011

Piantanida, R., Miranda, N., & Hajduch, G. (2017). MPC-S1: Thermal Denoising of Products Generated by the S-1 IPF. *S-1 Mission Performance Center*.

Planet Labs PBC. (2022, 2). *Planetary Variable Biomass Proxy*. Haarlem. Retrieved from https://docs.vandersat.com/data_products/biomass_proxy/specification.html

Podest, E., Pinto, N., & Fielding, E. (2017). *Introduction to Synthetic Aperture Radar*. Retrieved from https://appliedsciences.nasa.gov/introduction-synthetic-aperture-radar

Praktijkonderzoek, B., Postbus, V., & Lelystad, A. K. (1999). zomergerst. (87).

Qiu, F., Berglund, J., Jensen, J. R., Thakkar, P., & Ren, D. (2004). Speckle noise reduction in SAR imagery using a local adaptive median filter. *GIScience and Remote Sensing*, *41*(3), 244–266. doi: 10.2747/1548-1603.41.3.244

Rhee, J., Im, J., & Carbone, G. J. (2010, 12). Monitoring agricultural drought for arid and humid regions using multi-sensor remote sensing data. *Remote Sensing of Environment*, *114*(12), 2875–2887. doi: 10.1016/J.RSE.2010.07.005

Riitters, K. H., O'neill, R. V., Wickham, J. D., & Jones, K. B. (1996). *A note on contagion indices for landscape analysis* (Vol. 11; Tech. Rep. No. 4).

Rijksdienst voor Ondernemend Nederland. (2019). *Vanggewas na mais*. Retrieved from https://www.rvo.nl/onderwerpen/mest/vanggewas

Robert Cloude, S., & Pottier, E. (1997). *An Entropy Based Classification Scheme for Land Applications of Polarimetric SAR* (Vol. 35; Tech. Rep. No. 1).

Rossi, M., Niedrist, G., Asam, S., Tonon, G., Tomelleri, E., & Zebisch, M. (2019, 2). A Comparison of the Signal from Diverse Optical Sensors for Monitoring Alpine Grassland Dynamics. *Remote Sensing 2019, Vol. 11, Page 296*, *11*(3), 296. Retrieved from https://www.mdpi.com/2072-4292/11/3/296/htmhttps://www.mdpi.com/2072-4292/11/3/296 doi: 10.3390/RS11030296

Rouse, J. W., Haas, R. H., Schell, J. A., & Deering, D. W. (1974). Monitoring vegetation systems in the Great Plains with ERTS. In *Third earth resources technology satellite-1 symposium*. (pp. 48–62). NASA. Retrieved from https://ntrs.nasa.gov/citations/19740022614

Sánchez, N., González-Zamora, , Martínez-Fernández, J., Piles, M., & Pablos, M. (2018, 9). Integrated remote sensing approach to global agricultural drought monitoring. *Agricultural and Forest Meteorology*, *259*, 141–153. doi: 10.1016/J.AGRFORMET.2018.04.022

Schlund, M., & Erasmi, S. (2020, 9). Sentinel-1 time series data for monitoring the phenology of winter wheat. *Remote Sensing of Environment*, *246*. doi: 10.1016/j.rse.2020.111814

Senarathna, T. S. S., & Hemapala, K. T. M. U. (2020, 7). Optimized Adaptive Overcurrent Protection Using Hybridized Nature-Inspired Algorithm and Clustering in Microgrids. *Energies*, *13*(13). doi: 10.3390/EN13133324

Seo, B., Lee, J., Lee, K. D., Hong, S., & Kang, S. (2019). Improving remotely-sensed crop monitoring by NDVI-based crop phenology estimators for corn and soybeans in Iowa and Illinois, USA. *Field Crops Research*, *238*(October 2017), 113–128. doi: 10.1016/j.fcr.2019.03.015

Shang, J., Liu, J., Poncos, V., Geng, X., Qian, B., Chen, Q., ... Walters, D. (2020). Detection of crop seeding and harvest through analysis of time-series Sentinel-1 interferometric SAR data. *Remote Sensing*, *12*(10). doi: 10.3390/rs12101551

Shannon, C. E. (1948). A Mathematical Theory of Communication. *The Bell System Technical Journal*(3), 379–423. doi: 10.1002/J.1538-7305.1948.TB01338.X

Sibma, L. (1987). *Ontwikkeling en groei van mais (Zea mays L.) onder Nederlandse omstandigheden*.

Skriver, H., Svendsen, M. T., & Thomsen, A. G. (1999). *Multitemporal C- and L-band polarimetric signatures of crops* (Vol. 37; Tech. Rep. No. 5). doi: 10.1109/36.789639

Skrunes, S., Brekke, C., & Eltoft, T. (2014, 2). *A Comprehensive Analysis of Polarimetric Features for Oil Spill Characterization.* Tromso: University of Tromso. Retrieved from https://earth.esa.int/eogateway/documents/20142/37627/6-Comprehensive_analysis_polarimetric.pdf

Smith, D. M., & Smitht, D. M. (1996). Speckle reduction and segmentation of Synthetic Aperture Radar images. *International Journal of Remote Sensing*, *17*(11), 2043–2057. Retrieved from https://www.tandfonline.com/action/journalInformation?journalCode=tres20 doi: 10.1080/01431169608948758

Steele-Dunne, S. C., Friesen, J., & Van De Giesen, N. (2012). Using diurnal variation in backscatter to detect vegetation water stress. *IEEE Transactions on Geoscience and Remote Sensing*, *50*(7 PART1), 2618–2629. doi: 10.1109/TGRS.2012.2194156

Steele-Dunne, S. C., McNairn, H., Monsivais-Huertero, A., Judge, J., Liu, P. W., & Papathanassiou, K. (2017, 5). *Radar Remote Sensing of Agricultural Canopies: A Review* (Vol. 10) (No. 5). Institute of Electrical and Electronics Engineers. doi: 10.1109/JSTARS.2016.2639043

Stokkermans, P. (2019a, 11). *De laatste mais op rupsbanden binnengehaald - Nieuwe Oogst.* Retrieved from https://www.nieuweoogst.nl/nieuws/2019/11/18/de-laatste-mais-op-rupsbanden-binnengehaald

Stokkermans, P. (2019b, 10). *Mais nog lang niet altijd rijp - Nieuwe Oogst.* Retrieved from https://www.nieuweoogst.nl/nieuws/2019/10/01/mais-nog-lang-niet-altijd-rijp

Susan Moran, M., Alonso, L., Moreno, J. F., Pilar Cendrero Mateo, M., Fernando de la Cruz, D., Montoro, A., … Montoro, A. (2012). A RADARSAT-2 Quad-Polarized Time Series for Monitoring Crop and Soil Conditions in Barrax, Spain. *IEEE TRANSACTIONS ON GEOSCIENCE AND REMOTE SENSING*, *50*(4). Retrieved from http://ieeexplore.ieee.org. doi: 10.1109/TGRS.2011.2166080

Tan, S., Wu, B., Yan, N., & Zeng, H. (2018). Satellite-Based Water Consumption Dynamics Monitoring in an Extremely Arid Area. Retrieved from www.mdpi.com/journal/remotesensing doi: 10.3390/rs10091399

Tarpley, J. D., Schneider, S. R., & Money, R. L. (1984). American Meteorological Society Global Vegetation Indices from the NOAA-7 Meteorological Satellite. *Source: Journal of Climate and Applied Meteorology*, *23*(3), 491–494.

Thomason, W. E., Phillips, S. B., & Raymond, F. D. (2007, 8). Defining useful limits for spectral reflectance measures in corn. *Journal of Plant Nutrition*, *30*(8), 1263–1277. doi: 10.1080/01904160701555176

Tian, J., Wang, L., Li, X., Gong, H., Shi, C., Zhong, R., & Liu, X. (2017, 9). Comparison of UAV and WorldView-2 imagery for mapping leaf area index of mangrove forest. *International Journal of Applied Earth Observation and Geoinformation*, *61*, 22–31. doi: 10.1016/J.JAG.2017.05.002

Tilman, D., Balzer, C., Hill, J., & Befort, B. L. (2011, 12). Global food demand and the sustainable intensification of agriculture. *Proceedings of the National Academy of Sciences of the United States of America*, *108*(50), 20260–20264. Retrieved from https://www-pnas-org.tudelft.idm.oclc.org/doi/abs/10.1073/pnas.1116437108 doi: 10.1073/PNAS.1116437108/SUPPL{_}FILE/PNAS.201116437SI.PDF

Tuceryan, M., & Jain, A. K. (1993). Texture Analysis. In C. H. Chen, L. F. Pau, & P. S. P. Wang (Eds.), *Handbook of pattern recognition and computer vision* (pp. 235–276). World Scientific Publishing Company.

Ulaby, F. T. (1980). Vegetation Clutter Model. *IEEE Transactions on Antennas and Propagation*, *28*(4), 538–545. doi: 10.1109/TAP.1980.1142377

Ulaby, F. T., Dobson, M. C., & Alvarez-Perez, J. L. (2019). *Handbook of radar scattering statistics for terrain.* Norwood, MA :: Artech House,.

Ulaby, F. T., & El-Rayes, M. A. (1987). Microwave Dielectric Spectrum of Vegetation—Part II: Dual-Dispersion Model. *IEEE Transactions on Geoscience and Remote Sensing*, *GE-25*(5), 550–557. doi: 10.1109/TGRS.1987.289833

Ulsig, L., Nichol, C. J., Huemmrich, K. F., Landis, D. R., Middleton, E. M., Lyapustin, A. I., ... Thenkabail, P. S. (2017). Detecting Inter-Annual Variations in the Phenology of Evergreen Conifers Using Long-Term MODIS Vegetation Index Time Series. *Remote Sensing*, *9*, 49. Retrieved from www.mdpi.com/journal/remotesensing doi: 10.3390/rs9010049

Valero, S., Arnaud, L., Planells, M., & Ceschia, E. (2021). Synergy of Sentinel-1 and Sentinel-2 Imagery for Early Seasonal Agricultural Crop Mapping. *Remote Sensing*, *13*(4891). Retrieved from https://doi.org/10.3390/rs13234891 doi: 10.3390/rs13234891

van der Wal, T., Abma, B., Viguria, A., Prévinaire, E., Zarco-Tejada, P. J., Serruys, P., ... van der Voet, P. (2013). Fieldcopter: unmanned aerial systems for crop monitoring services. , 169–175. Retrieved from https://link.springer.com/chapter/10.3920/978-90-8686-778-3_19 doi: 10.3920/978-90-8686-778-3{_}19

Van Griethuysen, J. J. M., Fedorov, A., Parmar, C., Hosny, A., Aucoin, N., Narayan, V., ... Aerts, H. J. W. L. (2017). Focus on Computer Resources Computational Radiomics System to Decode the Radiographic Phenotype. *Cancer Research*, *77*(21), 104–107. Retrieved from http://cancerres.aacrjournals.org/ doi: 10.1158/0008-5472.CAN-17-0339

Veloso, A., Mermoz, S., Bouvet, A., Le Toan, T., Planells, M., Dejoux, J. F., & Ceschia, E. (2017, 9). Understanding the temporal behavior of crops using Sentinel-1 and Sentinel-2-like data for agricultural applications. *Remote Sensing of Environment*, *199*, 415–426. doi: 10.1016/j.rse.2017.07.015

Vicente-Guijalba, F., Martinez-Marin, T., & Lopez-Sanchez, J. M. (2015). Dynamical approach for real-time monitoring of agricultural crops. *IEEE Transactions on Geoscience and Remote Sensing*, *53*(6), 3278–3293. doi: 10.1109/TGRS.2014.2372897

Vicente-Serrano, S. M., Camarero, J. J., Olano, J. M., Martín-Hernández, N., Peña-Gallardo, M., Tomás-Burguera, M., ... El Kenawy, A. (2016, 12). Diverse relationships between forest growth and the Normalized Difference Vegetation Index at a global scale. *Remote Sensing of Environment*, *187*, 14–29. doi: 10.1016/J.RSE.2016.10.001

Virtanen, P., Gommers, R., Oliphant, T. E., Haberland, M., Reddy, T., Cournapeau, D., ... Vázquez-Baeza, Y. (2020, 2). SciPy 1.0: fundamental algorithms for scientific computing in Python. *Nature Methods 2020 17:3*, *17*(3), 261–272. Retrieved from https://www-nature-com.tudelft.idm.oclc.org/articles/s41592-019-0686-2 doi: 10.1038/S41592-019-0686-2

Vreugdenhil, M., Navacchi, C., Bauer-Marschallinger, B., Hahn, S., Steele-Dunne, S., Pfeil, I., ... Wagner, W. (2020, 10). Sentinel-1 Cross Ratio and Vegetation Optical Depth: A Comparison over Europe. *Remote Sensing*, *12*(20). Retrieved from www.mdpi.com/journal/remotesensing doi: 10.3390/rs12203404

Vreugdenhil, M., Wagner, W., Bauer-Marschallinger, B., Pfeil, I., Teubner, I., Rüdiger, C., & Strauss, P. (2018, 9). Sensitivity of Sentinel-1 backscatter to vegetation dynamics: An Austrian case study. *Remote Sensing*, *10*(9). doi: 10.3390/rs10091396

Wang, Z., Jensen, J. R., & Im, J. (2010, 10). An automatic region-based image segmentation algorithm for remote sensing applications. *Environmental Modelling and Software*, *25*(10), 1149–1165. doi: 10.1016/j.envsoft.2010.03.019

Wirth, M. (2004). *Texture analysis.* University of Guelph, Computing and Information Science.

Wiseman, G., McNairn, H., Homayouni, S., & Shang, J. (2014). RADARSAT-2 Polarimetric SAR response to crop biomass for agricultural production monitoring. *IEEE Journal of Selected Topics in Applied Earth Observations and Remote Sensing*, *7*(11), 4461–4471. doi: 10.1109/JSTARS.2014.2322311

Xue, L., Li, G., Xia, Linzhang, Q. •, Y., Zhang, H., … Zhang, H. (2014). Topdressing nitrogen recommendation for early rice with an active sensor in south China. *Precision Agric*, *15*, 95–110. doi: 10.1007/s11119-013-9326-5

Zhao, W., Qu, Y., Chen, J., & Yuan, Z. (2020). Deeply synergistic optical and SAR time series for crop dynamic monitoring. *Remote Sensing of Environment*, *247*(111952). Retrieved from https://doi.org/10.1016/j.rse.2020.111952 doi: 10.1016/j.rse.2020.111952

Zhu, Y., Zhao, C., Yang, H., Yang, G., Han, L., Li, Z., … Lei, L. (2019). Estimation of maize above-ground biomass based on stem-leaf separation strategy integrated with LiDAR and optical remote sensing data. *PeerJ*. doi: 10.7717/peerj.7593

A

Crop Development

In order to interpret the remote sensing images of the specified crops, a general understanding of crop development is indispensable. The crop and crop growth stage definitions of BBA et al. (2001) will be used for this research. Of the four selected crops: maize, barley, oat and wheat, the latter three are grouped together and thus follow the same phenological growth stages and BBCH-identification keys. Below is a brief description of the principal growing stages of maize and cereals. Note that the principal growing stages are not always a contiguous sequence because of the definitions BBA et al. (2001) used.

A.0.1. Maize growing stages

The growing season of maize (*Zea mays L.*) is divided into seven principal growing stages. The first principal growing stage is germination and describes the period from the dry seed (BBCH 00) to the emergence (BBCH 09). Principal growing stage 1 is the leaf development stage, where each stage (BBCH 10-19) describes the development of a new leaf. Next, stage 3 (BBCH 30-39) describes the stem elongation and node development of the plants. This stage drastically changes the structure of the plant, creating a strong vertical component. As mentioned, not all principal growing stages are sequential, and for maize, stage 4 is undefined in the BBCH model. Stage 5 is the heading stage and describes the period from the beginning of the tassel emergence (BBCH 51) until the tassel fully emerged and separated (BBCH 59). Next, stage 6 describes the flowering of the male and female plants. The male plants shed pollen, and in the female plant, the stigmata become visible (BBCH 63). The stage ends with flowering for the male plants and drying of the stigmata for the female plants (BBCH 69). Principal stage 7 describes the fruit development from the beginning of grain development (BBCH 71) to the stage where nearly all kernels have reached their final size (BBCH 79). Stage 8 is the ripening stage, where the dry mass of the kernels increases from about 45% (BBCH 81) to 65% (BBCH 89). Finally, stage 9 is senescence, in which the plant dies, collapses (BBCH 97), and is harvested (BBCH 99). The different phases are shown in Figure A.1.

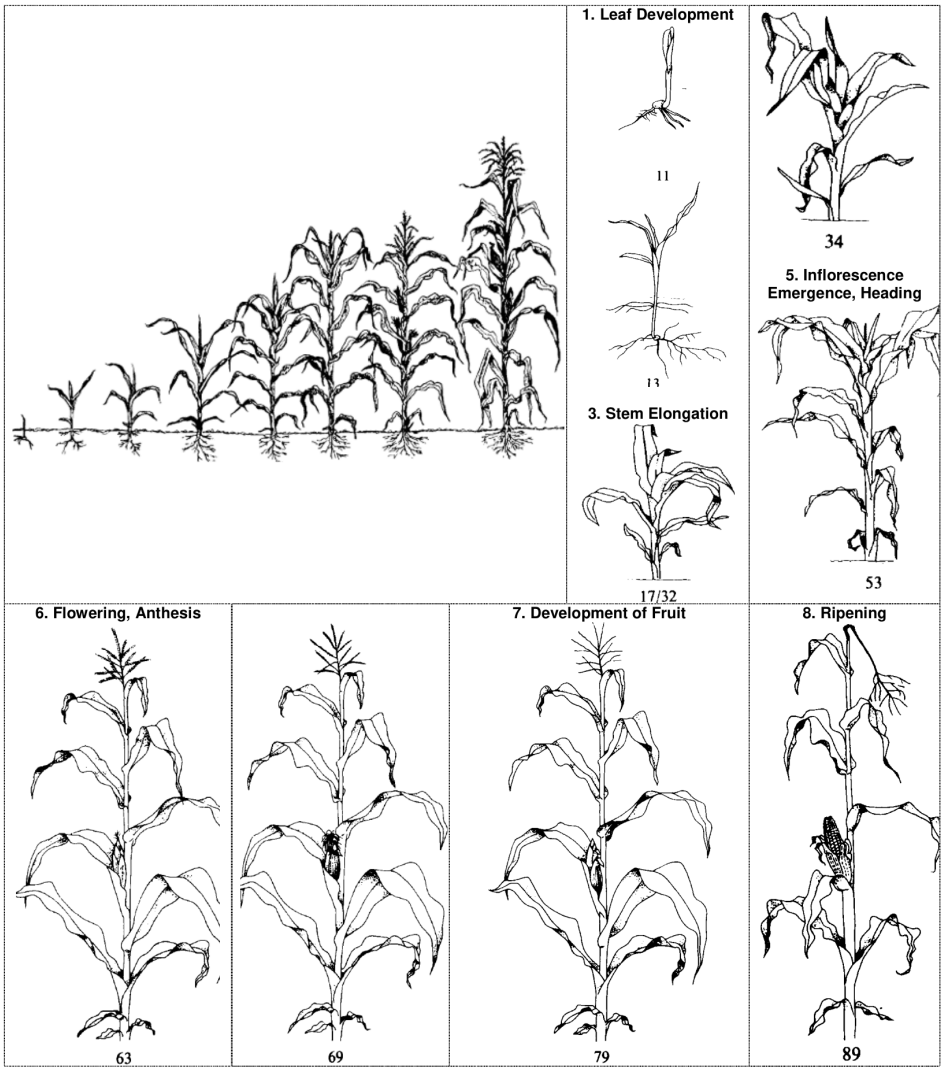

Figure A.1: Growing stages of maize as defined by BBA et al. (2001).

A.0.2. Cereal growing stages

Many growing stages of the different cereals (wheat = *Triticum sp. L.*, barley = *Hordeum vulgare L.*, oat = *Avena sativa L.*) are somewhat similar to those of maize. The cereals also start with germination (stage 0) and leaf development (stage 1). The next stage, however, is principal growing stage 2, which describes the process of tillering from no tillers (BBCH 20) to the maximum amount of detectable tillers (BBCH 29). Stage 3 is also stem elongation but is defined differently for cereals. The first stages correspond to certain heights of the first node above the tillering node (BBCH 31-36), and the last stages correspond to the emergence of the flag leaf (BBCH 37& 39), where the flag leaf is defined as the first leaf below the inflorescence (or the last leaf to emerge). Next, stage 4 is the booting stage. BBCH 41-47 describe the development of the flag leaf sheath until its opening (BBCH 47) and the visibility of the first awns (BBCH 49). Stage 5 is again the heading stage, where each BBCH key indicates a 10% increase in the inflorescence emergence from the sheath. During stage 6, flowering occurs. It starts with the first anthers becoming visible (BBCH 61) and ends with all spikelets having completed flowering. The last stages are all part of the maturing of the plants, during which the kernels harden and moisture decreases. The first step in this maturing process is the milking stage (BBCH 71-77), where the grains grow their final size but are still very soft. Then, in stage 8, the ripening occurs. The kernels go from soft dough (BBCH 85) to hard dough (BBCH 87) to fully ripe (BBCH 89). Finally, the senescence is described by stage 9, where the grains loosen (BBCH 93), the plant dies and collapses (BBCH 97) and is harvested (BBCH 99). The growing stages are illustrated in Figure A.2a.

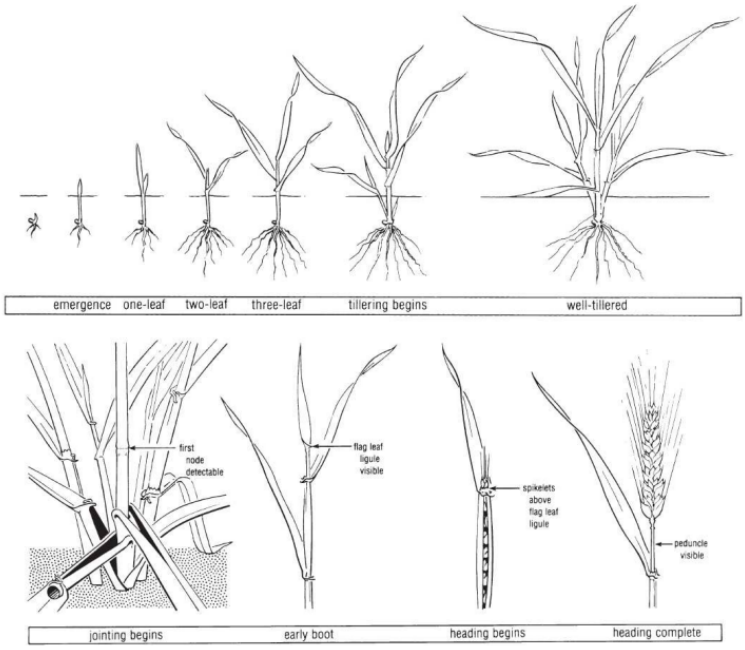

(a) BBCH growing stages of cereals (wheat, barley, oat) (Earth Observation Research Branch Team, 2011)

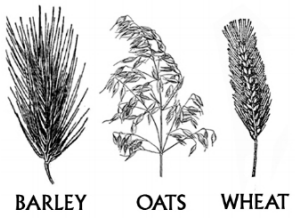

(b) Differences between the ears of the studied cereal types (wheat, barley and oat) (Lakna, 2019).

A more comprehensive description of the growing stages, supported by field images, can be found in Earth Observation Research Branch Team (2011). The main difference between barley, wheat and oats is that barley and wheat are cereal grasses grown as primary crops, whereas oats are a secondary crop derived from a weed of primary cereal grasses (such as wheat and barley). Furthermore, barley grains are arranged in a spike, whereas oats grow as small florets (Lacorn, Weiss, Wehling, Arlinghaus, & Scherf, 2019). The differences are visualized in Figure A.2b.

B

Entropy Concept Examples

To illustrate the effect of different *probability mass functions* (pmfs) and spatial distributions on the types of entropy, biomass data was simulated and entropies were computed. The results are presented in Figure B.1 to Figure B.4.

Figure B.1 shows the effect of spatial distribution of the biomass values. Since the pmf of the biomass data us uniform, the Shannon entropy is the same for each of the three scenarios. Furthermore, the Altieri entropy is affected more strongly by the spatial configuration: it demonstrates a decrease of 0.607 vs a decrease of 0.269 of the Leibovici entropy.

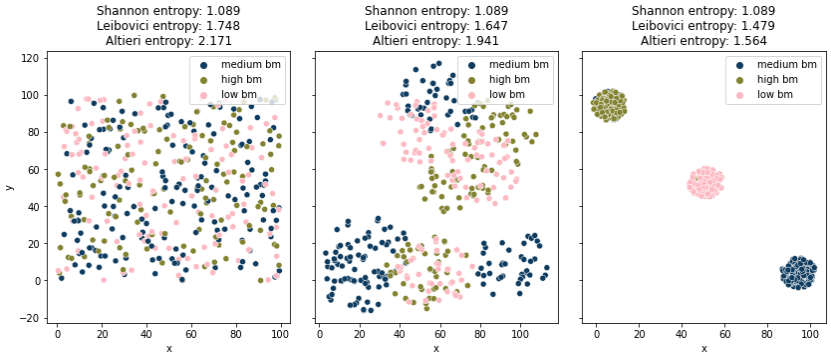

Figure B.1: Shannon, Leibovici and Altieri entropy for uniform pmf and random, slightly clustered, and strongly clustered biomass values.

The Altieri and Leibovici entropy are intuitive to interpret here: if similar values are isolated clusters, one would expect a value at a certain location, thus making it *unsurprising* (i.e. it has a low information content). However, in some cases an increase in Altieri and Leibovici entropy between the second and third scenario can be observed. Figure B.2 demonstrates this is due to the strong increase in mutual information (MI). The proportional MI (MI_{prop}) increases significantly and the total entropy increases again.

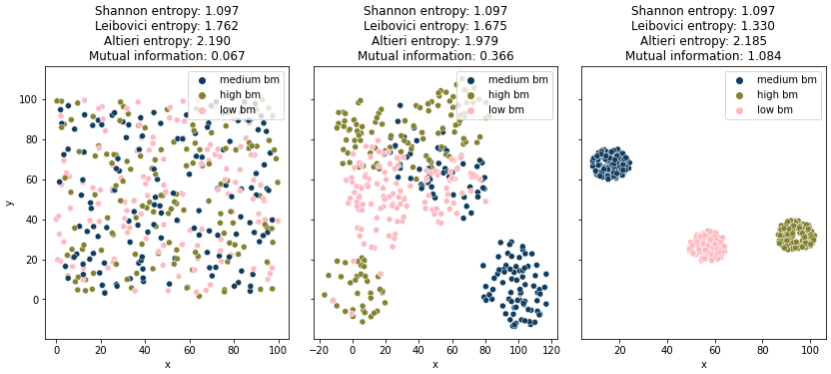

Figure B.2: Increase in Altieri entropy for uniform pmf and random, slightly clustered, and strongly clustered biomass values.

Besides spatial distribution, the entropies are influenced by the pmf. Figure B.3 shows the effect of varying the pmf while maintaining the same (random) spatial distribution. A significant decrease in all entropies can be observed, since each data point will contain less information when the probability of the points belonging to the same class is high. Note that even though the coordinates of the data points did not change, spatial distribution does play a role: the number of co-occurrences is much higher in the second and third scenario, thereby increasing the MI.

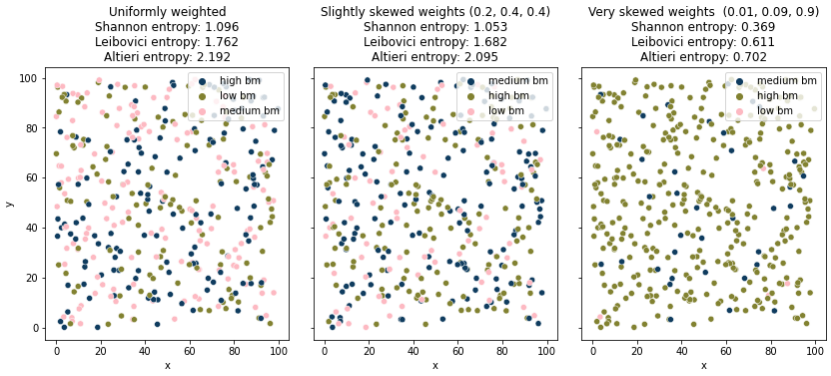

Figure B.3: Shannon, Leibovici and Altieri entropy for random spatial distribution and uniform, slightly skewed, and very skewed weights. Note that the scalars corresponding to the weights are ordered as (low bm, medium bm, high bm).

Lastly, the effect of the number of classes is evaluated in Figure B.4. As expected, the entropy increases with an increase in the number of classes: there is less certainty to which class a data point will belong if there are more classes. This corresponds to the mathematical definition of entropy, where $\log(I)$ (with I the amount of classes) equals the maximum entropy.

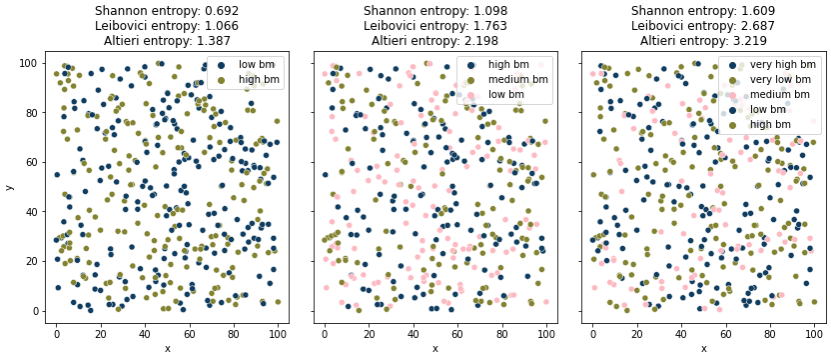

Figure B.4: Shannon, Leibovici and Altieri entropy for random spatial distribution and uniform weights, but with a different number of classes.

C

K-means Clustering

A clearly recognizable characteristic of radar data is the 'radar pattern', e.g. see S1 index raster in Figure 2.8b. These patterns often consist of multiple *clusters*, i.e. areas with similar backscatter values. To quantify such a pattern, one must analyse where objects with similar spectrum values are clustered together without any previous knowledge. K-means clustering is an unsupervised classification algorithm, which has become one of the most common methods of data analysis, as in the fields of pattern recognition, image processing, remote sensing and many more (Lv et al., 2010).
K-means clustering is a partitional clustering algorithm, which implies that data objects are divided into non-overlapping groups. The algorithm is non-deterministic, which means that even if two distinct runs were based on identical input data, the outputs might still vary (Al-Doski, Mansor, & Shafri, 2013). Lv et al. (2010) discusses the algorithm's strengths and weaknesses, including their scalability and ability to detect spherical shapes as strengths and their inability to detect complex shapes and density differences as weaknesses.

The algorithm is relatively simple and can be described in a few steps, which are also visualised in Figure C.1. First, it requires the user the specify two parameters: 1) the number of clusters (k), and 2) the maximum number of iterations (m) (Wang, Jensen, & Im, 2010). The number of clusters can either be chosen based on prior knowledge of the data set, e.g. a classification problem with a fixed number of classes or based on a method to find the optimum number of clusters. Several methods are available, and three commonly used examples are given below.

1. **The elbow (curve) method** - method based on defining clusters such that the total within-cluster sum of square (WSS) is minimised. Optimal k is when adding another cluster does not improve the WSS much (Cui, 2020).

2. **The silhouette score** - method using mean of intra-cluster distance (a) and the mean of nearest-cluster distance (b) for each sample, such that the score is defined as $(a-b)/max(a,b)$. The optimal k corresponds to the maximum silhouette score (Aranganayagi & Thangavel, 2007).

3. **The Davies Bouldin (DB) index** - a ratio of intra-cluster distance and inter-cluster distances. Therefore a minimal DB index is desired for the optimal k (Petrovic, 2006).

Since the algorithm is relatively cheap and very fast, limiting the number of observations is often unnecessary. Broder, Garcia-Pueyo, Josifovski, Vassilvitskii, and Venkatesan (2014) found that K-means converges between 20 to 50 iterations for all practical applications.
The next step in the algorithm is to determine the centroid locations. For the first iteration, this is done randomly. All data points are then allocated to the closest centroid by a certain distance metric, such as Euclidean distance. Next, the average distance of the data points to the cluster centroid is computed. If the cluster centres do not change or the maximum number of iterations is reached, a raster with cluster labels is returned. Otherwise, the updated centre locations are defined as centroids, and the algorithm starts over again (Wang et al., 2010).

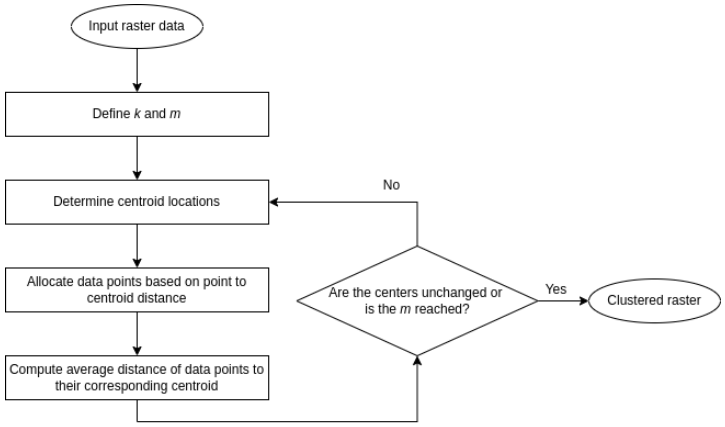

Figure C.1: Flow chart of K-means algorithm, adjusted figure from Senarathna and Hemapala (2020).

D

Field Thresholds

Figure D.1 illustrates the reason for the filtering of fields that are only covered by (part of) one orbit, causing outliers in the mean time series. The relative orbits of each observation is marked in the time series by one of the four symbols. Comparing Figure D.1a with Figure D.1b, it can be seen that the outliers are caused by a single orbit, and that, after applying the requirement that at least 10% of the fields should have an observation, these observations are filtered. If this threshold is increased to 20%, as was done in Figure D.1c, no other strong peaks are filtered, indicating an agreement between the fields of other values.

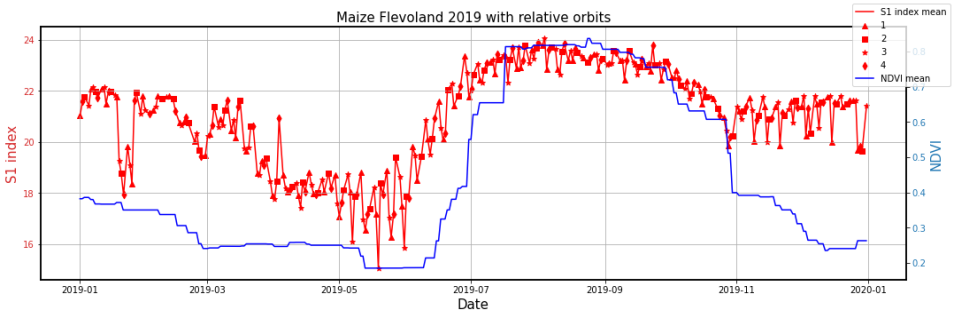

(a) $t_f = 0\%$

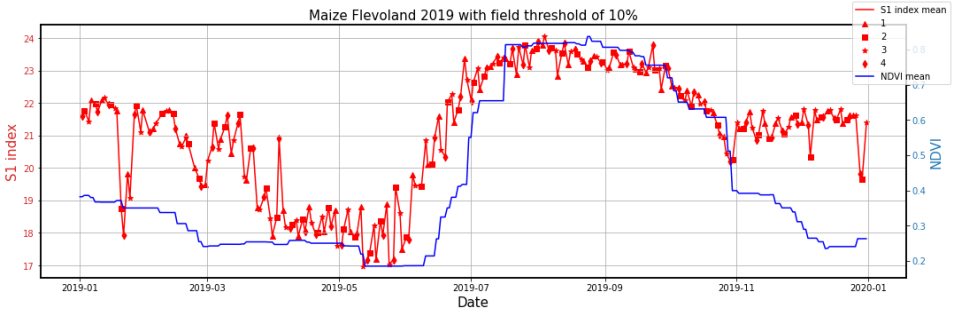

(b) $t_f = 10\%$

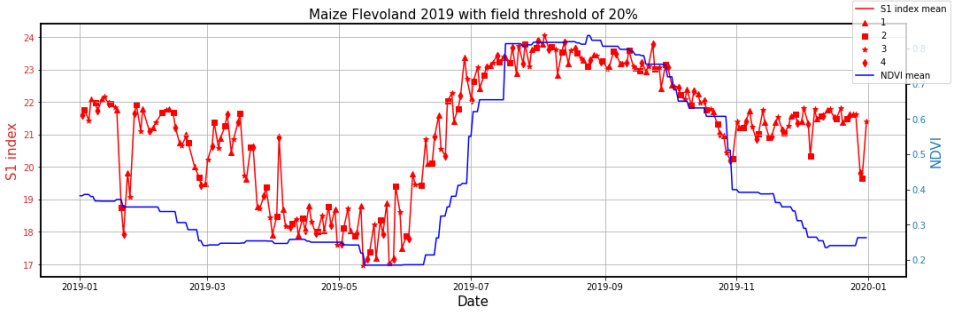

(c) $t_f = 20\%$

Figure D.1: Example of maize fields for to filter fields that are not covered entirely, filtering based on the relative amount of fields available with the *field threshold* (t_f).

E

Field Selection

As discussed in Section 3.1, for each crop a field was selected with the smallest RMS from the mean of the fields. Figure E.1 illustrates how the selected fields compare to the mean and the other fields.

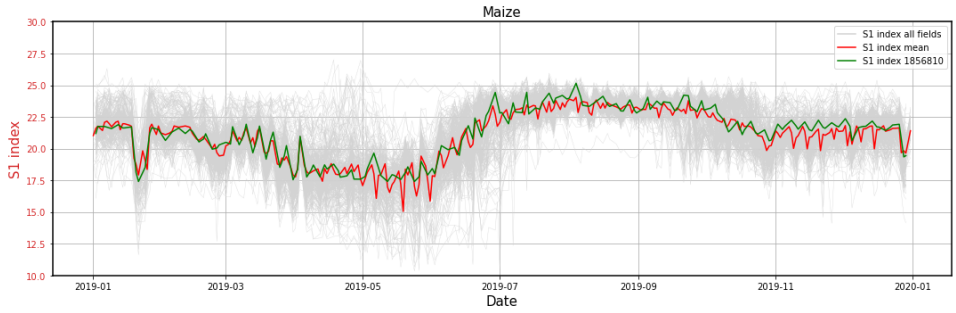

(a)

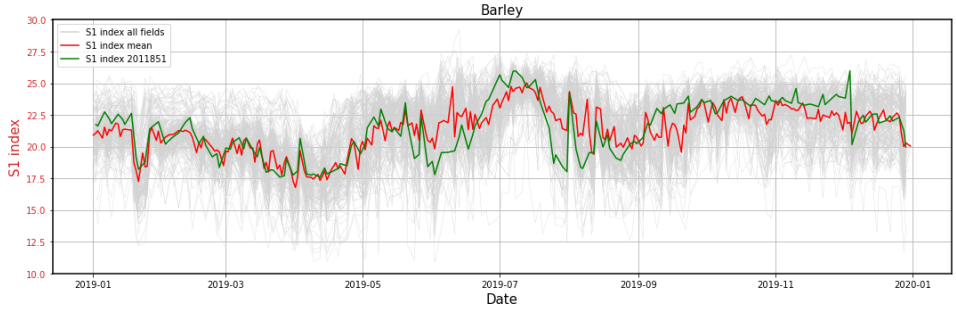

(b)

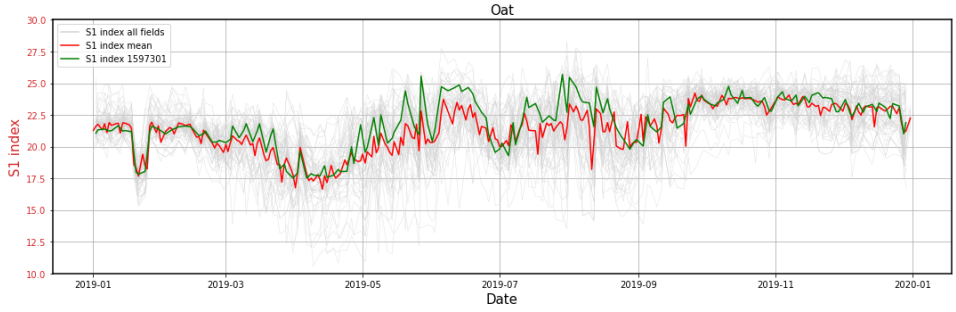

(c)

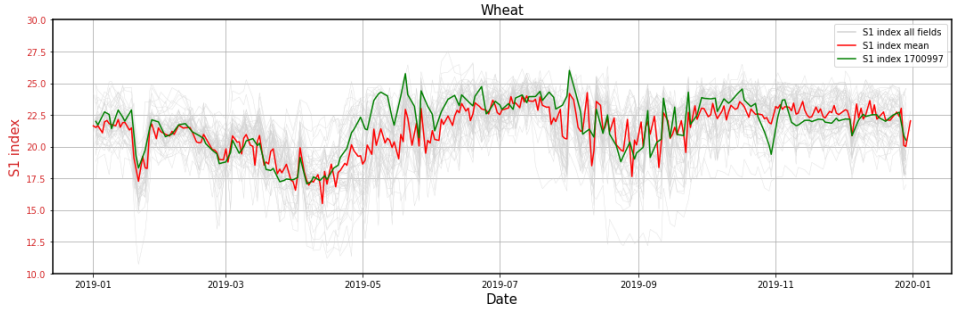

(d)

Figure E.1: Selected fields for (a) maize, (b) barley, (c) oat, and (d) wheat. The selected fields (green) are based on minimal root mean square difference between the fields and the mean (red). The other fields are plotted in light grey to demonstrate the variability.

F

Metric Analysis Cereals

As described in Section 4.2.1, the metric analysis performed is mainly based on image processing, and is assumed not to be crop dependent. However, for completeness and avoiding drawing conclusions on a single field, the plots were also created for the other crops. The following sections are structured the same way as Section 4.2.1, but show the respective plots for each of the cereals (barley, oat and wheat). Furthermore, Appendix F.4 visualises the differences in computation time of the metrics.

F.1. S1 index change effects

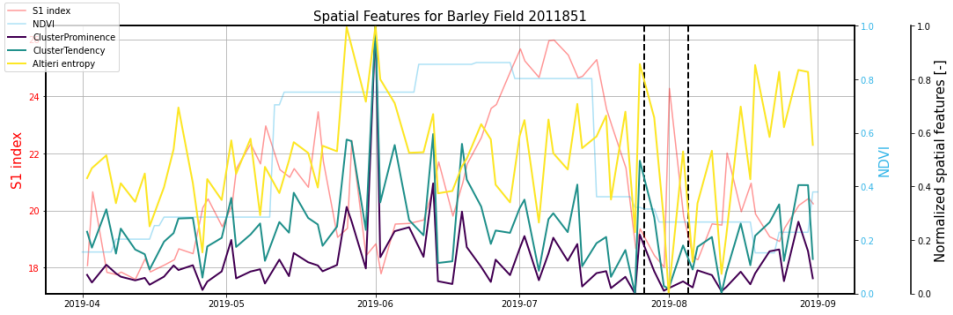

(a) Time series of spatial metrics with the period of interest denoted by the dashed vertical black lines.

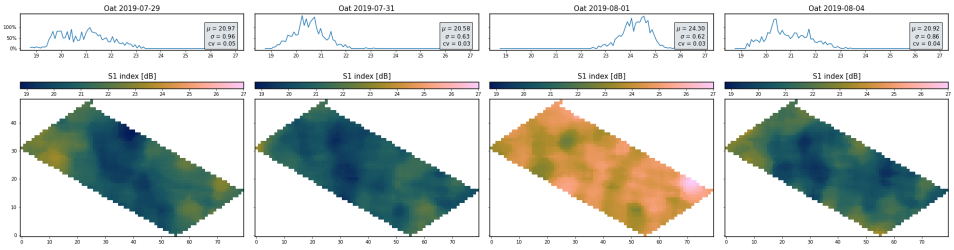

(b) S1 index rasters during period of interest.

Figure F.1: Effect of sudden change in S1 index on spatial metrics of a barley field in (a) time, and (b) space.

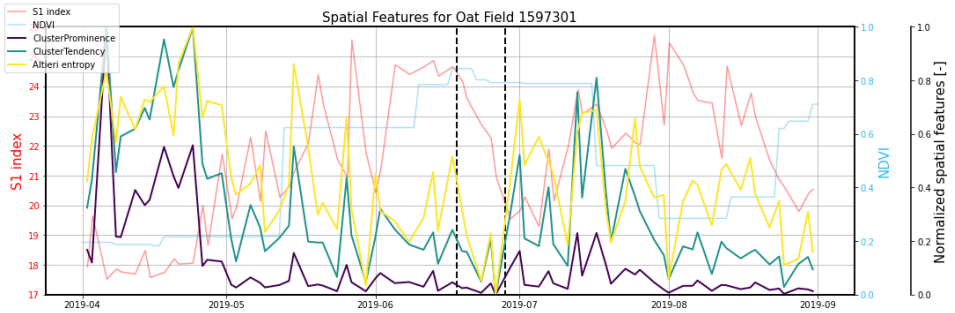

(a) Time series of spatial metrics with the period of interest denoted by the dashed vertical black lines.

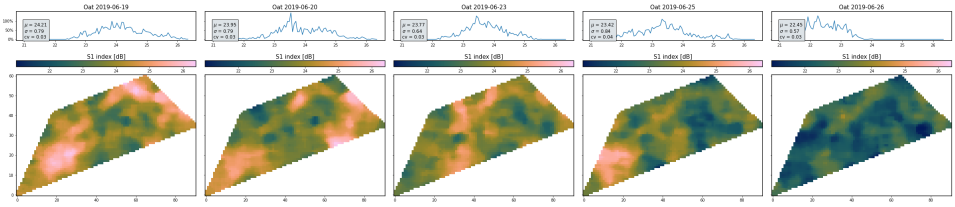

(b) S1 index rasters during period of interest.

Figure F.2: Effect of sudden change in S1 index on spatial metrics of a oat field in (a) time, and (b) space.

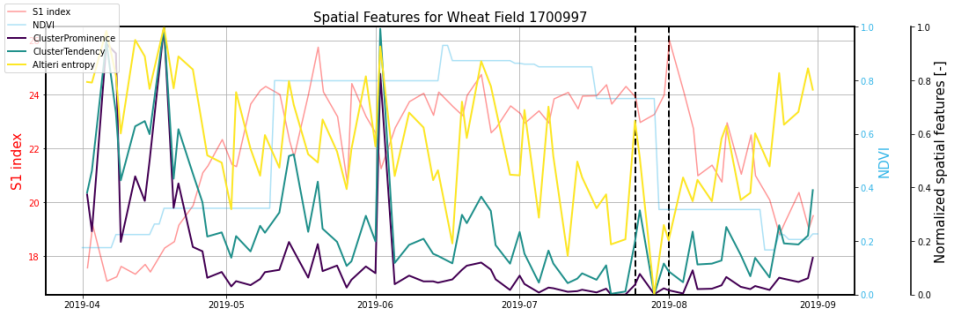

(a) Time series of spatial metrics with the period of interest denoted by the dashed vertical black lines.

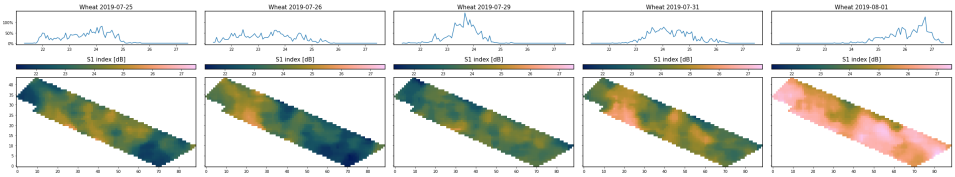

(b) S1 index rasters during period of interest.

Figure F.3: Effect of sudden change in S1 index on spatial metrics of a wheat field in (a) time, and (b) space.

F.2. Metric similarities

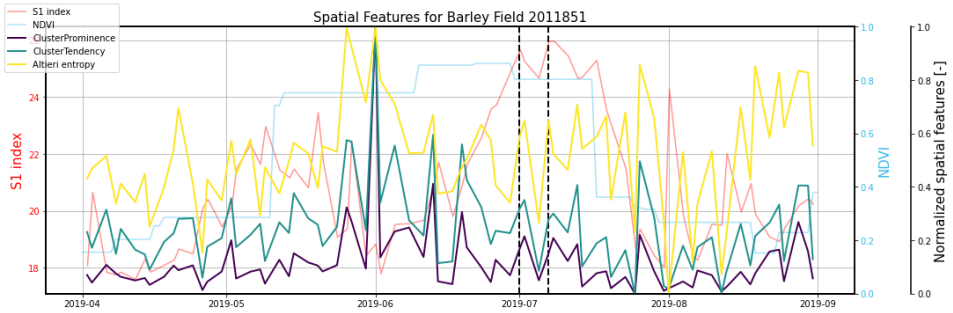

(a) Time series of spatial metrics with the period of interest denoted by the dashed vertical black lines.

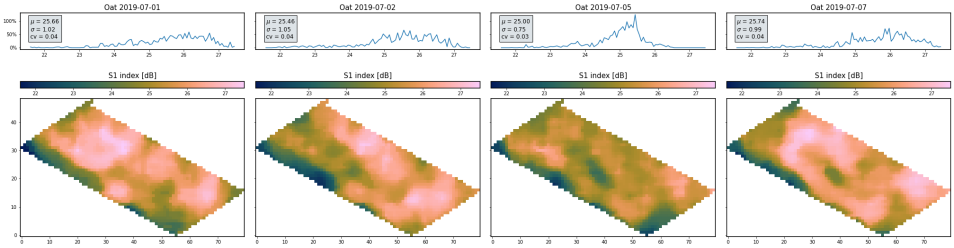

(b) S1 index rasters during period of interest.

Figure F.4: Period of similar spatial metric values of barley in (a) time, and (b) space.

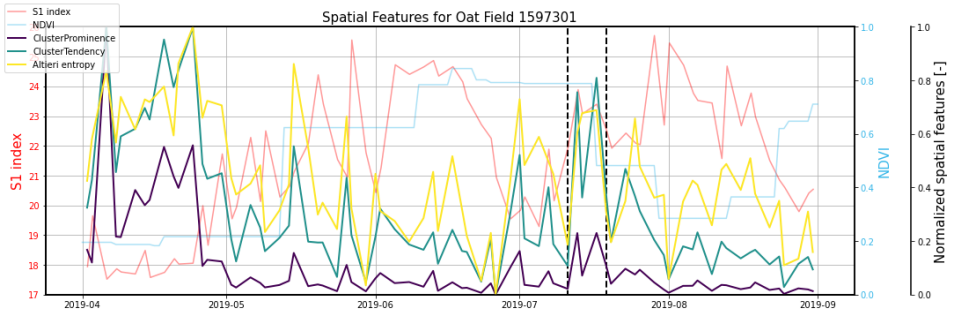

(a) Time series of spatial metrics with the period of interest denoted by the dashed vertical black lines.

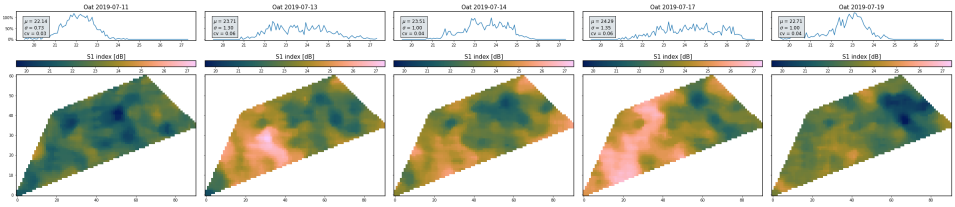

(b) S1 index rasters during period of interest.

Figure F.5: Period of similar spatial metric values of oat in (a) time, and (b) space.

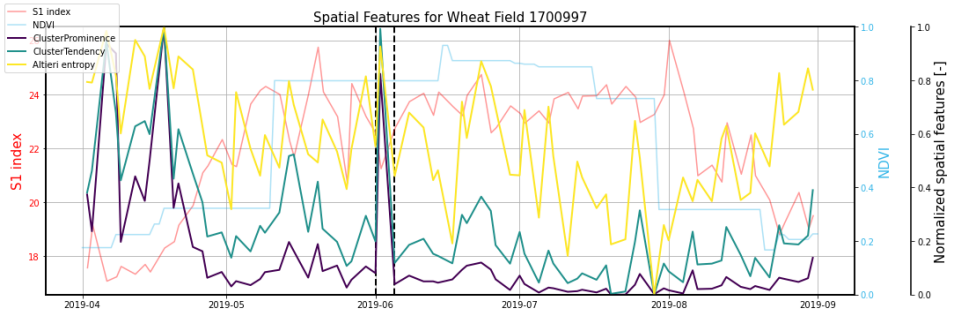

(a) Time series of spatial metrics with the period of interest denoted by the dashed vertical black lines.

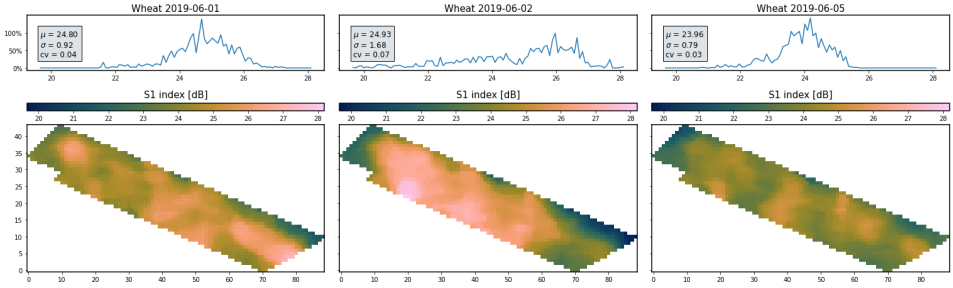

(b) S1 index rasters during period of interest.

Figure F.6: Period of similar spatial metric values of wheat in (a) time, and (b) space.

F.3. Metric differences

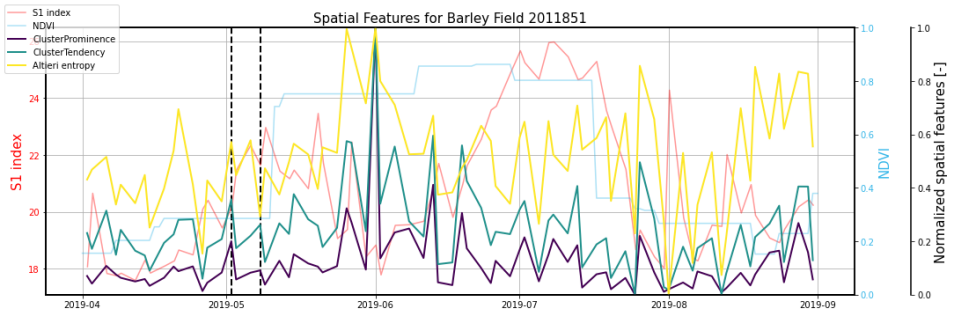

(a) Time series of spatial metrics with the period of interest denoted by the dashed vertical black lines.

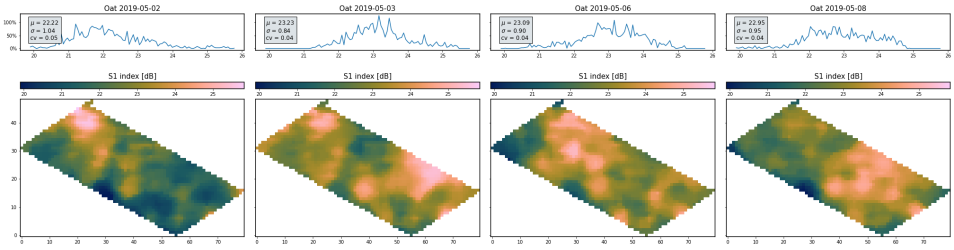

(b) S1 index rasters during period of interest.

Figure F.7: Period of dissimilar spatial metric values of barley in (a) time, and (b) space.

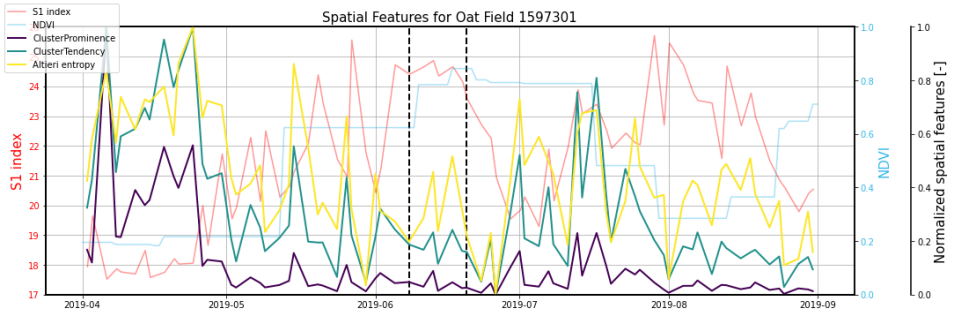

(a) Time series of spatial metrics with the period of interest denoted by the dashed vertical black lines.

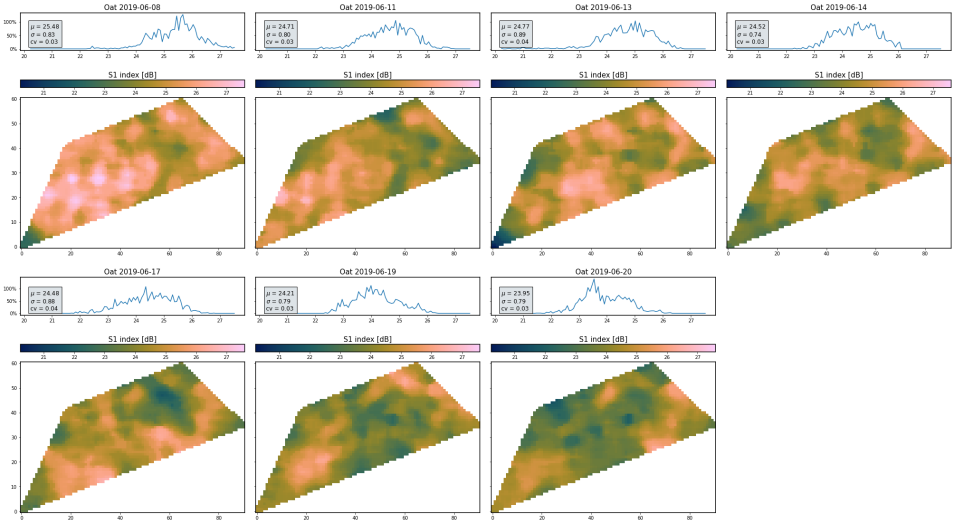

(b) S1 index rasters during period of interest.

Figure F.8: Period of dissimilar spatial metric values of oat in (a) time, and (b) space.

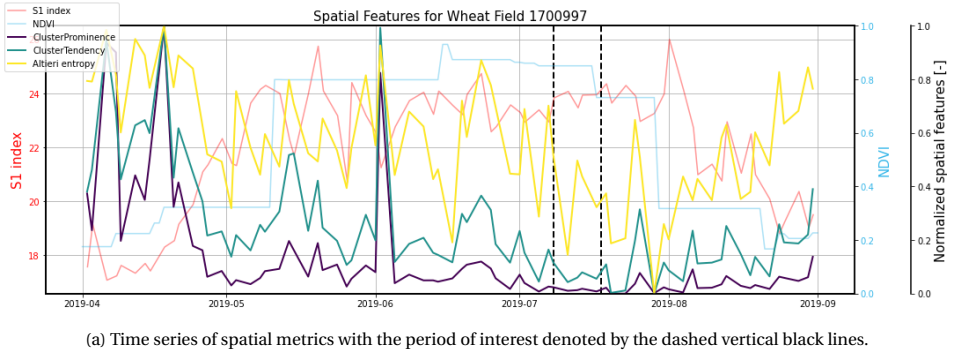

(a) Time series of spatial metrics with the period of interest denoted by the dashed vertical black lines.

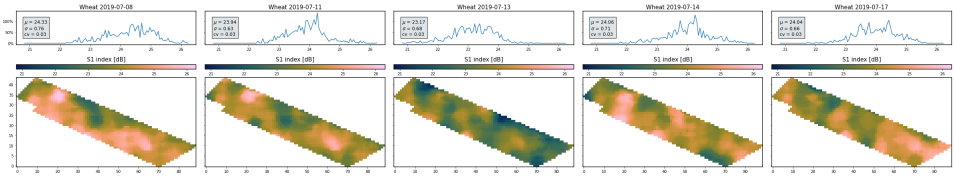

(b) S1 index rasters during period of interest.

Figure F.9: Period of dissimilar spatial metric values of wheat in (a) time, and (b) space.

F.4. Metric computation time

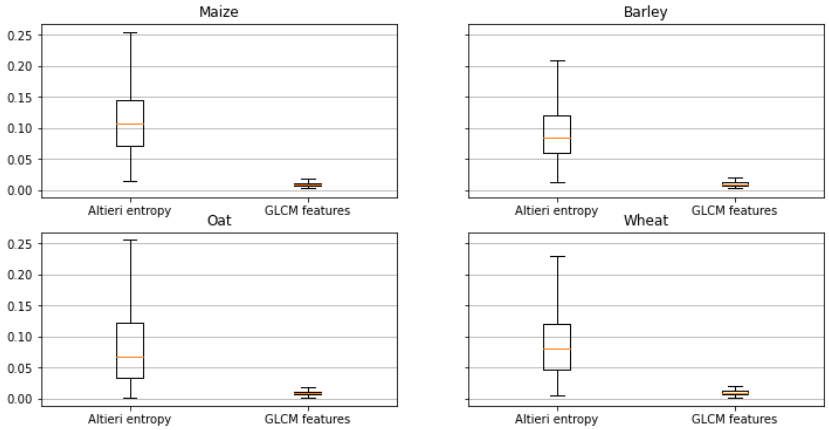

Figure F.10: Computation time of each crop type for the different features, where computation of the cluster tendency and cluster prominence both described by the *GLCM features*.

G

Defining Thresholds

G.1. Threshold selection

As described in Section 3.3.3, the thresholds were defined by sorting the rasters in a descending order, and test them by eye to see if they met the requirements. These requirements were:

1. the raster contains at least two recognisable clusters of at least 10 pixels
2. at least one raster is large, i.e. covers an area with a minimum of 20 pixels
3. at least one raster has an edge with high contrast, i.e. more than 1 dB difference

An example of a raster of which the metric was selected as threshold is shown in Figure G.1.

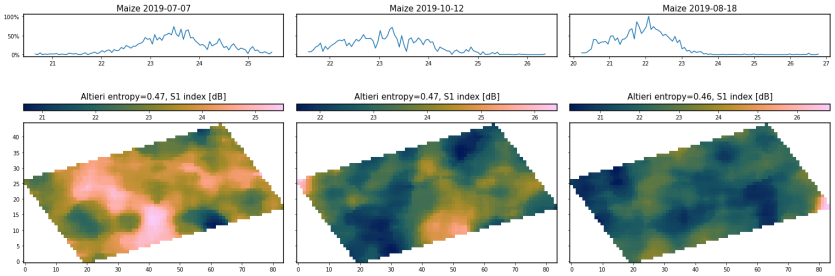

Figure G.1: S1 index raster of selected maize field in descending order of Altieri entropy.

The first two rasters have clearly recognisable clusters, but it is more difficult to distinguish the clusters with lower values in the third raster. Therefore, to avoid a bias towards clusters with values higher than the mean, the rasters were also plotted with diverging colour maps as shown in Figure G.2.

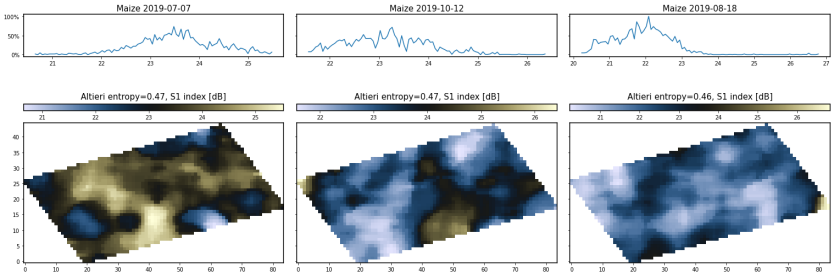

Figure G.2: S1 index raster of selected maize field in descending order of Altieri entropy with diverging colour map.

Even though the dark clusters are better recognisable, it can be seen that the third raster still does not meet all requirements due to its low contrast (requirement 3). Therefore, the threshold was set at 0.46 in this example, and converted to the absolute value for the threshold computation.

G.2. Variability of selected thresholds

However, because the average values are at different orders of magnitude, the standard deviations of these values cannot be compared. Therefore, the coefficient of variation (CV) is used to compute the variability of the threshold values for each crop and metric. The results can be seen in Figure G.3.

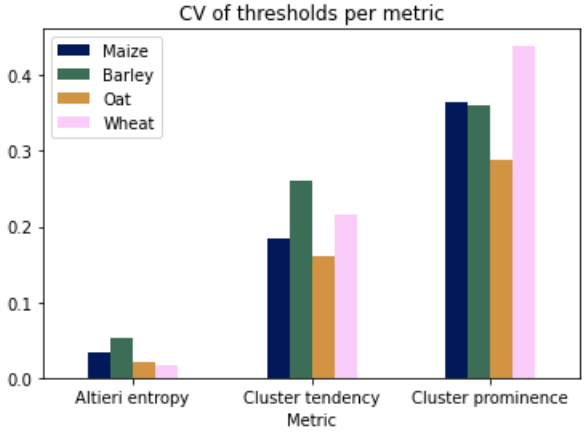

Figure G.3: Coefficient of Variation (CV) per metric and crop type.

Clearly, the variability of the Altieri entropy is the lowest ($CV_{mean} = 0.03$), followed by the cluster tendency ($CV_{mean} = 0.21$) and lastly the cluster prominence ($CV_{mean} = 0.36$). Moreover, the variability between the different crops is also the lowest for the Altieri entropy ($CV = 0.03$), then for the cluster tendency ($CV = 0.24$) and finally for the cluster prominence ($CV = 0.30$). This variability between crops is understandable since a larger uncertainty for each crop type will generally result in a larger variability between the crop types. This result implies that the rasters obtained using the Altieri entropy as a filter are more likely to possess the desired characteristics. However, this does not necessarily result in the exclusion of the other two metrics. Depending on the user's needs, one could make a trade-off between accuracy and precision by setting the value higher or lower.

H

Temporal Consistency Per Crop Type

To compare both the metrics as well as the crop types at field level, the time series of the autocorrelation with the metrics is presented in the following sections. First, a more extensive analysis of the maize field is performed as an example on how to interpret the results. Afterwards, the time series of barley, oat, and wheat are presented.

H.1. Maize

Altieri entropy

The temporal consistency at field level of the autocorrelation with the Altieri entropy is presented and discussed in Section 3.4.1.

Cluster tendency

The cluster tendency in Figure H.1 shows a similar temporal profile to the Altieri entropy of high(er) values before July. It also displays the same behaviour as Altieri entropy in the periods of Figure 4.22. However, between August 19 and 24, there is a high autocorrelation and Altieri entropy, but the cluster tendency stays below the threshold.

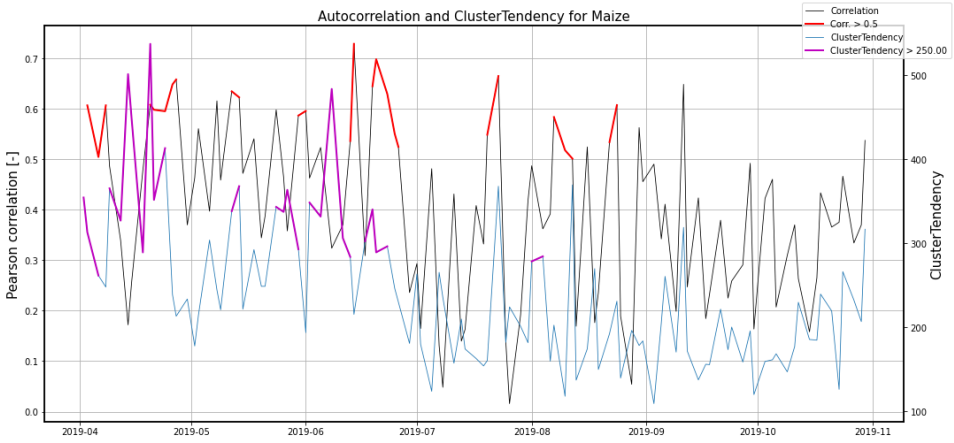

Figure H.1: Time series of autocorrelation and cluster tendency, where periods with two or more subsequent observations are marked for both metrics.

Evaluating the rasters from Figure H.2, it seems logical that the cluster tendency is low: there are few clearly defined clusters, and the area between them is not constant. The Altieri entropy for the second and third raster is 6.93 and 7.05, respectively, above the threshold value. As seen in the respective histograms, the residual entropy largely causes the high value due to the almost homogeneous distribution of backscatter values.

There are two possible causes for the scenario when one metric has values above the threshold, and the other(s) do not. First, the threshold of one metric is selected more strictly than the others. As discussed in Section 4.2.2, the currently deployed method is sensitive to subjectivity, and the sample size was small. This can lead to (too) strict or lenient threshold values so that some rasters will or will not be considered relevant. Secondly, the metrics are different, so they will be sensitive to different spatial features as discussed in Section 4.2.1. In this case, the former seems to be the cause because the selected period has similar cluster tendency values as the whole time series post-June.

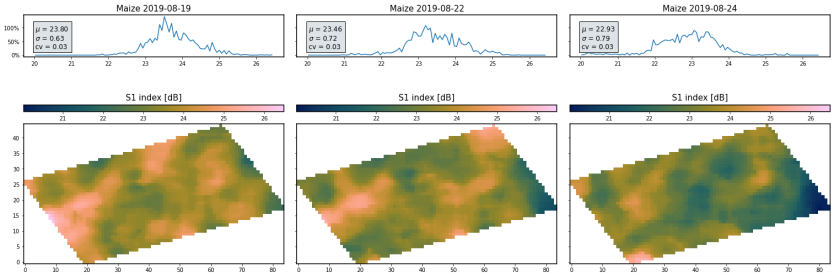

Figure H.2: Spatial S1 index data in a period of high autocorrelation and Altieri entropy, but low cluster tendency.

Cluster prominence

Since the cluster prominence is the amplification of the cluster tendency, periods of values above the threshold are similar, as can be seen in Figure H.3. However, Section 4.2.1 showed that due to this amplification, rasters with prominent clusters correspond to much higher values than 'smoother' rasters. Besides that, the definition of the threshold again plays an important role.

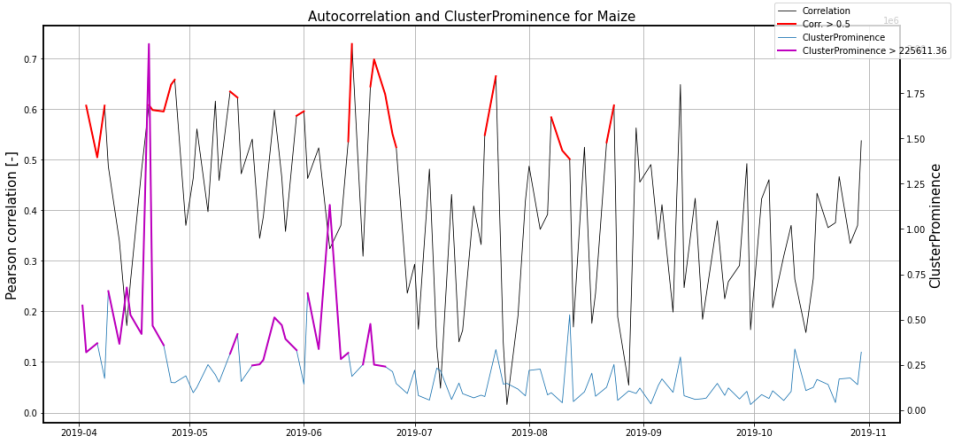

Figure H.3: Time series of autocorrelation and cluster prominence, where periods with two or more subsequent observations are marked for both metrics.

H.2. Barley

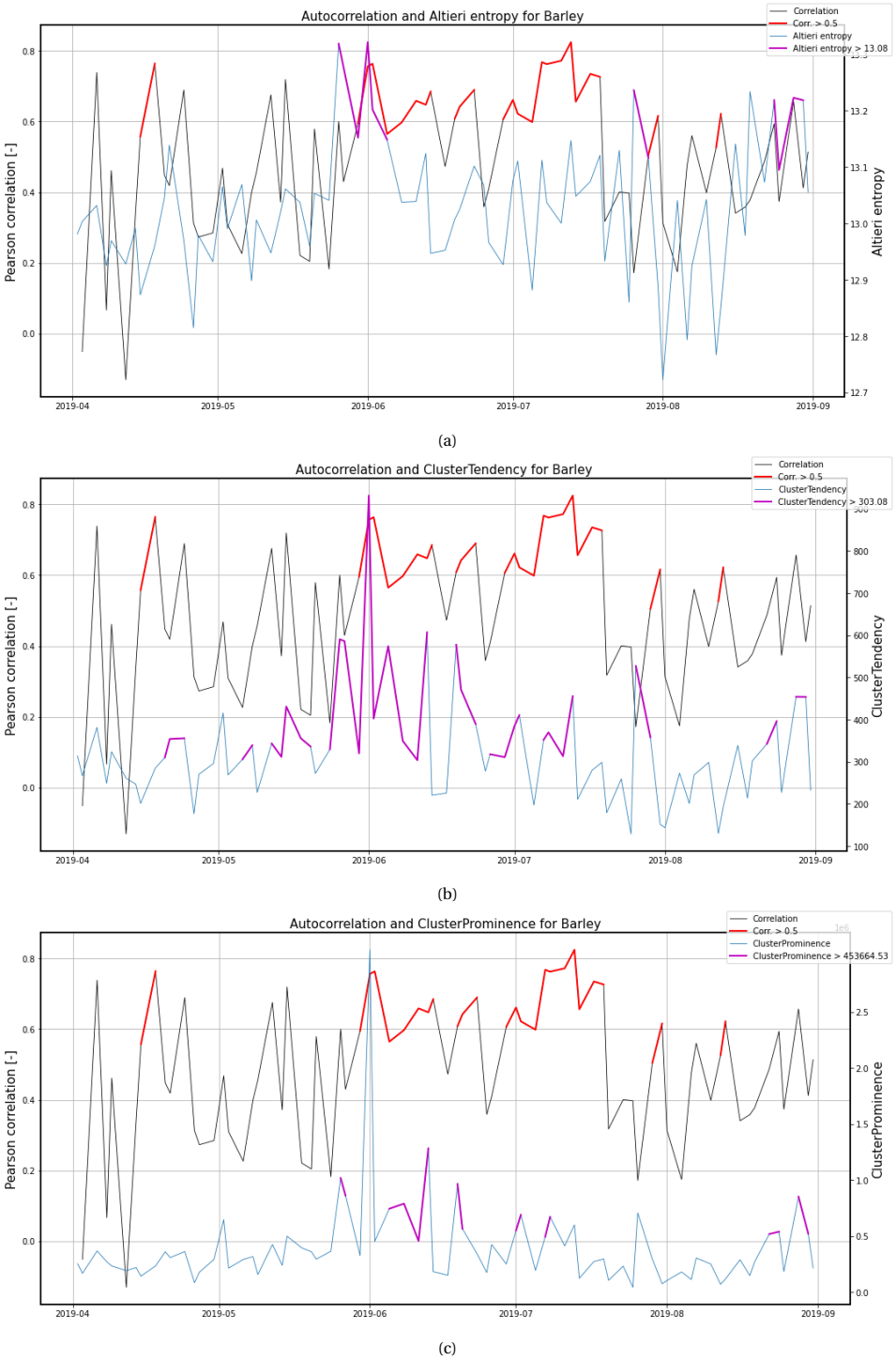

Figure H.4: Barley time series of autocorrelation and (a) Altieri entropy, (b) cluster tendency, and (c) cluster prominence, where periods with two or more subsequent observations are marked for both metrics.

H.3. Oat

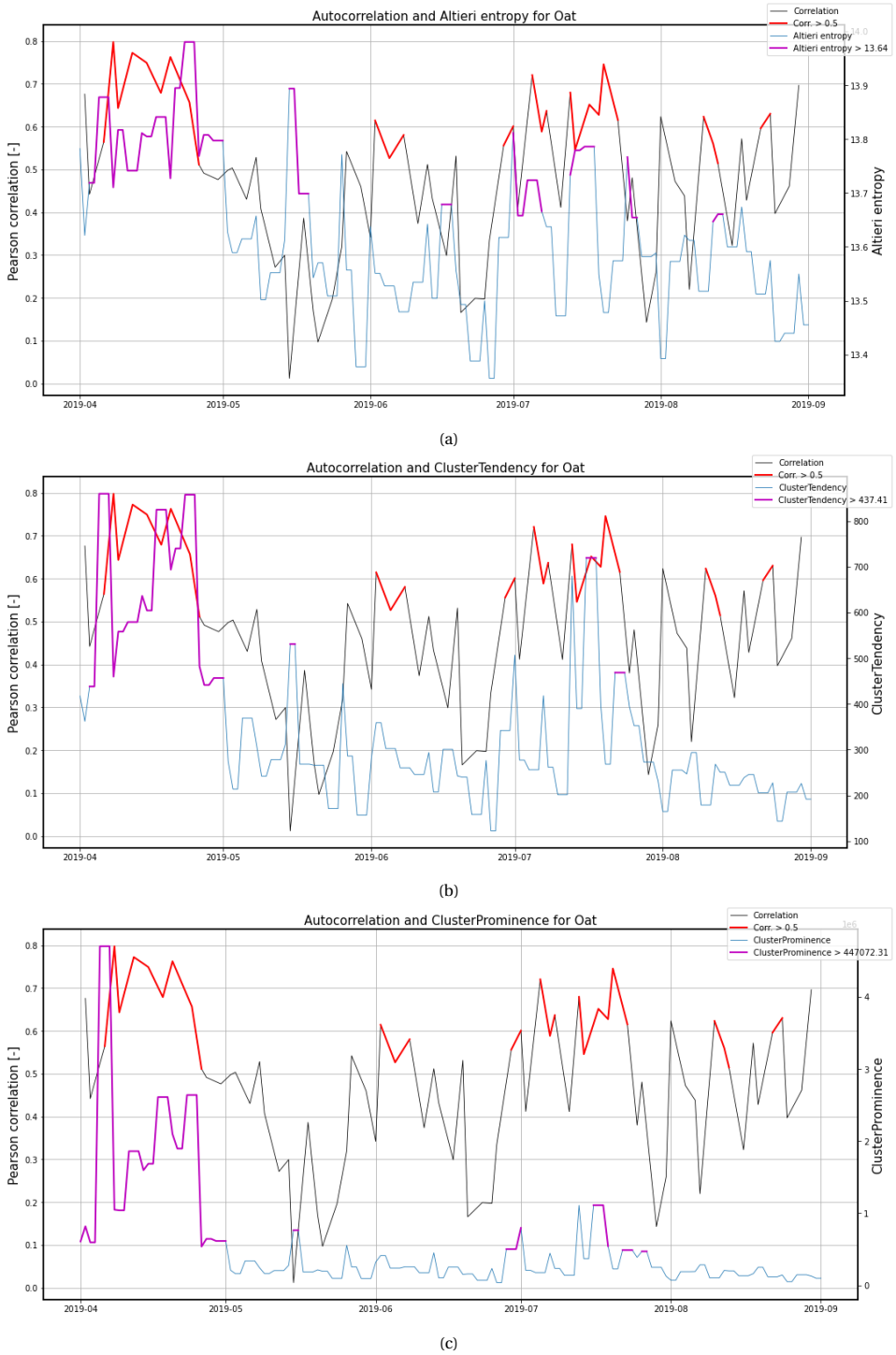

Figure H.5: Oat time series of autocorrelation and (a) Altieri entropy, (b) cluster tendency, and (c) cluster prominence, where periods with two or more subsequent observations are marked for both metrics.

H.4. Wheat

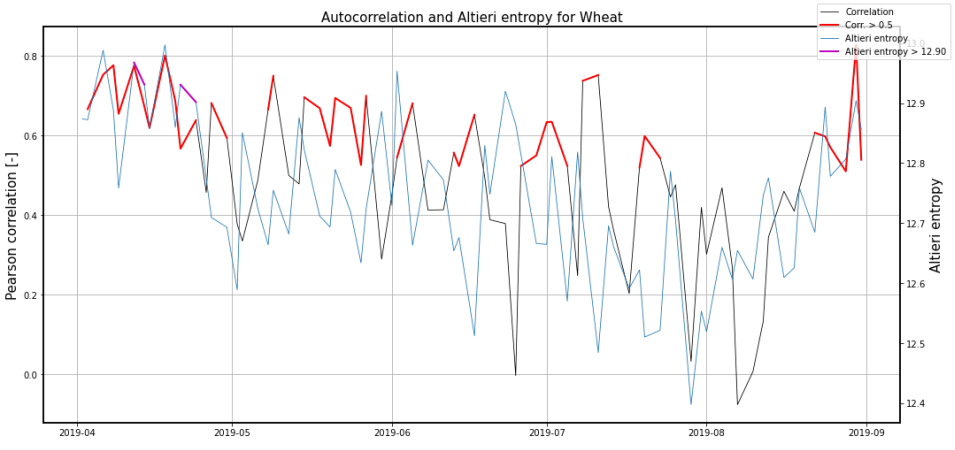

(a)

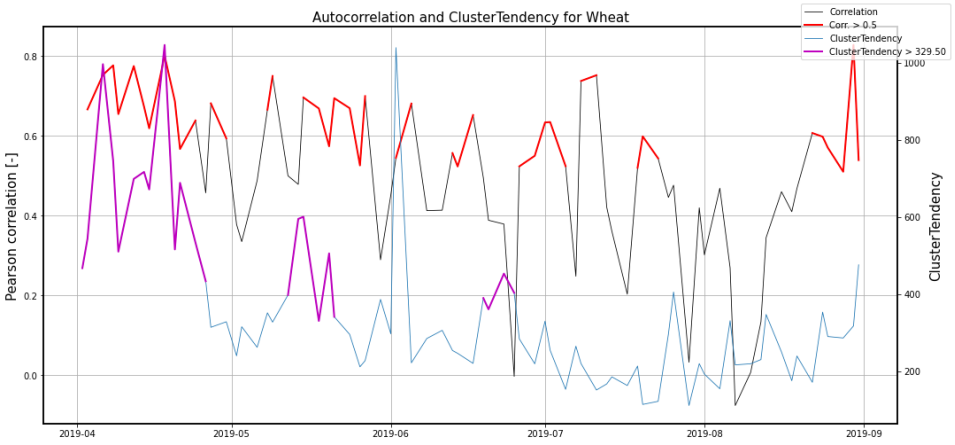

(b)

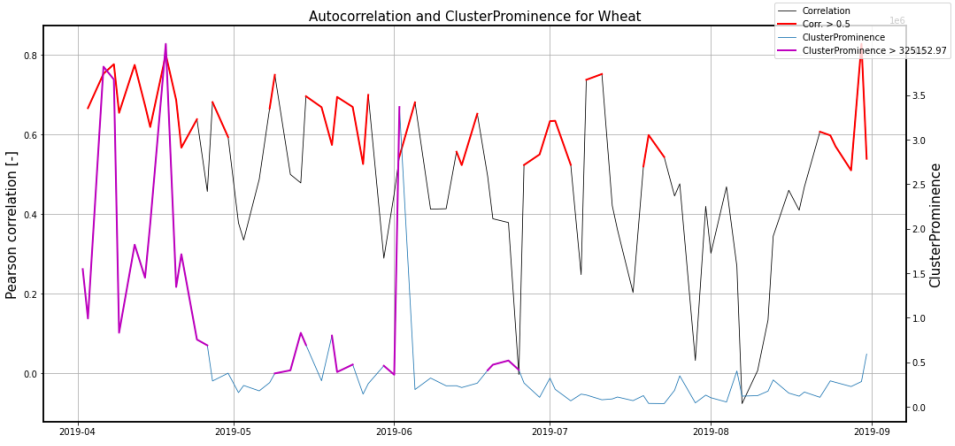

(c)

Figure H.6: Wheat time series of autocorrelation and (a) Altieri entropy, (b) cluster tendency, and (c) cluster prominence, where periods with two or more subsequent observations are marked for both metrics.

Consistency Distribution per Crop

This appendix provides figures to support the analysis of the temporal consistency from Section 4.3.1. First, the histograms only based on autocorrelations are shown in Appendix I.1, followed by the metric comparison of each crop in Appendix I.2.

I.1. Autocorrelation frequency distribution

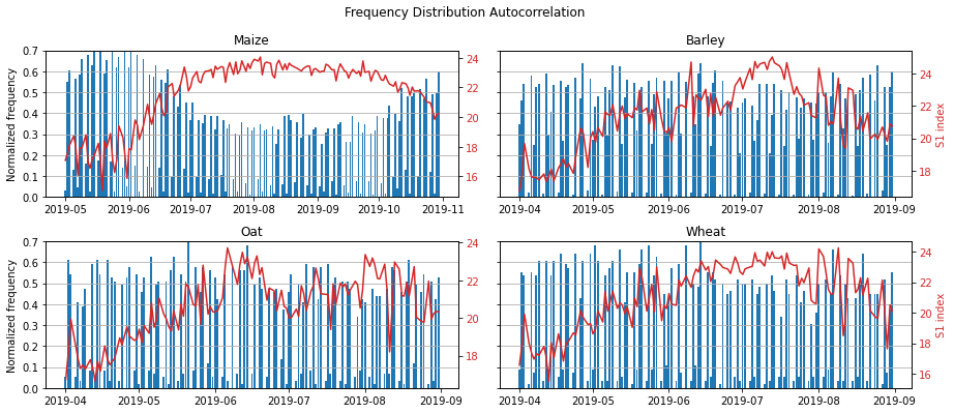

Figure I.1: Histograms of autocorrelation for the four crop types.

I.2. Metric comparison frequency distribution

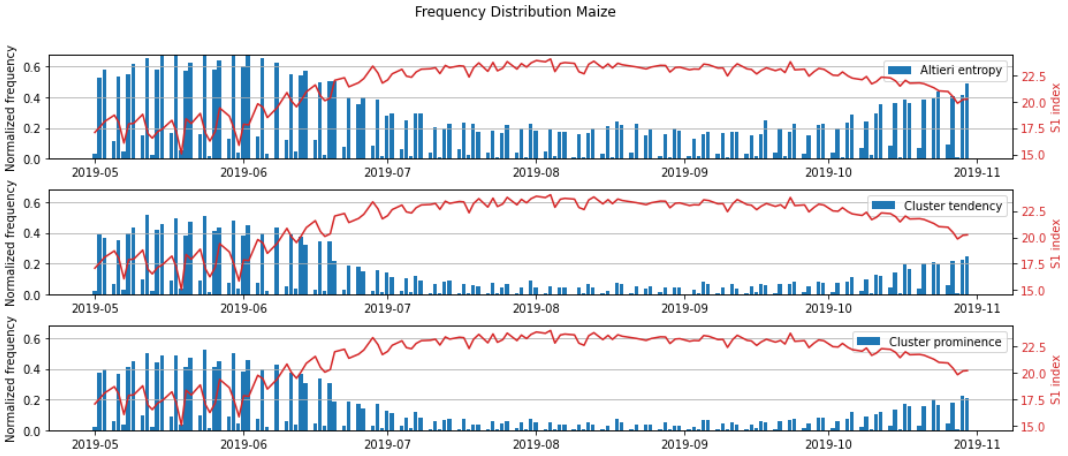

Figure I.2: Histograms of maize where the bars indicate the normalised occurrences of consistency and the red line corresponds to the mean S1 index time series. The subplots correspond to the Altieri entropy, cluster tendency and cluster prominence respectively.

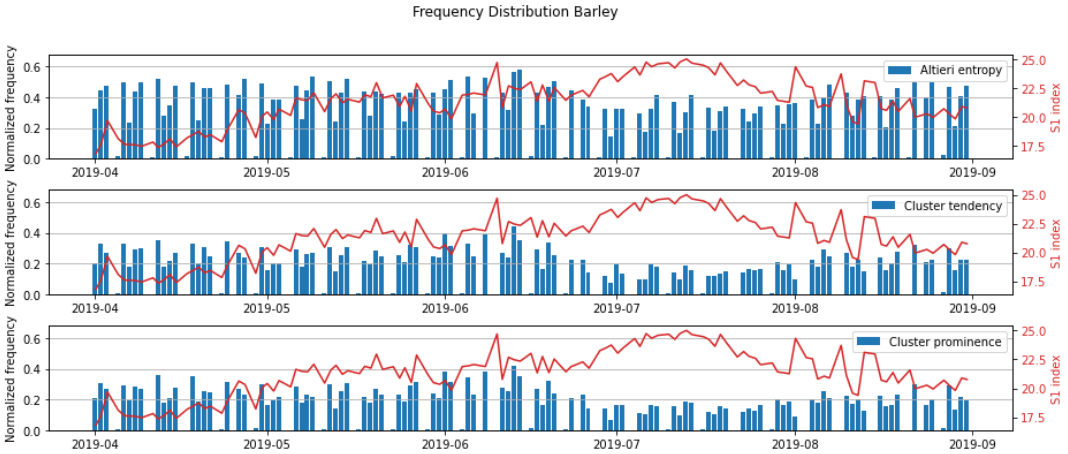

Figure I.3: Histograms of barley where the bars indicate the normalised occurrences of consistency and the red line corresponds to the mean S1 index time series. The subplots correspond to the Altieri entropy, cluster tendency and cluster prominence respectively.

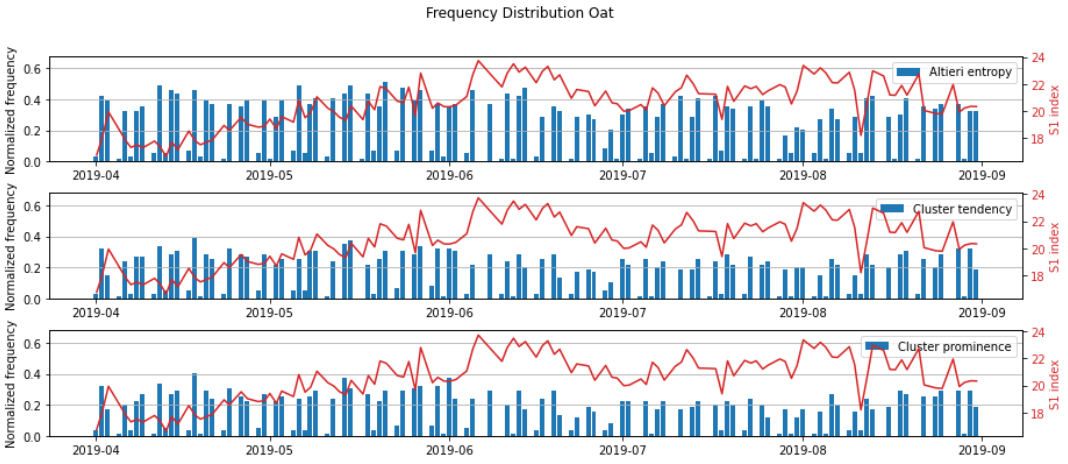

Figure I.4: Histograms of oat where the bars indicate the normalised occurrences of consistency and the red line corresponds to the mean S1 index time series. The subplots correspond to the Altieri entropy, cluster tendency and cluster prominence respectively.

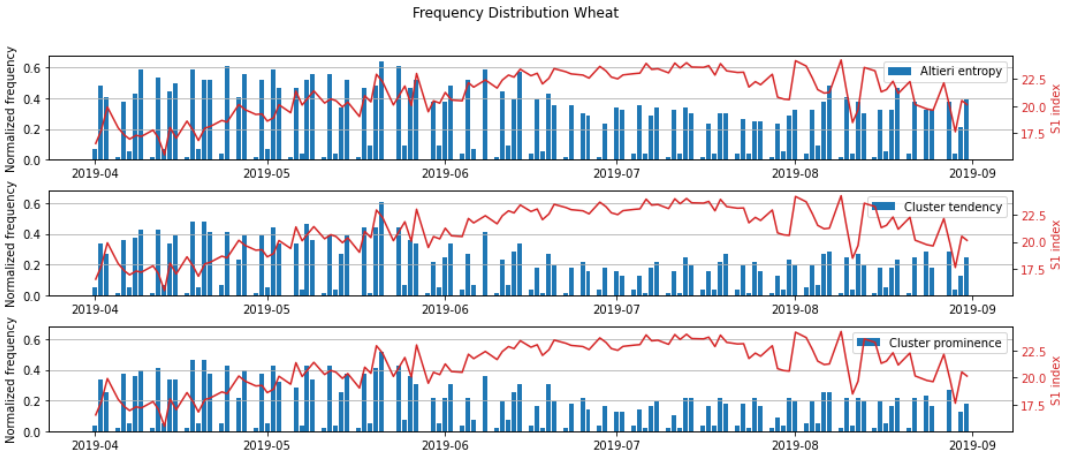

Figure I.5: Histograms of wheat where the bars indicate the normalised occurrences of consistency and the red line corresponds to the mean S1 index time series. The subplots correspond to the Altieri entropy, cluster tendency and cluster prominence respectively.

J

Parameter Sensitivity

To better understand the influence the threshold, the same maize field was plotted for thresholds of 0.01, 0.03 and 0.04, presented in Figure J.1a, Figure J.1b, and Figure J.1c respectively. As expected, differences are clearly visible, and the field is completely considered as consistent for threshold values from 0.065 onwards. As discussed, threshold values could be adjusted to fit the application. For instance, if the user wants to be certain of constant values indicating some change in the field, a low threshold of 0.01 could be used. Another possible use is estimating the reliability of the radar image. If a higher threshold is selected, the missing pixels in the filtered raster indicate large, non-consistent deviations from the mean. If this is a significant percentage of the total number of pixels, it could be regarded as less reliable, assigning it a lower weight in the spatial fusion.
Moreover, larger clusters could indicate large change, but if the intra-cluster variability is high, the change is not the same for the entire cluster. On the other hand, small clusters with little variability are likely to be more precise and could therefore be just as relevant. Depending on the application, the inter-cluster variability could be a measure to select a suitable threshold.

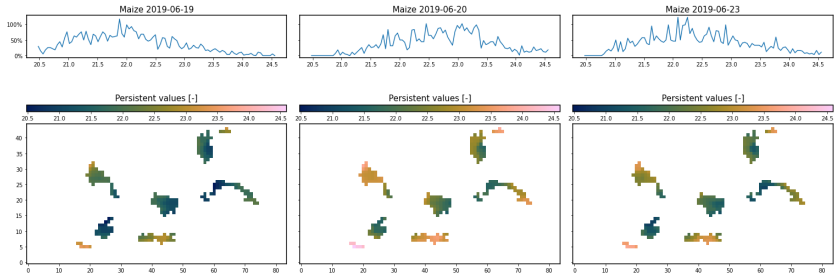

(a) Threshold of 0.01.

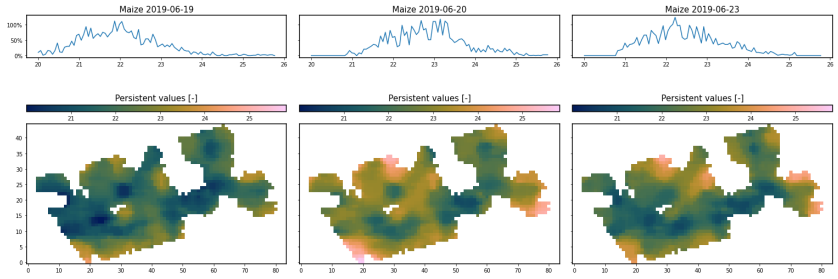

(b) Threshold of 0.03.

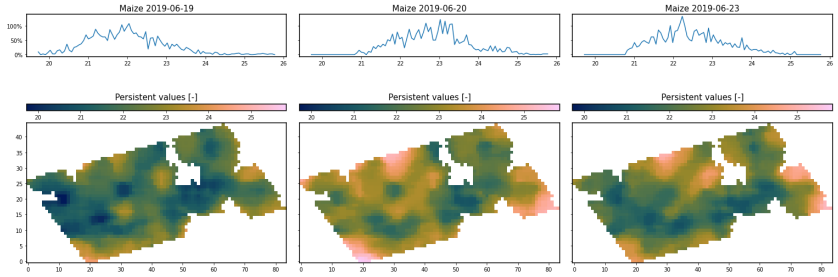

(c) Threshold of 0.04.

Figure J.1: Effect of various threshold values on defining persistent clusters, an example of the selected maize field.

Besides threshold value, the current method is severely affected by the number of observations in the period of interest. With the defined threshold values from Section 4.2.2, periods of interest now seldom contain more than four observations. However, if one would adjust the threshold values and thereby increase the number of observations, the method should be robust enough to handle this. The rasters from Figure 4.24 correspond to a period (from June 19 to 23) where the autocorrelation and the three spatial metrics are above their threshold values. However, the autocorrelation and Altieri entropy continue to have high values until June 26. Applying the same algorithm to this series of S1 rasters (Figure J.2a), the clusters have shrunk, and connecting parts have been filtered (Figure J.2b).

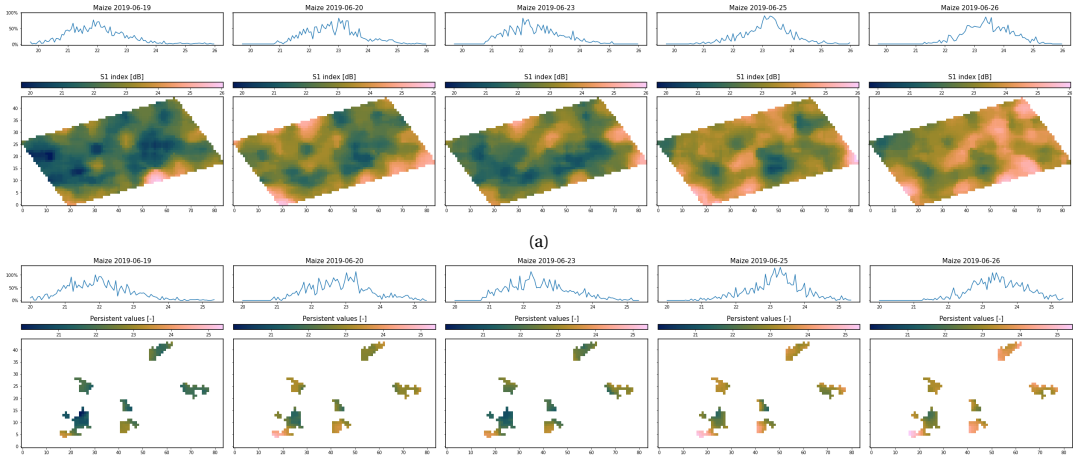

(a)

(b)

Figure J.2: Series of S1 index rasters for period of high autocorrelation and Altieri entropy (a) and filtered rasters based on consistency with threshold 0.02 (b).

This is a limitation of the currently deployed method since by simply comparing Figure 4.25 and Figure J.2b now; it seems that there are more persistent pixels (larger persistent clusters) in the former than in the latter. However, that would neglect that the clusters in Figure J.2b contain two extra observations, thereby increasing the probability of real persistent change. Besides, this method cannot be used in near real-time since it uses an average taken over the selected period.

K

Spatial Consistency Pipeline

To illustrate how the persistent spatial patterns are extracted, this section presents an image corresponding to each step of the spatial processing (steps 2 to 8 in Figure 3.3). After, the effects of the different processing steps are discussed by comparison of the results.

Step 1 of the process is the selection of a suitable period. For this example, a period is selected for which all three spatial metrics were above the threshold values but far enough in the growing season that there is already vegetation. This period is from June 19 to 23. The rasters from this period are shown in Figure K.1.

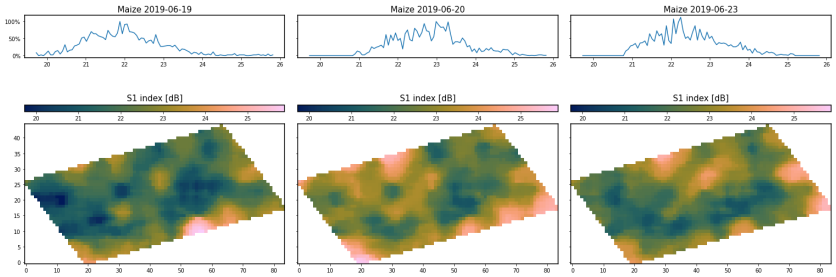

Figure K.1: S1 index rasters of the selected period with high autocorrelation and high spatial metric values.

The following steps (2 to 5) are used to create a mask for each raster, marking the pixels classified as persistent throughout the series. These steps are illustrated in Figure K.2. The input for these steps is the rasters from the selected period (Figure K.1). In step 2 of the process, the internal ratio was taken, i.e. each pixel was expressed in X times the mean of the raster on the respective day (μ_{R_d}). Then the (uniform) average is taken and subtracted from each raster in step 3. This results in the second row of rasters in Figure K.2, where differences are amplified. Note that because the internal ratio was taken from the rasters, the differences are also expressed in this unitless measure. In the fifth step, a boolean mask was created to mark all pixels with a smaller absolute difference than 0.02. For these rasters, this corresponds to 0.45 on average, resulting in an approximate range of 1 dB, which is the radiometric resolution of Sentinel-1.

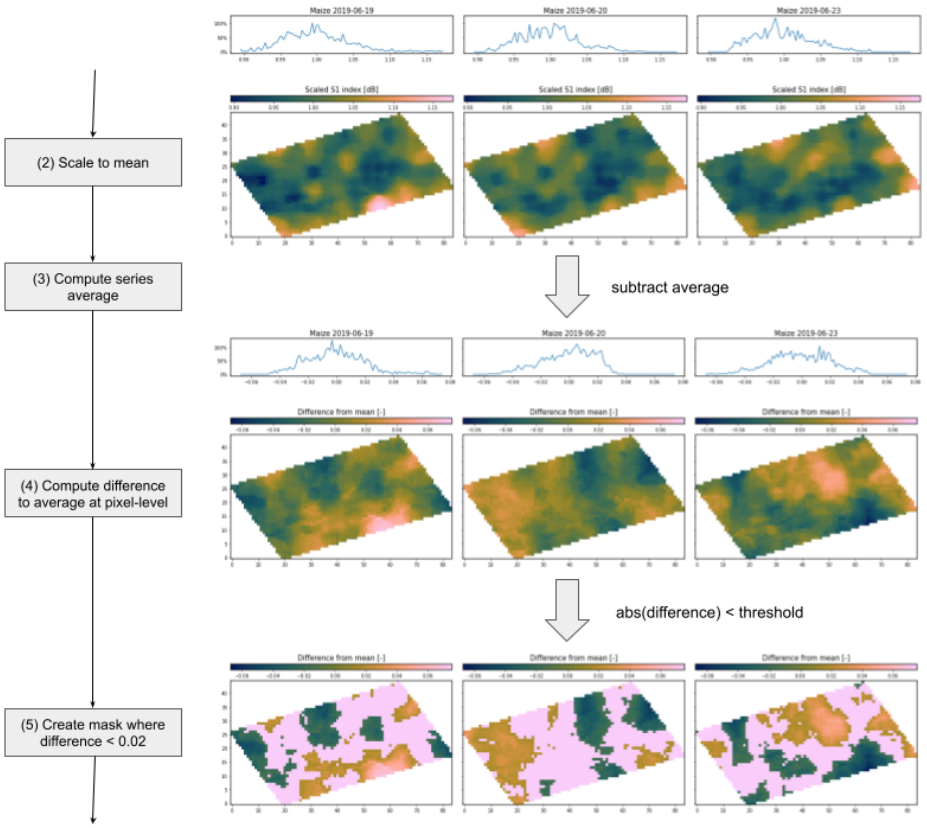

Figure K.2: Processing steps 2 to 5 of the pipeline for spatial consistency.

With the three masks as the output of Figure K.2, a single mask was created to detect which pixels were masked in every raster. This resulted in Figure K.3a. Most single pixels have been filtered out since these are often not constant in time. However, this is not the case for all pixels. It can be seen from the masked rasters that the edges of the single raster masks often cause single pixels or small groups of pixels. Since the assumption was made that only clusters at a larger scale are relevant, the mask was filtered by two morphological filters, of which the result is presented in Figure K.3b. From the before and after, it can be seen that all pixels groups with less than 5 pixels have been removed. Note that also a morphological filter for filling small holes (<5 pixels) was applied, but no small holes were present in the mask of this example. As with the thresholds for the spatial metrics, the threshold for the number of pixels can be adjusted according to the application. This again comes back to the question of false positives and true negatives and should therefore be chosen accordingly.

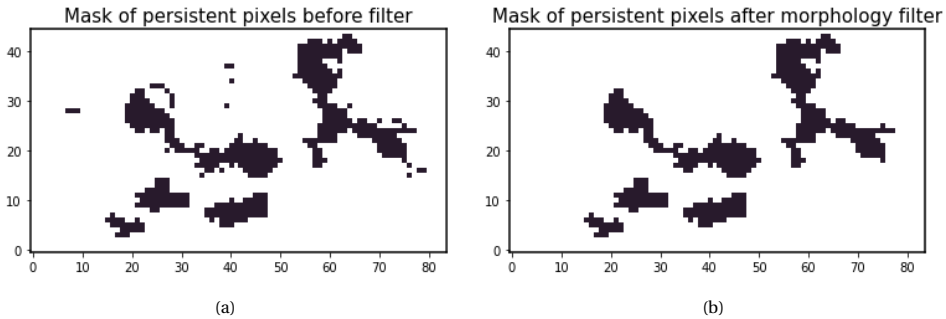

Figure K.3: Consistency mask before (a) and after (b) morphological operations.

The persistent clusters were obtained by applying this final mask to the original rasters from Figure K.1, as shown in Figure K.4.

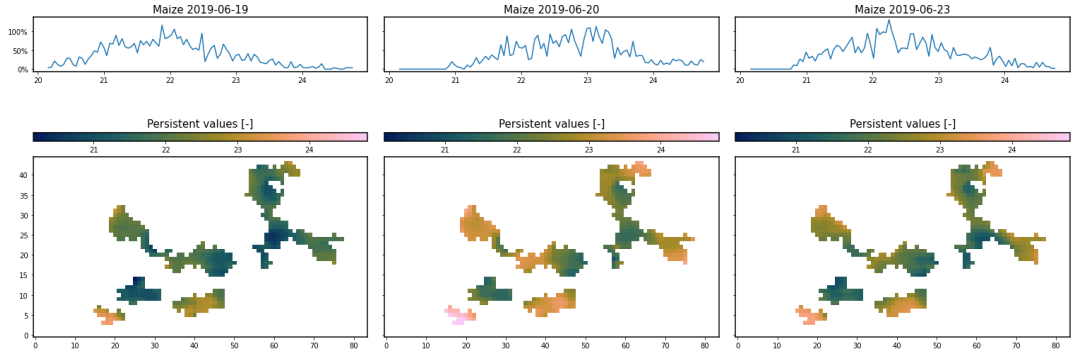

Figure K.4: S1 index rasters filtered by persistent clusters in data.

L

Spatial Data of Weighted Biomass Proxy

This appendix contains the extended analysis from Section 4.4.1. There, day 3 of Figure L.1 was discussed; this appendix will therefore go into days 1, 3, and 4.

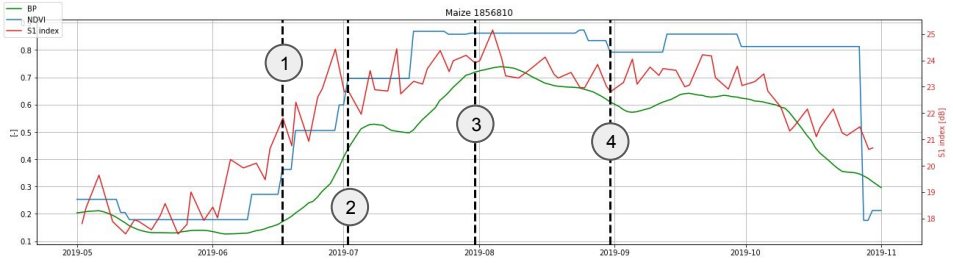

Figure L.1: Time series of the maize field with four days of interest at which the static weight sensitivity analysis was performed.

The results from day 1, corresponding to the leaf development phase, are shown in Figure L.2. It can already be seen from Figure L.1 that the BP value is still low due to the lag of the signal. This is confirmed by Figure L.2, where the average value of the BP fields is 0.17. Because of the low BP time series value, the pattern in the weighted rasters is hardly recognisable. In addition, the S1 index has a relatively large standard deviation (compared to the other S1 index rasters for this field), which contributes to the vague BP signal.

Inspecting the weighted rasters in Figure L.2a, it seems that only rasters of static weights of 0.5 and higher show similar spatial features as those visible in the S1 index raster. However, looking at the clustered rasters in Figure L.2b, the algorithm already recognises an isolated cluster in the middle of the raster in the default static weight of $w_s = 0.075$. This demonstrates the algorithm's ability to fuse the two signals with a strong spatial preference for the NDVI signal but still keep the most prominent spatial features from the S1 index. Interestingly, the last three clustered raster of Figure L.2b show very little change. This could be due to three different causes or a combination of the three.

Firstly, the high variance of the S1 index, combined with the spatial distribution of multiple small clusters, causes the low BP signal to spread out quite evenly over all these small clusters. Secondly, due to the homogeneity of the NDVI raster, NDVI and S1 index clusters are not 'competing' for which pixel belongs to which cluster. Because of the Euclidean distance measure used in the K-means clustering, spherical clusters are preferred by the algorithm. When two signals are fused, one of which has spherical shapes, the clustering will be inclined to that spatial pattern and will not change. Lastly, the S1 index values are scaled to the NDVI scale to fuse the two signals. The scaling is done using an exponential function with a linear tail, causing the high S1 index values to be amplified and the low values to be smoothed. The bend of this linear to exponential scaling is at 23 dB, thus causing most of the S1 index on day 1 to be smoothed.

Furthermore, spatial NDVI features remain visible in the weighted BP rasters as well. This is clear from the (double) edge in the NDVI signal, which is recognisable in the clustered signals until the cluster with $w_s = 0.5$.

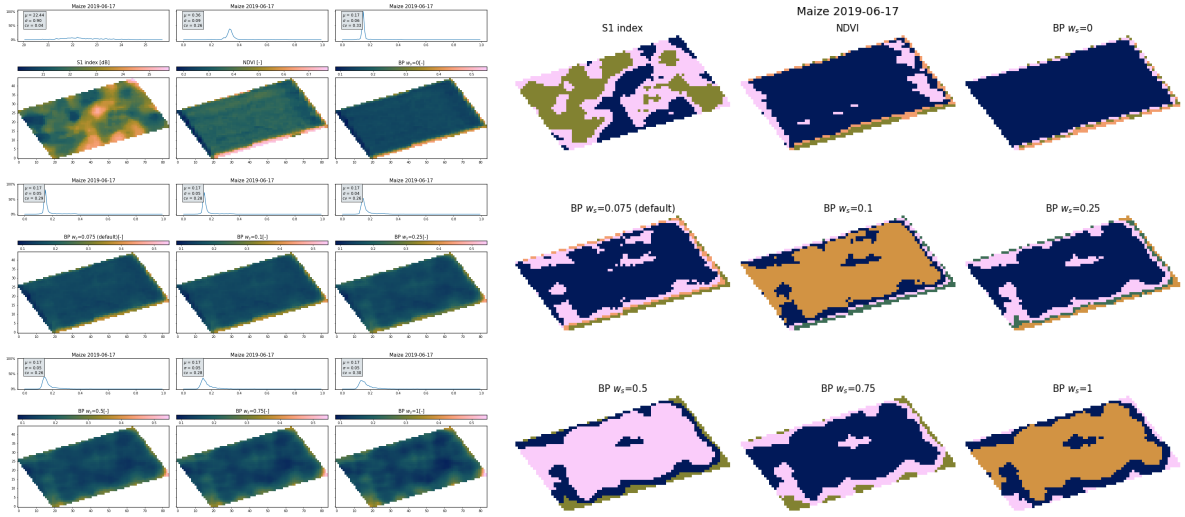

(a) (b)

Figure L.2: BP weighted rasters for varying static weights of day 1, regular (a) and clustered (b).

Figure 4.27 and Figure L.3a show that on day 2, the field means of the S1 index, the NDVI, and the BP have increased. Due to the higher mean value and the stronger contrast between clusters of the S1 index, the spatial radar-like features are better recognisable in the BP rasters than on day 1. Besides that, the NDVI raster is less homogeneous and shows a weaker spot in the field on the right side. Spatial features from the NDVI data, such as the horizontal line near the upper edge, can be seen in the clustered rasters up to and including the BP raster of $w_s = 0.25$.

Comparing the last three clusters of the weighted BP, the clusters appear to become smaller, which is a negative side effect under the assumption that larger clusters are of interest. Interestingly, comparing the BP cluster of $w_s = 1$ to the S1 index raster, the former has much smaller clusters than the latter. This is again caused by a combination of the temporal averaging of the BP and the scaling of the S1 index rasters.

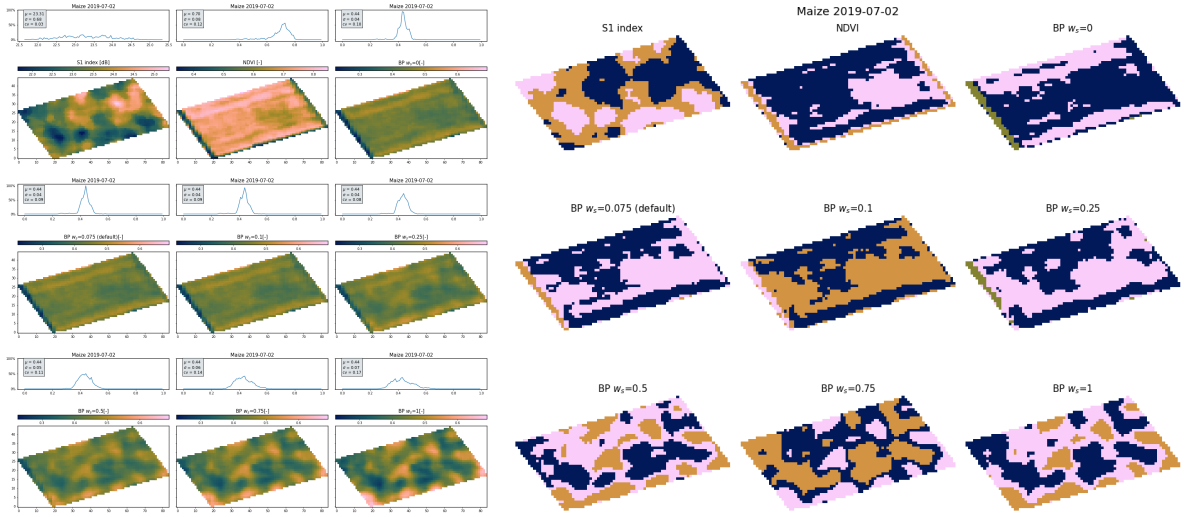

(a) (b)

Figure L.3: BP weighted rasters for varying static weights of day 2, regular (a) and clustered (b).

Figure L.4 shows that on the last day, day 4, a similar result was obtained as on day 3. The mean value of the BP rasters has decreased slightly, which agrees with Figure 4.27. Interesting to see is that for the same static weight, $w_s = 0.25$, clusters are detected in Figure L.4b. For the NDVI-saturated barley field, this value is either the same or 0.5 (Appendix L). For oat and wheat, this always was 0.5. More fields should be checked, however, before any conclusions can be drawn.

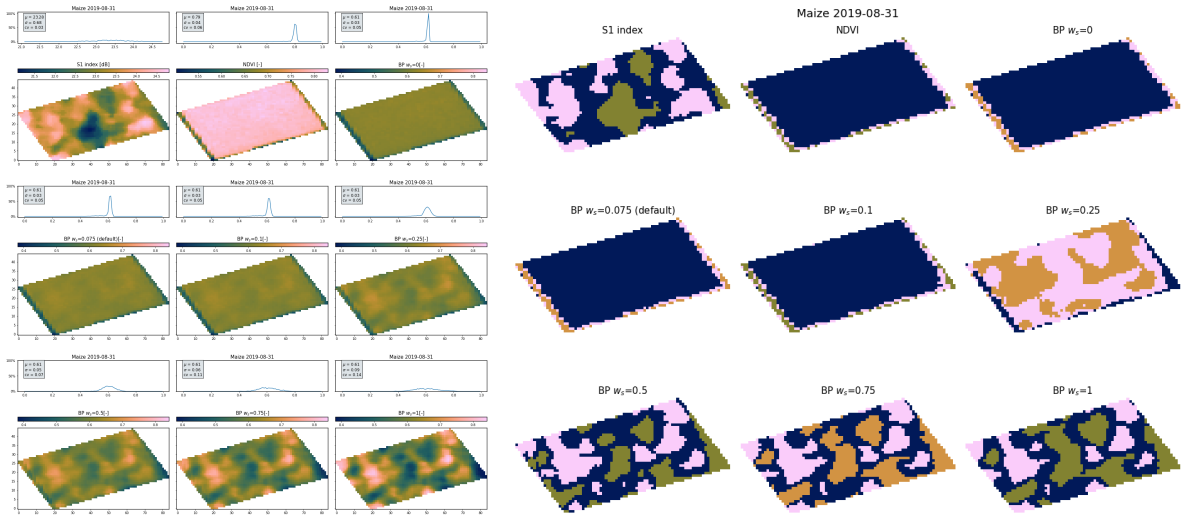

(a) (b)

Figure L.4: BP weighted rasters for varying static weights day 4, regular (a) and clustered (b).

Note that these rasters were all computed on days with full-coverage NDVI observations. Since the final weight is a product of the dynamic and static weights, the S1 index contribution increases over time. Thus spatial features from the radar could become visible in the BP raster at lower weights than might appear from this analysis.